LASER INTERFEROMETER GRAVITATIONAL WAVE OBSERVATORY
- LIGO -
==========
LIGO SCIENTIFIC COLLABORATION

Technical Note	**LIGO-T2200287–v3**	2024/05/01

Report from the LSC Post-O5 Study Group

Post-O5 Study Group

Distribution of this document:
LIGO Scientific Collaboration

Contents

List of Figures

1 Executive summary

This document is the result of a small study group, made up of members of the LIGO Scientific Collaboration (LSC), that has been exploring possible upgrades to the LIGO detectors following the fifth observing run (O5). The intended audience for this report is primarily the LSC, though it is also meant to be shared with funding agencies that support the LSC. The recommendations in the report are meant to guide the LSC research efforts over the next several years, including the post-O5 era which is expected to extend into the 2030s. The report will also form the background for a future proposal from the LIGO Laboratory (and potential international partners) for a detector upgrade that would be implemented after O5. While the future potential of technologies that dovetail with next-generation observatory concepts (e.g., Cosmic Explorer) is highlighted, the scope of this report does not include any assessment of next-generation observatories.

Current planning has O5 running through the end of 2028, so the first post-O5 upgrades should be designed to be available for installation at the start of 2029, with operation continuing through the mid-2030s. Factoring in time estimates for funding and upgrade fabrication, an upgrade proposal submission to the NSF by early 2025 is an appropriate target.

To assess the technical readiness of the technologies discussed in this report, we have tried to apply the Technology Readiness Level (TRL) method used by NASA, DoD, and industry, which rates technical maturity on a scale of 1 to 9 (9 being the most mature). A common practice is to require all enabling technologies to be at a TRL of 6 or higher before a concept can enter the project phase. We recommend that we begin to use this criterion for LIGO technologies, although it may take some trial-and-error to apply and adapt the standard TRL designations.

The report lays out a collection of upgrades to the A+ interferometers that we believe can potentially achieve the required technical readiness on the post-O5 timeline, and would offer roughly a factor of two improved strain sensitivity at low frequencies (below 50 Hz) and high frequencies (above 300 Hz). The former involves improved seismic isolation, larger test masses, and improved test mass suspensions. The latter involves higher laser power (and accompanying improvements in thermal compensation and parametric instability suppression), and increased squeezing. The paths to these technical advances appear to be achievable, though certainly challenging in some areas. Furthermore, the Cosmic Explorer detector design is based on the use of these technical advances, so implementing them in LIGO paves the way for these third generation instruments.

Reducing detector noise at mid-frequencies (50–300 Hz) requires lower thermal noise coatings for the test masses. Without such a reduction, the improvement in quantum noise would provide little benefit at mid-frequencies. Therefore we are including a reduction in coating thermal noise in the baseline post-O5 upgrade, with a factor of $\sim$2 reduction beyond A+ as the target. This goal is technically less certain than the other upgrades just mentioned. Crystalline coatings using AlGaAs/GaAs layers represent the best option for significantly reduced Brownian thermal noise (though other noise mechanisms need investigation, see Section 5.2.2); it is the only coating type that has demonstrated thermal noise substantially below the A+ design goal in a direct noise measurement. While scaling up the AlGaAs technology to test mass size is a matter of engineering, the production tooling and manu-

facturing costs for crystalline coatings are significantly higher than for amorphous coatings. There are also some open technical questions stemming from the material's birefringence. The new, heavier test masses will have to be coated with the best coating available, therefore continued R&D on both amorphous and crystalline coatings is essential as any reduction in thermal noise (and in absorption) would be beneficial.

At very low frequencies, below about 30 Hz, any proposed sensitivity improvement must confront the large discrepancy between current interferometer performance and the design strain noise spectrum.[1] Improvements to the low frequency noise will surely be made by O5. But noise reductions in the control band (below 10 Hz), resulting from the seismic isolation and suspension improvements and the heavier test masses called for in this report will be critical to achieving the design spectrum below 30 Hz, and therefore critical to reaching the science targets that come from low frequencies.

At high frequencies, above a kHz, a straightforward option is to widen the bandwidth of the differential signal by increasing the reflectivity of the signal recycling mirror.[2] This comes at the expense of reduced sensitivity below a kHz, although if the mid-frequencies are limited anyway by coating thermal noise, the loss is not very substantial. Of course there is a continuum of bandwidth options between the specific A$^\sharp$ and A$^\sharp$-wideband cases in this report – this can be optimized when more is known about the detectors and the target GW sources. Variable transmission mirrors (signal recycling and filter cavity input), if they can be made low-loss and low-noise, could provide useful in situ bandwidth control, and are a technology that should be pursued.

The Voyager concept – 200 kg crystalline silicon test masses at 123 K, 2 µm laser wavelength, 4 MW arm power – holds promise for its inherent power handling capability and low thermal noise, but its underlying technologies are less mature than A$^\sharp$. In the event that the room-temperature, fused silica, 1 µm configuration simply cannot achieve good high power operation (due to thermal distortions), or that lower noise coatings cannot be developed, Voyager may prove to be the best way forward towards better sensitivity and new discoveries with the LIGO observatories.[3]

Given the current maturity of several Voyager technologies, it is not likely that Voyager could be implemented on the immediate post-O5 timescale; however, we recommend that the LSC pursue the research and development of Voyager technologies so that it could become a viable upgrade option. The confluence of technologies between Voyager and the Einstein Telescope (as well as a possible Cosmic Explorer upgrade) make this a promising direction. We further recommend that a more in-depth review of Voyager technology readiness be carried out in the near term (within the next six months), and that it involve both LSC and non-LSC experts in the full range of technologies required for Voyager.

[1] 'Design spectrum' refers to the sum of fundamental noises as calculated by GWINC. Currently, the best performance at 20 Hz is about a factor of four above the A+ design spectrum, and about one and a half orders of magnitude above at 10 Hz.

[2] When employing frequency dependent squeezing, the reflectivity of the filter cavity input mirror would also need to be changed.

[3] If, on the other hand, upgrades to fused silica 1 µm technology are successful, improvements beyond A$^\sharp$ could allow for sensitivity comparable to the Voyager design; such a design is included in Appendix A and Appendix C under the name Spacetime Observer, or STO.

We adopt a range of familiar metrics to evaluate the relative scientific outcomes possible with the configurations being considered. We focus on compact binary science targets, since our current knowledge of the astrophysics allows us to make predictions robust enough to anticipate trade-offs between the design decisions explored in this report.

The baseline A$\sharp$ design will boost detection rates over the A+ design by a factor of $\sim$5 and $\sim$2.9 for binary neutron star (BNS) and binary black hole (BBH) mergers, respectively. All variants of the A$\sharp$ design will more than double the lead time of early-warning BNS alerts, enabling detection of signals six minutes or more before merger. A$\sharp$ could improve the precision of tidal deformability measurements by almost a factor of $\sim$2 over the A+ design. Wideband configurations would provide the best chance detecting post-merger signals from BNS mergers, though signal-to-noise ratios (SNRs) will remain $\lesssim 5$ for most signals, and the corresponding reduction in sensitivity at low frequency will reduce overall detection rates, e.g., by $\sim$45% for BNS mergers and $\sim$30% for BBH mergers for A$\sharp$-wideband relative to A$\sharp$.

Finally, if the gravitational wave background from binary mergers has continued to elude detection by the end of O5, *any* of the improvements considered here would guarantee detection in subsequent observing runs.

2 Introduction

Since 2015, LIGO and Virgo established the field of gravitational-wave astronomy, with the detection of nearly 100 gravitational wave signals over the first three observing runs. The LIGO Scientific Collaboration has well-defined plans for improving and operating the LIGO interferometers for the fourth and fifth observing runs over the coming half-dozen years. For the fifth run (O5), the interferometers will be operating in the full Advanced LIGO configuration, plus the addition of the A+ upgrades. The target design sensitivity for O5/A+ is given in LIGO-T1800042.

This report looks beyond the O5 time frame, at options for continued interferometer upgrades in the LIGO facilities. The process started in March of 2021, when the LSC Directorate developed a charge for a LIGO 'Post-O5 Study Group' to explore and evaluate potential upgrades (see LIGO-M2100044). Over the ensuing couple of months the study group was formed with the following membership:

Peter Fritschel, LIGO Lab, MIT, Chair	Jenne Driggers, LIGO Lab, LHO
Brian Lantz, Stanford	Anamaria Effler, LIGO Lab, LLO
Dave Ottaway, OzGrav, Adelaide	Kate Dooley, GEO, Cardiff
Stefan Ballmer, Syracuse	Gabriela Gonzalez, LSU
Rana Adhikari, LIGO Lab, Caltech	Sendhil Raja, LIGO India, RRCAT
Matthew Evans, LIGO Lab, MIT	Ben Farr, Oregon
Patricia Schmidt, Birmingham	Kevin Kuns, LIGO Lab, MIT

In addition, the LSC Directorate (D Reitze, A Lazzarini, P Brady) are ex officio members.

To organize the effort, the following subgroups were formed:

- **O5 Planning: Instrument** and **O5 Planning: Science**. These two subgroups were formed to answer the question: when does the post-O5 period begin? On the instrument side, this meant evaluating when the detectors might reach the target O5 sensitivity. On the science side, this meant evaluating how long LIGO should observe once at that sensitivity.

- **Room temperature, 1 µm upgrades.** This subgroup looked at upgrades within the context of room temperature fused silica test masses and 1 µm laser light.

- **Voyager.** This subgroup evaluated the technical readiness of the Voyager detector concept, which uses silicon test masses at 123 K and 2 µm laser light.

- **Other instruments.** This subgroup keeps track of the plans of other astronomical instruments – both other gravitational wave detectors and electro-magnetic telescopes – that should be taken into account in our post-O5 plans.

- **Post O5 Science.** This subgroup evaluated the science of and sets science targets for the candidate post-O5 upgrades.

This report attempts to cover options for detector operation in the LIGO facilities in the decade after O5, with necessarily more uncertainty in the latter part of the period. We make several recommendations that would eventually form the basis for a proposal(s) for post-O5 upgrade projects.

Fig. 1 shows the strain noise performance for various designs considered in this report. The interferometer design parameters for these cases are given in Appendix A. In brief, they are:

- **A+ design.** This is the A+ design, which starts from the Advanced LIGO design (40 kg test masses, 750 kW arm power), reduces the coating thermal noise by a factor of 2, and adds 6 dB of frequency dependent squeezing. See LIGO-T1800042 for the A+ design curve.

- **A♯.** This is the baseline design upgrade proposed in this report for a room temperature, 1 µm upgrade. It consists of the following improvements on A+: 100 kg test masses; higher stress (2×) test mass suspension fibers; arm cavity power increased to 1.5 MW; squeezing efficiency increased to 10 dB at high frequencies. It also includes another factor of ∼2 reduction in coating thermal noise beyond A+; for a concrete example, we use the design based on AlGaAs crystalline coatings described in Section 5.2.2.

- **A♯ with A+ coatings.** The same as A♯, except that the coating thermal noise is maintained at the A+ target level (i.e., no further improvement assumed).

- **A♯ wideband.** The same as A♯, except the signal bandwidth is increased to 3.4 kHz (from 450 Hz) by increasing the reflectivity of the signal recycling mirror; the filter cavity finesse and detuning are also changed appropriately.

- **Voyager Deep** This is the nominal Voyager design as described in Ref. [1] (with some updates), consisting of: 200 kg silicon test masses at 123 K; 2 µm laser light; 4 MW arm cavity power; 10 dB effective, frequency-dependent squeezing. This "Deep" version is

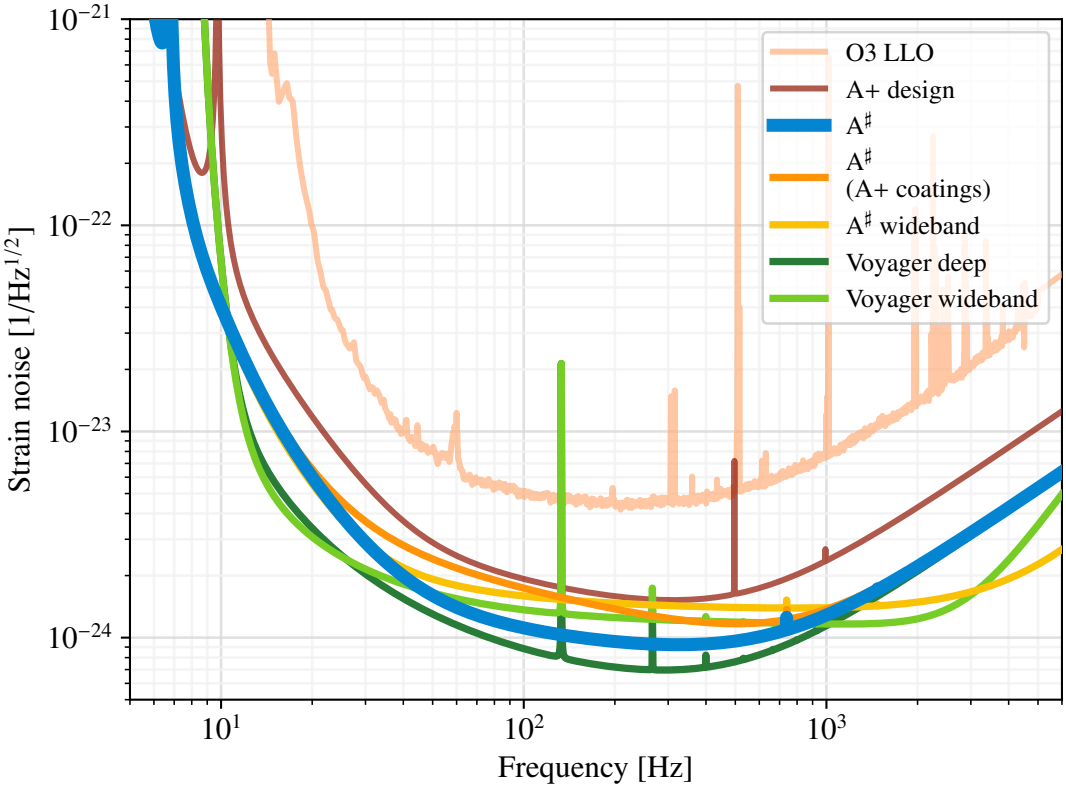

Figure 1: Design strain noise spectra for the post-O5 scenarios summarized in the Introduction. The A♯ wideband scenario updates the A+ wideband tuning proposed in [2] with the improved A♯ quantum noise (Section 5.3.3). The Voyager-Deep and Voyager-Wideband, illustrate the tuning range possible with Voyager with 2 different SRMs (as was envisaged for aLIGO). Whether the noise performance in any real interferometer will approach that of our estimates here, remains uncertain – no interferometer in the past 50 years has reached its fundamental noise limits at the lowest frequencies.

tuned to achieve maximum BNS/BBH range, and puts more emphasis on low optical losses to achieve 10 dB effective squeezing.

- **Voyager Wideband** This is the Voyager Deep design, but with a wider bandwidth to increase the SNR for the BNS mergers by ∼10× over LIGO-O3. For this tuning, the SRM and filter cavity mirrors have to be swapped.

3 O5 timeline

The interval between the end of O4 and start of O5 is currently planned to be around 21 months – 14-15 months of installation followed by 6-7 months of commissioning. This plan, in combination with the expected O4 start of March 2023 and total O4 duration of 13 months (two six month blocks with a one month break), leads to a nominal start date for O5 of the beginning of 2026.

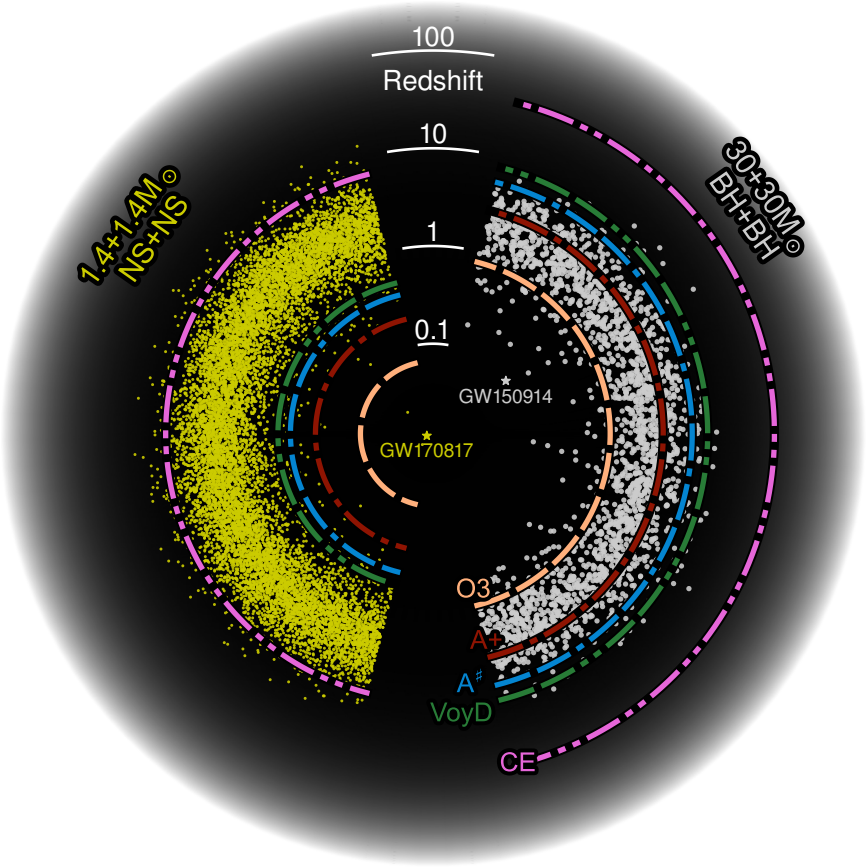

Figure 2: Horizon redshifts for some of the scenarios shown in Fig. 1. The yellow and white dots denote simulated populations of binary neutron star and binary black hole mergers, respectively.

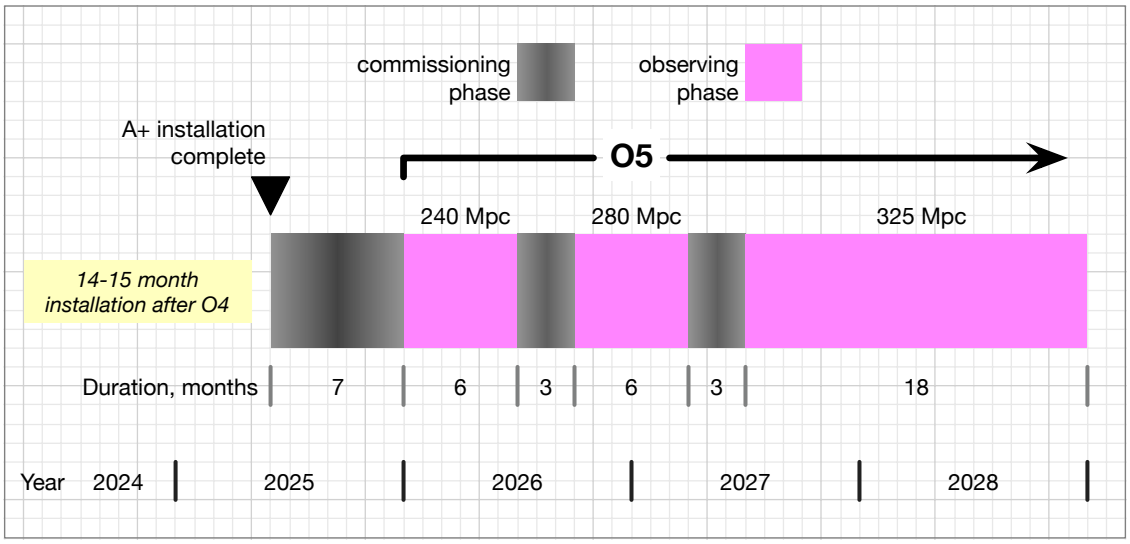

Figure 3: Proposed O5 timeline, with O5 ending at the end of 2028.

We do not expect the interferometers to be at the A+ target design sensitivity at the beginning of O5. That will take more commissioning time and effort. Therefore we have proposed a scenario for O5 that consists first of two observing periods of 6 month duration, each followed by a 3 month commissioning period, before an 18 month observing period at design sensitivity; see Fig. 3. This timeline leads to the following recommendation:

Recommendation: The first post-O5 upgrades should be planned so that they would be available to install starting at the beginning of 2029.

4 Technical Readiness

To assess the technical readiness of the technologies discussed in this report, we have looked into the Technology Readiness Level (TRL) method used by NASA, DoD, and industry. The TRL scale goes from 1 to 9, with 9 being the most mature technology.[4] The practice in NASA and DoD is that all enabling technologies must achieve a TRL of 6 or higher before a project can enter the project phase. For example, the Astro2020 decadal survey[5] states that for "Explorers, SmallSats, and CubeSats, all technologies are required to be at TRL 6 or higher upon selection for implementation". The footnote reference gives TRL 6 as (the full list of TRLs is given in Appendix B):

Definition. System/subsystem model or prototype demonstration in a relevant environment.	**Description.** A representative model or prototype system, which is well beyond that of TRL 5, is tested in a relevant environment. Represents a major step up in a technology's demonstrated readiness.

[4]There are many references on the TRL system on the web; a useful one is https://acqnotes.com/acqnote/tasks/technology-readiness-level

[5]'Pathways to Discovery in Astronomy and Astrophysics for the 2020s', http://nap.edu/26141

For the various upgrades presented in this report, we evaluate the required technologies on the TRL scale, and attempt to establish the criteria for each to achieve a TRL of 6 or higher.

For a stand-alone instrument, such as a new inertial sensor for the Internal Seismic Isolation (ISI), to be at TRL 6 it should be operating and have the target noise performance. The 'relevant environment' would be a vacuum system. The instrument wouldn't need to be LIGO UHV compatible, but must have a reasonable path to achieving that.

5 Room temperature Upgrades to the Existing Interferometers

Here we present (room temperature) upgrades to the existing interferometers, meaning the A+ interferometer configuration, with room temperature test masses and 1.06 µm laser light; fused silica still appears to be the best test mass material. Within this context, the upgrades are to a large extent separable into those that improve the sensitivity at low frequencies (below 50 Hz), mid-frequencies (50–300 Hz), and high frequencies (above 300 Hz). Much of the work described in this section overlaps constructively with the Voyager design concept and some of the R&D supports both approaches.

In brief, the upgrades that improve **low frequency** sensitivity are:

- Larger test masses: increased from 40 kg to 100 kg
- Test mass suspensions: higher stress fibers & other improvements
- Improved seismic isolation for reduced controls noise
- Subtraction of Newtonian noise

Improving the sensitivity significantly at **mid-frequencies** will require lower thermal noise coatings for the test masses. Upgrades that improve **high frequency** sensitivity are:

- Laser power increase to 1.5 MW arm power
- Squeezing increase to 10 dB broadband
- Improved thermal compensation, reduced point absorbers, and parametric instability mitigation for higher power operation
- Wideband signal recycling operation

The design for Cosmic Explorer assumes the use of virtually all of the advances described above, so introducing them into the current facilities will not only improve the astrophysics output in the near future, it will also smooth the path for the adoption of significant technical advances in the next generation facilities.

5.1 Upgrades targeting low frequencies

The main elements comprising the low-frequency upgrades are heavier test masses, improved suspensions for the heavier test masses, and improved performance of the seismic isolation

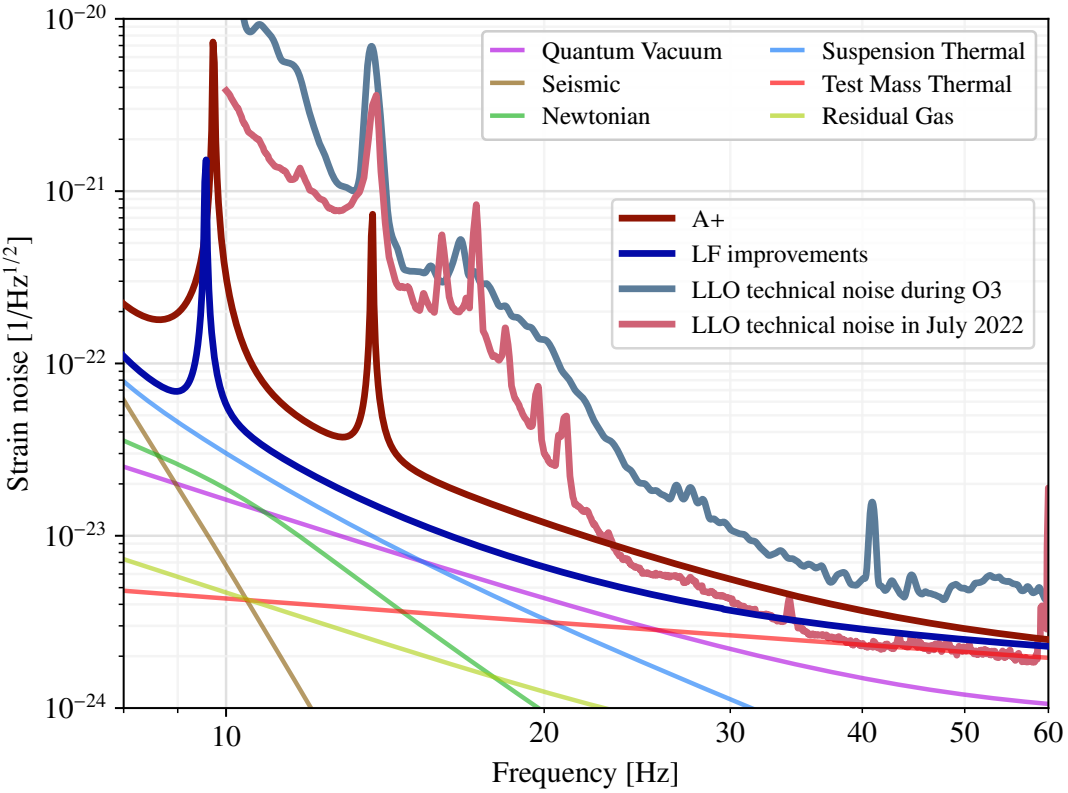

Figure 4: Low frequency improvements from heavier test masses and suspension modifications. The A+ curve is the standard design using 40 kg test masses, 60 cm long fused silica suspension fibers loaded to 770 MPa, 750 kW arm power, and 6 dB frequency dependent squeezing. The dark blue curve improves upon the A+ design by using 100 kg test masses, 60 cm long fused silica suspension fibers loaded to 1.6 GPa, and suppression of Newtonian noise from Rayleigh waves by a factor of two. No further improvements to quantum noise or coating Brownian noise are included; for the full A$^\sharp$ design, the combination of 2× higher arm power and increased squeezing leaves the low-frequency quantum noise essentially the same as shown here, while the test mass thermal noise is reduced by a factor of two around 60 Hz due to the improved coating Brownian noise. The other colored curves show the fundamental noises making up the total low frequency improvements (dark blue curve). The gray curve shows the level of technical noise in the Livingston detector during O3, making it clear that large noise reductions are required before the improvements of the blue curve can be realized. The pink curve is the technical noise during July 2022 and shows that significant progress in achieving this reduction is being made. A noise budget including technical noises during this time is shown in Fig. 18. Many of the proposed low-frequency improvements aim to further address this by reducing noise below 10 Hz (in the control band). The gray and pink curves also show that the 14 Hz roll mode of the test mass suspension shows up significantly in the strain spectrum; for the proposed design (blue curve) the roll mode would occur just below 10 Hz. The roll mode is included in the model curves in an ad hoc fashion – it has the same spectral shape as the bounce/vertical mode, but lower in amplitude by a factor of ten, as observed in the current interferometers.

platforms. Many of the ideas for these improvements were discussed at the Low Frequency Workshop in April 2021, the talks and report (LIGO-L2100055) provide extensive background material for the plans and ideas presented here.

Some of the improvements come from reducing fundamental noises. The increased mass, m, will reduce quantum radiation pressure noise, which scales as $1/m$, and also suspension thermal noise, which scales as $1/\sqrt{m}$ in the LIGO suspensions. By increasing the stress, and possibly the length, of the fused silica fibers that support the test mass, the highest vertical resonant frequency of the suspension will be lowered, effectively reducing seismic and thermal noise in the GW band. The effect of gas damping force noise is also reduced (as $m^{-2/3}$ under certain assumptions). Finally, heavier test masses reduce the impact of radiation pressure noise, so that higher levels of laser power and squeezing can be employed to reduce quantum shot-noise, as discussed in Section 5.3.

The strain noise reduction from these improvements is shown in Fig. 4. There is approximately a factor of 2 reduction in strain noise at frequencies below 30 Hz. The following sections describe the design details behind the 'LF improvements' curve in this plot. The increase in the warning time of a BNS merger is illustrated in Table 1.

Of course these reductions in the fundamental noises will not be fruitful unless the current level of low-frequency technical noise is greatly reduced. This requires reducing controls noise from the auxiliary degrees of freedom of the interferometer – principally alignment controls, but also auxiliary length controls. The strategy is to achieve this by significantly reducing the rms fluctuations in these degrees of freedom by improving the seismic isolation and reducing cross-couplings in the suspensions. In addition, the increased moment of inertia of the heavier test masses will counter radiation pressure torques, also helping to stabilize their alignment.

5.1.1 Larger Test Masses on Upgraded Suspensions

The Advanced LIGO suspensions and optics are often considered to be the crown jewels of the detectors. These systems provide excellent passive isolation and control of thermal noise. Suspension upgrades should retain the design experience of these systems, and improve them using the lessons from operating Advanced LIGO. The most distinct upgrade we're proposing to the quad suspension is increasing the mass of all four stages: the test mass is increased to 100 kg (from 40 kg), and the total mass of the main suspended chain is increased to about 400 kg (from 120 kg). To help accommodate the increased mass, the suspensions would be moved to the center of the ISI.

There are several reasons behind taking 100 kg as the starting point. First, Virgo is already fabricating 100 kg test masses for new ETMs for O5, which should establish a production path for that size in terms of material availability, substrate polishing, and coating at LMA. Second, the total suspension mass should be safely within the maximum payload of the (unmodified) BSC ISI, which is 1000 kg. See more details on this below, but currently it appears that 100 kg test masses would be compatible with this constraint. Finally, currently there is not a clear performance benefit to going larger than 100 kg.

Fused silica material. The ETMs are made of Heraeus Suprasil 312. It is available at the 100–130 kg size we are considering (Virgo has procured 100 kg 312 for their ETMs). The

ITMs are currently made of Heraeus Suprasil 3001, which has lower OH content and thus lower absorption, but its size is limited. Heraeus claims they have a process that could produce 80–90 kg of 3001, though it hasn't been tested. Suprasil 3002 is available in larger sizes (up to hundreds of kg) and has the same low absorption as 3001; however, it is not a '3D material', meaning it is not as optically isotropic as 3001. For use in a single direction, as in an ITM, the homogeneity of 3002 should be adequate, possibly in conjunction with a compensating polish on the back side of the optic. In summary, we don't foresee any issues in obtaining fused silica of 100–130 kg, using Suprasil 312 for the ETMs and 3002 for the ITMs.

TRL 6

Improved Suspensions with increased mass. The new suspensions will be designed to have 100 kg test masses and relatively heavier intermediate masses. In the current design the top two stages of the quad suspension have half the mass of the lower two. There is a benefit to increasing these to have more mass at the top stages; the dynamics are improved because the suspension modes are kept more closely spaced in frequency, improving the isolation and decreasing the required bandwidth of the (noisy) local damping loops; see LIGO-T2100287 and LIGO-G2102249. The latter includes an example of a suspension chain with a test mass of 100 kg and a total main-chain mass of 400 kg. The reaction chain can be much less massive, assume 200 kg at most. That leaves 400 kg for: suspension cage; ETM transmission monitor; other items such as baffles, a beam rotation sensor(s), electric-field meter. Note that the suspension would be centered on the ISI (unlike the current design) so large ballast mass would not be needed for balancing. As discussed below, the new suspensions will include higher stress fibers and modifications to improve the controllability.

Recommendation: A subgroup of the LSC Suspension Working Group (SWG), called the Large Test Mass Suspension Subgroup, was formed in spring 2022. This subgroup should coordinate the design and development of the new test mass suspension, including setting a timeline for development and prototype testing. It seems appropriate to target testing a controls prototype in the LASTI facility at MIT in 3-4 years.

Suspension fiber upgrades. The fused silica fibers that suspend the test mass can be operated at higher stress than they currently are. This would reduce suspension thermal noise and increase vertical isolation, and, by reducing the frequencies of the test mass bounce and roll modes therefore mitigate their encroachment in the GW band; the accompanying increase in violin mode frequencies could also be beneficial. The impact on suspension thermal noise of increasing the stress and length plus changing blade springs is highlighted in Fig. 5 and the summarized in Table 1.

We are targeting a fiber stress of 1.6 GPa, essentially double the stress of the current fibers. At that stress, and keeping the fiber length the same, the roll mode would be just below 10 Hz. The use of higher-stress fibers and larger test masses is considered in some detail in LIGO-G1601071 and in [3]. As the latter notes, a stress level of 1.2 GPa has been used in a couple of test suspensions at Glasgow that hung intact in-air for over 3 years.

Increasing the length of suspension fibers would also decrease thermal noise and bounce/roll mode frequencies, and increase isolation. However, the fiber length cannot be increased significantly without raising the top of the suspension; two options have been proposed to

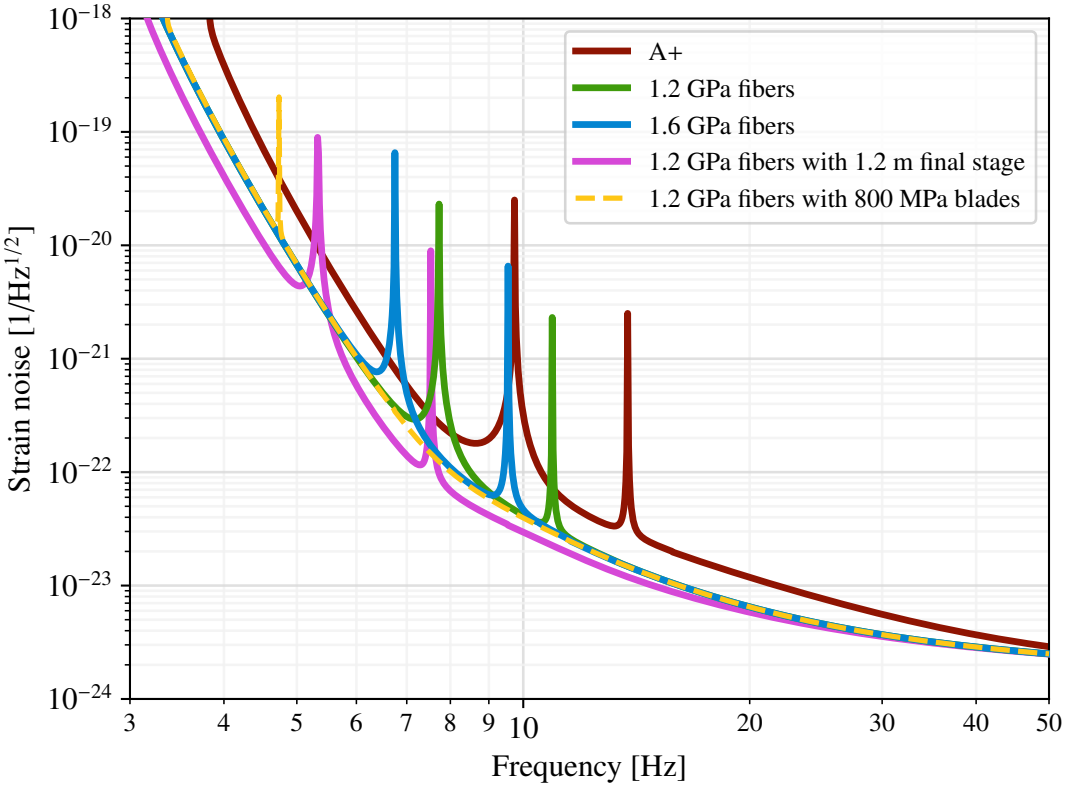

Figure 5: Total detector strain noise for several suspension options. All options have the same 0.6 m long final stage as A+, except for the purple curve which doubles the length to 1.2 m. All options bond the final stage fused silica fibers directly to the penultimate mass, except for the yellow dashed curve which suspends the test mass from fused silica blade springs attached to the penultimate mass. The bounce and roll modes for each option are listed in Table 1. The roll mode is included in the same way described in the caption of Fig. 4. (The bounce mode for the dashed yellow curve, not visible in the plot, is at 3.4 Hz.)

Configuration	Bounce mode [Hz]	Roll mode [Hz]	Violin mode [Hz]	Early warning [min]
A+	9.7	13.8	497	3
1.2 GPa fibers	7.7	10.9	640	6
1.6 GPa fibers	6.8	9.6	738	6
1.2 GPa fibers with 1.2 m final stage	5.3	7.5	311	8
1.2 GPa fibers with 800 MPa blades	3.4	4.7	640	6

Table 1: Suspension resonance frequencies for the detectors shown in Fig. 5 along with the BNS early warning times as described in Section 7 and Table 4.

do this: raise the ISI by adding spacers between stage 0 and the support tubes; mount the top blades of the quad suspension on the upper side of the ISI stage 2 platform, threading the suspension wires through the ISI structure. The second would involve modifications to the ISI that we would prefer to avoid, and the first option carries the risk of compromising the ISI performance. Both involve extra installation work (and thus downtime), which at this time does not appear to be worth the performance advantage.

TRL 5 (6 for stress of 1.2 GPa)

Recommendation: To reach TRL 6, a suspension demonstration at 1.6 GPa should be realized, similar to the test described in [3].

Improved controllability. It should be possible to modify the geometry of the quad suspension to improve its controllability and reduce the cross-coupling of length to angle. It seems that most of the pitch motion of the main optics is caused by the longitudinal motion of the ISI and the longitudinal control signals applied to the suspensions, which cross-couple to produce angular motion. However, as the cross-coupling between length and angle is reduced, the direct coupling from ISI angle to optical angle will be increased (LIGO-G2102370). Studies are underway to optimize the geometry to minimize the total angular drive on the optics. This optimization is an important part of the overall work on reducing the control noise of the interferometers described in Section 5.1.2.

TRL 3. Suspension designs are well understood, but these modifications have not been demonstrated.

5.1.2 Improved Seismic Isolation & Controls noise

The largest contributors to the low-frequency noise excess shown in Figs. 4 and 18 are auxiliary, global controls of the interferometer – primarily alignment controls, but also length controls. These control signals couple into DARM through various mechanisms, not all of which are well understood. We expect that these controls noises will be reduced in the commissioning process for O4 and O5. However, it seems unlikely that the magnitude of reduction needed to reach the target blue curve in Fig. 4 – which is nearly 3 orders of magnitude near 10 Hz – will be achieved solely by improvements to the global control loops. Instead, we think that significant improvements in the performance of the seismic isolation platforms will be needed to reach the low-frequency sensitivity goals. Thus we are proposing significant upgrades to the seismic isolation systems.

The mechanical design of the existing seismic isolation subsystem will remain largely unchanged (if modified at all). Rather, there are upgrades to the sensors that can improve the system performance below 10 Hz. Two useful references for these upgrades are the ISI modeling work presented by Arnaud Pele at the low frequency workshop in 2021 (LIGO-G2100779), and the optical integration talk given by Brian Lantz at the Sept 2020 LVK meeting (LIGO-G2001539).

Capacitive Position Sensors. The modeling work in LIGO-G2100779 shows that the capacitive position sensors (CPS) limit the tilt and translation performance of the HAM-ISI above 1 or 2 Hz. New high voltage readouts for the CPS are now in development by the manufacturer (MicroSens); the new readout should reduce the displacement noise floor of the CPS by a factor of 2−5×, depending on frequency (see LIGO-G2102224). Tests of the

new devices are planned for the HAM8 ISI at LHO. These readouts can be deployed for all the installed sensors, along with upgraded target grounding to reduce sensor glitching, as being implemented in the four new A+ HAM-ISIs. This is a straightforward upgrade.

TRL 7. Units tested at MIT, on order for test in aLIGO

Stage 0 L-4Cs Recent measurements indicate that the performance of the HAM-ISI can be improved between about 3 and 50 Hz by using L-4C sensors (1 Hz geophones from Sercel) on stage 0 of the ISI to feedforward to the optics platform; see LHO aLOG 26221. Although the magnitude of the motion on stage 0 is similar to that seen on the floor by the STS-2 used for sensor correction, the coherence between the floor motion and the stage 0 motion drops to nearly 0 by 2 Hz, whereas the coherence with the stage 0 L-4Cs installed in HAM 4 and HAM 5 show excellent coherence. This is also a straightforward upgrade.

TRL 9. In use on some HAM-ISIs

In-vacuum Rotation sensors. One of the most exciting sensor upgrades we endorse is the addition of compact rotation sensors to the ISIs. These new compact sensors build on the technology used by the large "Beam Rotation Sensor" installed on the floor at LHO and LLO. There are at least two different sensors which are being developed. Michael Ross, at the University of Washington, is developing a "Cylindrical Rotation Sensor" (CRS) with a cylindrical proof mass and interferometric (HoQI) readouts. The "Quartz Rotation Sensor" (QRS) (LIGO-G2000673) is being developed as a commercial instrument at Paroscientific, and is led by Krishna Venkataswara, a graduate from the UWash group. This sensor also utilizes a cylindrical proof mass, but uses a resonant quartz readout.

Alternately, rather than a dedicated single-axis rotation sensor, an inertial sensor small enough to fit on the top of the BSC-ISI or on certain HAM-ISIs with space available (e.g. HAM4) with improved performance in multiple degrees of freedom has the potential of significant performance benefits. Using a single proof mass as a reference for several degrees of freedom is a different design approach than LIGO has used in the past, but such devices are now in development, such as the 'Compact-6D' seismometer being tested at the University of Birmingham.

Rotation sensors are useful because the performance of the ISI at low frequency (the secondary microseism and below) is limited by our ability to measure tilt and to distinguish tilt from translation. Rotation sensors could be placed on the top of stage 2 of BSC-ISIs, and on available table space of HAM-ISIs. We envision a system using several rotation sensors combined with SPI links to achieve good IFO-beam-direction rotation control for all ISIs. The optimal configuration is still being developed.

TRL 6. CRS prototype operational and has run in vacuum. Noise below 1 Hz is good enough to improve the detector performance, but should be improved with new HoQI laser. HoQI readout is not LIGO UHV ready. The compact 6D is TRL 4 (promising test results in the lab).

Seismic Platform Interferometer. The concept of adding an auxiliary interferometer to LIGO to control the low frequency lengths has been around for many years. Recently, the idea has evolved to a Seismic Platform Interferometer (SPI) which employs a large-working-range interferometer to measure the length, and an optical lever or multiple beams

to measure the angles between adjacent seismic tables. The SPI would be used between the tables in the corner station, but not along the long arms, due to the increased difficulty of the telescopes. Performance of the LISA-pathfinder-style phase meter installed at AEI has been presented in LIGO-T1800282 (better than $2\times10^{-11}\,\mathrm{m}/\sqrt{\mathrm{Hz}}$ and $2\times10^{-10}\,\mathrm{rad}/\sqrt{\mathrm{Hz}}$ at the microseism), and concepts for adapting it to the HAM-ISIs shown in LIGO-G2100582. The performance of the HAM-ISI, when an SPI is included, can be dramatically better than what we see now, as shown in LIGO-G2001539, reducing the relative displacements at the suspension point by at least an order of magnitude at the microseism. This is because the SPI directly impacts the relative translation, and it directly impacts the relative tilts. When this is combined with improved inertial sensing for the vertical direction (see below), the relative angle measurements can be extended to provide absolute angular stability. When combined with several inertial rotation sensors (see above), the SPI forms the backbone of an optically integrated, very low vibration system for supporting the optics in a post A+ interferometer.

TRL 6. In use on 10 m prototype at AEI. Updated prototypes at Stanford and SLAC.

Improved low frequency seismometers for the HAM-ISIs. The low frequency inertial sensing of the HAM-ISIs should be improved, either by improving the performance of the GS-13, or by adding additional sensors. One of the key features of the ISI is that it provides isolation in all 6 degrees of freedom, yet we understand that the most critical is the suspension point longitudinal motion, and this is dominated by the translation and tilt of the optical tables. Compact, high performance, low-frequency inertial sensors are under development which can improve the performance of the HAM-ISIs for these critical DOFs. Unfortunately, the compact rotation sensors are still too bulky to install on many of the HAM-ISIs, so we rely on the angular sensing of the SPI to achieve rotation improvement for many of the the tables. However, the absolute angular performance of the SPI is limited by the differential vertical motion of the separated tables. We desire a *compact vertical inertial sensor* with performance similar to the T240, but a smaller footprint so that it can be installed inside the stage 1 structure (i.e. below the optical table). Once the angular motion is reduced, a *compact horizontal inertial sensor* can then be used to improve the horizontal motion, and to better match the low frequency control used on the BSC-ISIs, again reducing the relative motion in the optical cavities in the corner station.

TRL 5. L-4C with HoQI readout demonstrated [4]. Other sensors are in development.

Install an ISI into HAM1. The excess motion of the optical table in HAM1 is a continuing source of trouble for the interferometer's sensors which are installed there, particularly the REFL WFS signals (LIGO-G2100751). Replacing the passive stack in that chamber with an ISI would be a straightforward, if expensive, solution. This was explored as an option for A+, but despite the benefits for the low-frequency noise (LIGO-T1800369), the lab decided not to pursue this upgrade for A+ due to the cost and schedule, and a plan that the noise could be mitigated with active control techniques (LIGO-M1900052). As the other technical noises are improved, it is likely that the motion of HAM1 will dominate the angular noise spectrum once again, and mitigation will be important. Thus, the choice to install an ISI into HAM1 should be considered again.

Given the smaller payload needed for HAM1, this may be an opportunity to collaborate with the LSC to design a more compact version of a single-stage ISI with a reduced payload. This design update would incur significant NRE costs, but there are several university labs across the collaboration who are currently pursuing high performance isolation systems to support their development work (Birmingham, VU, Stanford, GSSI) and so it would have a broader impact for the GW community.

TRL 9 if current HAM ISI, TRL 5 for redesign version.

5.1.3 Newtonian Noise Suppression

Newtonian gravitational noise will limit the low frequency sensitivity of this detector if other improvements noted in Section 5.1 are achieved. The dominant source of Newtonian noise for the LIGO detectors is due to Rayleigh seismic waves near the test masses [5]. Newtonian noise from other sources are expected to be sub-dominant and should not limit current detectors. As indicated in Fig. 4, the nominal target is a relatively modest suppression of Newtonian noise from Rayleigh waves by a factor of two. The model used for the Newtonian noise curve in Fig. 4 corresponds approximately to the 50th percentile seismic noise level at LLO and LHO. The 90th percentile seismic noise is approximately 4× higher in the 10–20 Hz band, at which point it would start to degrade the A♯ target strain sensitivity. Thus a more ambitious, but useful goal would a suppression factor of 8–10.

While future detectors at new sites with new infrastructure may be able to mitigate Newtonian noise through careful site selection and infrastructure design (e.g. recess structures [6]), those are not practical options for detectors within the current infrastructure.

TRL 3/4

5.2 Upgrades targeting mid-frequencies

In the A+ design, coating thermal noise is comparable to quantum noise in the 50–300 Hz band. Thus the quantum noise reductions proposed for post-O5 will not have full impact at these frequencies unless coating thermal noise is also reduced. In this section we consider options for improving the test mass coatings. For the baseline A♯ strain noise curves, we use the thermal noise projected for GaAs/AlGaAs crystalling coatings (see Section 5.2.2). But the same A♯ sensitivity could be achieved using amorphous oxide coatings if their thermal noise can be reduced by a factor of 2 beyond the A+ target.

5.2.1 Maturation of A+ Oxide Coatings

We have been assuming here that the A+ coatings currently being developed, using titanium-doped germania as the new high-index material, will meet the goal of a factor of 2 reduction in coating thermal noise. At the moment these coatings are not yet proven, and we can't be sure where thermal noise will lie. Further R&D on these coatings is warranted – and on amorphous, metal-oxide films in general. Since the new, larger test masses will need to be coated, even modest improvements in thermal noise or absorption would be welcome.

TRL 4

Recommendation: Research on amorphous metal-oxide coatings should continue beyond

the A+ coating solution, for further improvements of thermal noise, absorption, and scattering. The timescale for this is approximately five years.

5.2.2 Crystalline Coatings

Crystalline coatings made from GaAs/AlGaAs layers offer very low thermal noise; LIGO-G2001592 reports a direct thermal measurement on a small sample mirror that is a factor of at least 5 lower than current ETM coatings (or a factor of at least 2.5× lower than the A+ goal). The challenge is scaling up the process to test mass size, and in a reliable fashion. The status and potential path forward for this development is reviewed in LIGO-G2100466. The current project involves 10 cm diameter coatings, and will look at the coating uniformity: thickness uniformity, absorption uniformity, and coating defects. A hoped-for next step, which comes at a significant increase in cost, is to increase the size to 20 cm diameter and to control the molecular-beam epitaxy process by leasing the chamber continuously for several months – this is believed to be crucial to producing low-defect coatings.

If these development steps are successful, the path to producing test masses with AlGaAs coatings would involve two additional significant investments: procurement of 30 cm diameter GaAs wafers, a standard wafer size in the semiconductor industry, but not for GaAs; and procurement of a custom bonding machine that can handle the test mass. Details on this can be found in LIGO-T2000170.

Some changes would need to be made to the interferometer if AlGaAs coatings were used. The 30 cm diameter is not quite large enough for the current beam size on the ETMs of 12.4 cm diameter ($1/e^2$), so the test mass curvatures would be changed to make slightly smaller beams (the coating mechanical loss is so much lower that it would no longer be important to make the beams as large as possible). The A$^\sharp$ curves using AlGaAs coatings in Fig. 1 are calculated with a 5.5 cm beam radius on the end test masses and a 4.5 cm radius on the input test masses; the more stable cavity geometry this implies ($g_1 g_2 = 0.71$) would be a benefit in terms of reduced sensitivity to misalignments. The curvature of some of the vertex optics would need to change to match to the new arm cavity mode. The other issue is that the Arm Length Stabilization system would need to operate at a different wavelength, as the AlGaAs coatings are opaque to green light. Some initial ideas on using 2128 nm for the ALS beam can be found in LIGO-G2201328.

A workshop on AlGaAs coatings for GW interferometers was recently held (15-17 August 2022, at American University). A summary of the workshop, including findings and recommendations, can be found in LIGO-T2200321. In addition to reviewing the issues mentioned above, the workshop also heard the latest from the community making cryogenic cavities for ultra-stable lasers, work now available in pre-prints [7] and [8]. At low frequencies, 10^{-3} to 1 Hz, their cavities, made of silicon and using AlGaAs/GaAs mirror coatings, show noise above the predicted coating Brownian noise level, by around one order of magnitude (in amplitude). They observe two types of excess noise. 'Birefringence noise' is anti-correlated between the two polarization axes of the resonator; there is no physical model for this noise, so scaling their results for the beam size and light intensity (for which those references report some phenomenological scalings), and for the wavelength and frequencies relevant for LIGO (for which they do not) is a speculative exercise. Below birefringence noise, but above the predicted Brownian noise by a factor of several, is a 'global noise', so-called because its

correlation length is greater than the half-millimeter beam size used in these cavities; there is no physical model for this noise either. Thus unfortunately we cannot establish with any certainty whether either of these noises would be below Brownian noise in the LIGO arm cavities.

TRL 4-5. However, it is unclear how to evaluate the TRL when there remain questions about the underlying physics of the materials.

Recommendation: The August 2022 workshop report (LIGO-T2200321) contains recommended actions, including a plan for the proposed next step in scaling, which is to develop AlGaAs coatings at the 20 cm wafer scale. Experiments to probe the excess noises observed in cryogenic cavities should be devised and performed.

5.3 Upgrades targeting high frequencies

We believe there is room for further reductions in high frequency noise through a combination of higher power and an increase in the level of effective squeezed vacuum. For the former, we foresee continuing the tradition of doubling the stored power in each observing run, to reach 1.5 MW in each arm cavity. For squeezing, the goal is set at 10 dB of broadband, effective squeezing (compared to 6 dB for A+); this is the level of squeezing specified in the design for Cosmic Explorer [9] and Voyager (Section 6.1.3). Reaching these targets will require advances in laser power, mirror coating absorption and/or thermal compensation, parametric instability mitigation, and losses that limit squeezing. These are discussed in the following sections.

We also present an option to change from the normal broadband signal recycling operation to a wideband configuration, which would offer better performance above ∼1 kHz at the expense of poorer performance at lower frequencies.

5.3.1 Increased optical power

Increasing the power circulating in the arm cavities to 1.5 MW in each arm will present the usual suite of high power challenges: Siddles-Sigg angular instabilities; parametric instabilities; thermal distortions and their compensation.

Angular instabilities. Increasing the mass and moment of inertia of the test masses will help control Siddles-Sigg angular instabilites. If the test mass dimensions are simply scaled by $(100/40)^{1/3}$, the moment of inertia will increase by a factor of 4.6; this will more than compensate for the factor of 2 increase in optical torque due to the power increase (compared to A+ design power) – at 1.5 MW the opto-mechanical angular dynamics will be similar to those of Advanced LIGO at 330 kW arm power.

Parametric instabilities. The parametric instability (PI) situation will be worse both because of the factor of 2 increase in arm power, and because the larger test masses will have a higher density in frequency of internal modes of vibration. The design and number of acoustic mode dampers will likely need to change in accordance. Active damping of PIs may be required, using the electro-static test mass actuators or possibly a radiation pressure actuator using an external laser beam. In Advanced LIGO, parametric instability mitigation was an add-on, designed after the O1 run. For A♯, accommodations for PI mitigation will be designed in at

the beginning (e.g., the shape of the test mass could be chosen to minimize PI risk, and to mount acoustic mode dampers in more ideal locations).

TRL 5/6. TRL 6 for current techniques of acoustic mode dampers and active damping via electro-static actuators. TRL 5 for radiation pressure actuation.

Thermal distortions & compensation. Reaching 1.5 MW of power in each arm will require thermal compensation designs and parametric instability mitigation that are targeted to that power level and the larger test masses. Modeling shows that when the power absorbed in the test mass coating is above 0.5–0.6 W (for each test mass), the power recycling gain starts to degrade significantly (see LIGO-G2200743). This is with ring heater correction, but the near-spherical surface change they produce is not a terribly accurate match to the surface distortion produced by the interferometer beam heating. A next generation of ring heater may be needed to more accurately compensate the beam heating – fortunately, research on this has already begun by groups at UC-Riverside and Caltech, see LIGO-G2200399.

The thermal distortion in the ITM substrates will also need to be compensated to greater degree than it has been so far (the distortion in the beamsplitter and compensation plates is much smaller). This is both because of the higher power, and the ambitious A♯ target of 500 ppm loss in the signal extraction cavity (SEC)[6]. Analysis of the effects of thermal distortions on SEC loss and the misrotation of the squeezed state as it propagates through the interferometer, and the required levels of distortion correction, is a work in progress; results will be reported in LIGO-T2200310. In terms of the feasibility of achieving large distortion correction factors, some early modeling indicated they could be achieved with a combination of the test mass ring heater and a suitably patterned CO_2 laser beam acting on the compensation plate (see LIGO-T0900359), but this has not been demonstrated or tested.

Clearly the coating point absorbers that limited power levels in O3 will need to be eliminated or at least significantly reduced. This is also the case for A+, but at this point we do not know well what the absorption characteristics of the A+ (Ti:Ge based) coatings will be. For O4, Virgo is going to be testing an external (to the vacuum) heater, coupled with a binary mask, as a means of compensating for point absorbers – it will be interesting to see how successful this is. The need for further reductions in coating absorption is mentioned in Section 5.2.1.

TRL 3

Laser. The laser power required to achieve 1.5 MW in the arms, assuming a power recycling gain of 50, is 210 W at the power recycling mirror input, which would require a source laser power of 300–350 W. The current design approach of using sequential free-space amplifiers has achieved 195 W, though with a higher-order mode content of nearly 14 % that probably represents the limit of this approach (see LIGO-G2000893). Higher power is possible with a fiber-amplifier, and/or coherent combining of separately-amplified laser beams (see LIGO-G2100481).

[6]For the baseline A♯ design the SEC loss could be up to four times higher (2000 ppm) without significantly degrading the quantum noise (see Fig. 6); it is the A♯ wideband configuration that really requires achieving 500 ppm loss (see Fig. 22)

TRL 6

Recommendations: We recommend that research commence on the optimum shape for a 100 kg test mass including one which will optimally suppress parametric instability. Work will also need to be continued on developing new strategies to suppress parametric instabilities. Significant research should continue on developing TCS systems to combat aberrations that will be caused by very high circulating powers. We recommend that a full scale TCS test facility like that proposed by the Adelaide Group be established. The power circulating in the current generation of detectors will need to be significantly increased to meet O5 goals and much will be learned about suppressing parametric instabilities and thermal distortions in achieving this.

5.3.2 Quantum noise Reduction with improved squeezing

Approaching the A$^\sharp$ target of 10 dB broadband squeezing will require several improvements over the current detectors [9]. We consider as a baseline design using the current 300 m filter cavity in addition to increasing the arm power to 1.5 MW, increasing the generated squeezing, and improving losses and technical noises of all kinds. The quantum noise budget for this baseline is shown in Fig. 6 and a set of parameters that would meet this target is summarized in Table 2. As a rule of thumb, since squeezing is limited to $10\log_{10}(\Lambda + 2\theta_{\rm rms})$ decibels, the 10 dB goal is achieved with total effective losses of $\Lambda \sim 8\,\%$ and total effective phase noise of $\theta_{\rm rms} \sim 10$ mrad.

The dominant broadband sources of quantum noise are losses in the filter cavity, readout chain, and injection path [9]. The losses in the OPO are currently 2 % and only incremental improvements are need to reach the A$^\sharp$ goal of 1 %. There are four passes through Faraday isolators required for the squeezed state injection with an additional pass required for readout. Only minor improvements are needed to reach the goal of 2.5 % loss from the Faradays with the current low-loss isolators achieving 0.5–1 % loss per pass [10]. The improvements needed to the other major sources of input and output loss—steering mirrors, pickoff for the filter cavity, OMC throughput, and photodiodes—are detailed in Table 2.

Loss in the signal extraction cavity, including contributions from mode mismatch, was estimated to be ∼6000 ppm at LLO during O3 (LHO aLOG 58658), which is roughly consistent with the estimate of $\lesssim$ 3000 ppm from [11] which budgeted mode matching losses separately. This level of loss would be equal to the currently dominant injection and readout losses at high frequencies for A$^\sharp$. SEC loss is significant for Voyager Deep and is the dominant noise source for both Voyager Wideband and Cosmic Explorer at high frequencies,[7] and A$^\sharp$ adopts the same 500 ppm loss target as set by both these detectors. SEC loss is even more important for the A$^\sharp$ wideband tuning since it is unaffected by the increased SEC finesse which broadens the bandwidth of the other noises; see Fig. 22. SEC loss of 500 ppm would also limit the enhanced sensitivities around 2 kHz caused by the SEC resonance of both the 655 m

[7] Strain-referred SEC loss is proportional to $\sqrt{\mathcal{F}}$, where $\mathcal{F}$ is the arm cavity finesse, and independent of arm length L at high frequencies. The other dominant sources of quantum noise, injection and readout loss, both scale as $L^{-1/2}$ if the detector bandwidth is kept fixed. Thus, SEC loss becomes the dominant noise source for Cosmic Explorer since it is constant while the other noises are reduced by the 10× longer arms. SEC loss is more significant for Voyager due to Voyager's larger arm finesse. It is true that Cosmic Explorer and Voyager need higher finesse SECs due to their lower arm poles, but this is not the reason that SEC loss is more significant for these detectors: strain-referred SEC loss is independent of SEC finesse [12].

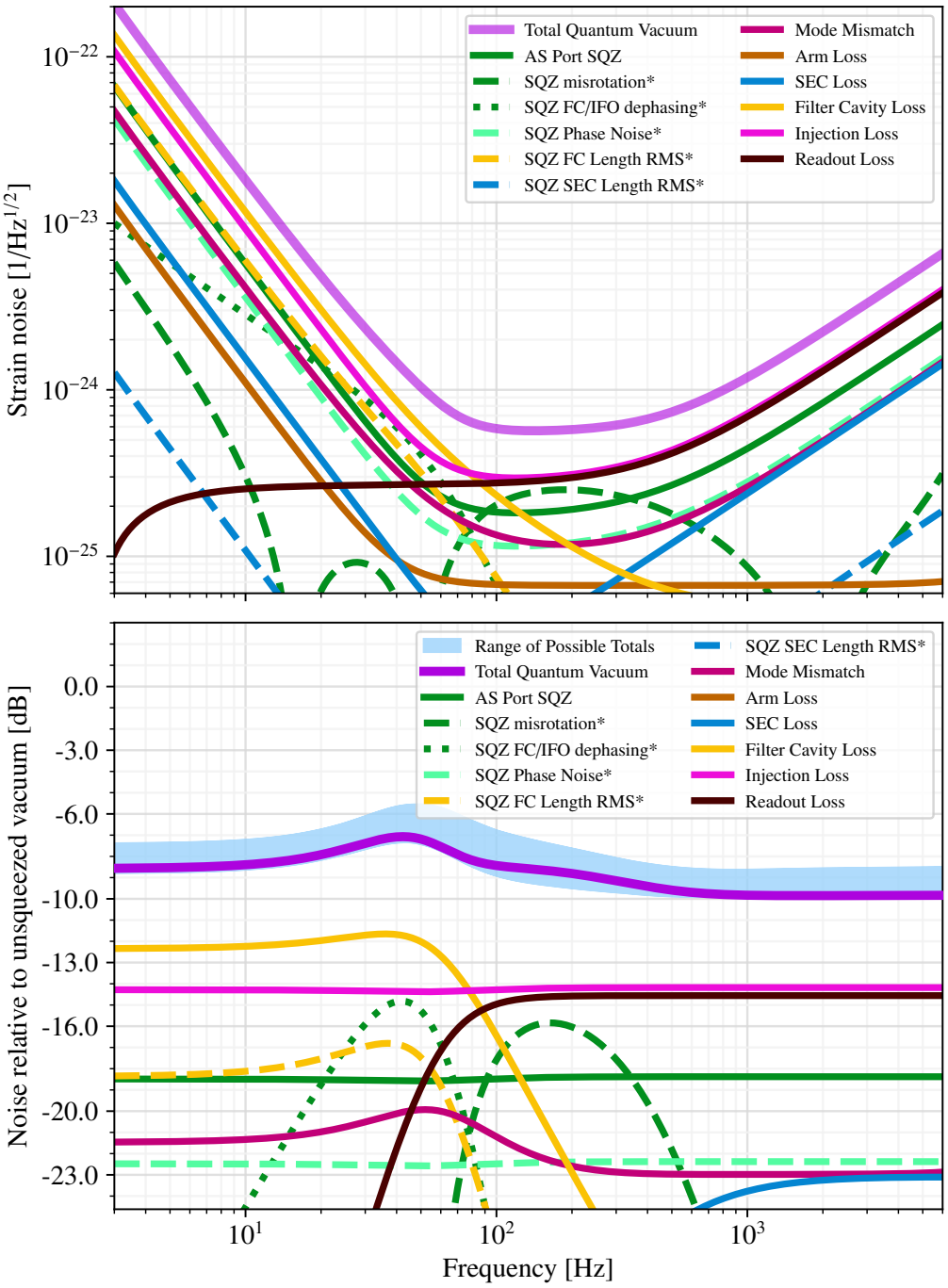

Figure 6: **Top**: Baseline quantum noise budget for A♯ achieving 9.8 dB squeezing at 1 kHz; **Bottom**: the same budget plotted as noise relative to unsqueezed vacuum. The noise due to mode mismatch varies for different relative phases between the higher order modes excited by the various mismatches. The budget shown is for one of the best cases and the light blue band shows the range of total quantum noise achieved for the possible relative phases.

long SEC interferometer and the 12 km folded arm interferometer discussed in Section 5.3.3; see Figs. 24 and 26.

There are several sources of dephasing that must be controlled. The first is frequency independent phase noise, a technical noise, which is assumed to be 10 mrad for A♯. The second is fundamental dephasing caused by imbalanced sidebands experiencing differential loss, or by radiation pressure acting on a lossy mechanical system [11]. The main source of this fundamental dephasing is from the detuned filter cavity where the roundtrip loss is enhanced by the cavity finesse to produce a frequency dependent phase noise around the cavity detuning. This noise is 25 mrad for A♯, exceeding the 10 mrad goal in a small band around 40 Hz. Furthermore, the increased SEC finesse of the wideband tuning requires a lower filter cavity bandwidth, and thus a higher filter cavity finesse, resulting in even more dephasing in this band; compare Figs. 6 and 22.

Finally, the rotation experienced by the squeezed state as it propagates throughout the optical system is a function of the detunings of the cavities it encounters, and thus RMS fluctuations in the lengths of these cavities is another source of phase noise. A study of the length control of the A+ filter cavity found that the residual RMS motion can likely be 0.7–2.5 pm (LIGO-T1800447) and we take the lower value of 0.7 pm for the A♯ requirement, which is not insignificant below ∼50 Hz. A similar analysis should be made for the SEC RMS length noise, but 10 pm is not significant for the baseline A♯. It would be for the 12 km folded interferometer though, as can be seen in Fig. 26.

Mismatch between the optical modes of the various cavities is another source of loss, and each mismatch has a different frequency dependent character. A cavity mode basis mismatch between the squeezer and the filter cavity has the frequency dependence of a filter cavity loss; between the squeezer and the interferometer has the frequency dependence of an injection loss; between the interferometer and the OMC has the frequency dependence of a readout loss; and between the arm cavities and the SEC largely has the frequency dependence of an arm loss at frequencies where higher order modes are not resonant in the arms. Higher order mismatches between the arms and the SEC due to optical path length distortions in the ITMs largely have the frequency dependence of an SEC loss and are likely to be more significant; they will be analyzed in LIGO-T2200310. However, since the effects of these mismatches are coherent, the relative phases between the higher order modes excited by them (e.g. whether they are beam size errors or wavefront phase errors) lead to different interference effects, and the magnitude and frequency dependence of the total loss due to mode mismatch can vary. While the frequency dependence of these mode mismatch losses are the same as the other losses, they do not behave in the same way and must be analyzed separately, e.g. power scattered out of the fundamental due to optical path length distortions between the arm cavities and the SEC is a separate mismatch loss and does not contribute to the 500 ppm SEC loss target.

Moreover, when the squeezed state is scattered into higher order modes due to mode mismatch, it will experience a different rotation than the fundamental and inject anti-squeezing when it is scattered back into the fundamental mode [11]. Mode mismatch can also alter the fundamental dephasing. The net result is that the total quantum noise can vary by of order 1 dB at any frequency depending on these mismatch phases. Active mode matching is thus important in reducing both the magnitude of the mismatches and controlling the relative

	Parameter	Units	A+	A♯	Voyager
	Arm power	kW	750	1500	4000
	Source squeezing level	dB	12	18	18
	Roundtrip FC loss	ppm	40	30	10
	Roundtrip arm loss	ppm	75	75	20
	SEC loss	ppm	3000	500	500
Squeezer and	OPO	%	2	1	1
Injection loss	4 × Faraday pass	%	2	2	2
	FC pickoff	%	1	1	1
	Total injection loss	%	5	4	4
Readout loss	1 × Faraday pass	%	0.5	0.5	0.5
	Output steering	%	1.5	1	1
	OMC and PDs	%	2.5	2	2
	Total readout loss	%	4.5	3.5	3.5
Dephasing	Squeezer RMS phase	mrad	30	10	10
	FC RMS length	pm	0.7	0.7	0.7
	SEC RMS length	pm	10	10	10
Mode mismatch	SQZ/FC	%	0.5	0.25	0.25
	SQZ/IFO	%	1	0.5	0.5
	IFO/OMC	%	2	0.5	0.5
	Arm cavities/SEC	%	2	2	2
Observed squeezing	at 1 kHz	dB	6.8	9.8	9.1

Table 2: Parameters used for quantum noise projections for A+, A♯, and Voyager. The total noise is for one of the best cases for the relative phases between the different sources of mode mismatch; see text and Fig. 6 for details. The mode mismatch budgeted here is for the mismatch between the mode basis of two cavities and does not include higher order mismatch arising from, for example, optical path length distortions which will be analyzed in LIGO-T2200310. Note that the source squeezing level is the idealized and lossless squeezing generated at the source before encountering any losses, including those from the OPO. SEC: signal extraction cavity; OPO: optical parameteric oscillator; FC: filter cavity; OMC: output mode cleaner; IFO: interferometer; SQZ: squeezer.

phases to tune toward the best case, as should be achieved for A+ (LIGO-T1800447). The reduction in the magnitude of the mode mismatches necessary to reach the A♯ targets are given in Table 2. The noise budgets shown in Fig. 6 use mismatch phases resulting in the near minimal possible noise, while the light blue band in the bottom figure shows the range of total quantum noise achievable for the range of possible relative phases.

Since the effects of filter cavity loss prevent A♯ from reaching 10 dB squeezing at low frequencies, one is motivated to consider increasing the length of the filter cavity from 300 m to 4 km by putting it in one of the arm vacuum tubes. Both the filter cavity loss and the fundamental dephasing caused by that loss are enhanced by a factor of the filter cavity finesse and, for the fixed bandwidth needed to compensate the squeezed state rotation in the interferometer, are reduced by increasing the filter cavity length and thus decreasing the finesse. Furthermore, the sensitivity to RMS length fluctuations also decreases linearly as the cavity length is increased at fixed bandwidth. The wideband A♯ tuning is the scenario that benefits most from this length increase where the quantum noise is reduced by roughly a factor of 2.4 in a frequency range around 20 Hz; however, this only leads to a roughly 25 % reduction in the total noise. The gains for the other A♯ scenarios are even more modest[8] and we thus conclude that the option of making a 4 km long filter cavity in one of the arm vacuum tubes is not worth the effort.

TRL 5/6 Squeezed Light Generation, TRL 4/5 Use of Squeezed Light

Recommendations:

Squeezed Light Generation. Although the current approach to generate squeezed light is already adequate to produce high levels of squeezing, degradation of the strength of the nonlinear interaction inside the squeezer PPKTP crystal has been observed in LIGO, GEO and Virgo, caused by the interaction between the crystal and the green circulating power. While the approach in LIGO during O3 was to shift the crystal and use a "fresh" spot after several months of continuous operation, we should assess in O4 if this strategy is sufficient to maintain high nonlinear interaction strength. Moreover, the higher squeezer green pump power needed to achieve 10 dB of observed squeezing will likely accelerate this degradation process, so further studies should be done.

Use of Squeezed Light. Work should continue on reducing RMS phase noise and optical losses of all kinds. An effort should be made to more accurately measure SEC loss in A+ and to make a detailed loss budget of where the losses are coming from, i.e. what fraction from AR surfaces, substrate inhomogeneity, mode matching, etc. Work should also continue on improving active mode matching, both externally with the matching in the input and output optics and internally with the matching between the arms and the SEC. At the moment, we do not think that new technology needs to be developed to achieve a nearly-optimal mode-matching, and work should focus on developing an effective actuation strategy with the actuators newly installed for O4. However, it is possible that in O4 we will learn that specific mode-matching sensors need to be installed, and/or that wavefront actuators able to make mode corrections at higher order (i.e. astigmatism) are necessary. The filter cavity control strategy should be evaluated during O4, and it should be established if it meets the

[8]The total improvement for both Voyager Deep and Wideband using a 4 km long filter cavity is only about 10 %.

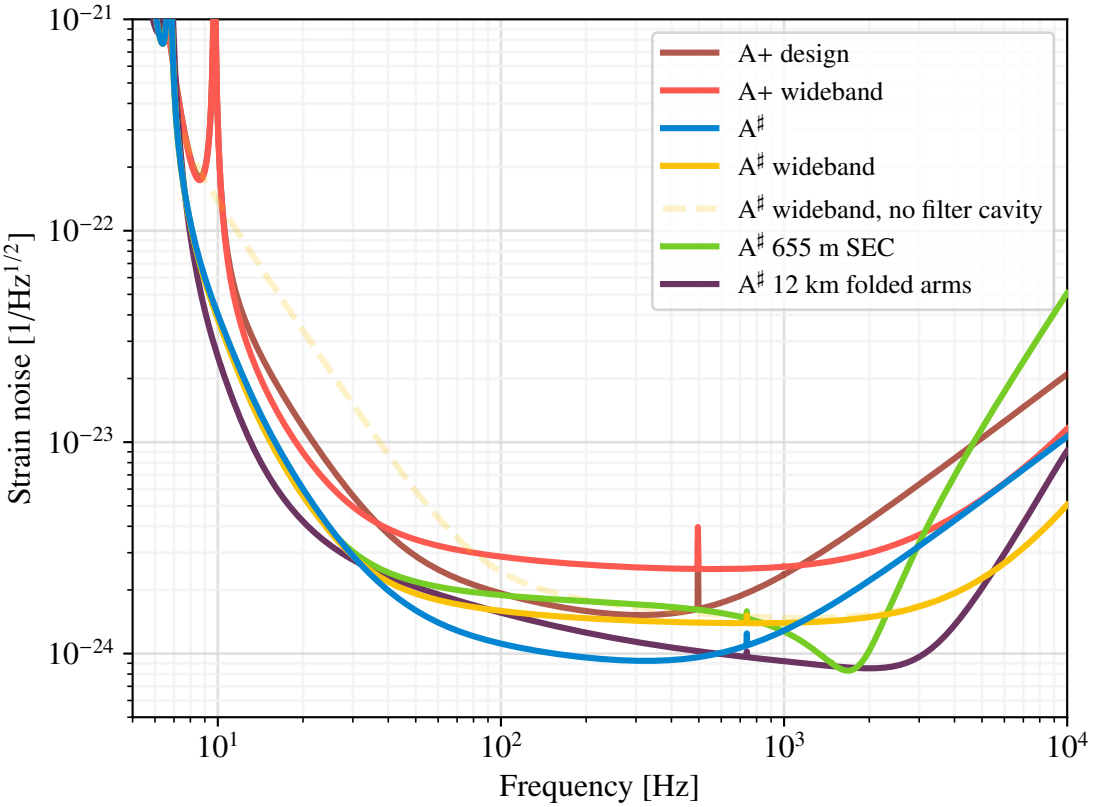

Figure 7: Alternative A♯ tunings. A+ wideband is the tuning proposed in Ref. [2] and A♯ wideband is the same tuning using all of the A♯ upgrades. "A♯ 655 m SEC" increases the length of the SEC from 55 m to 655 m by using the 300 m filter cavity vacuum tube to house part of the cavity and is adapted from the 355 m long SEC proposal from Ref. [13]. "A♯ 12 km folded arms" is the proposal of Ref. [13] to make folded 12 km long arms, updated to use all of the A♯ upgrades (the coating thermal noise is taken from Ref. [13]).

A♯ noise requirements, and if not, which modifications should be implemented. Research should also be done to optimally tune the squeezer parameters throughout the run, so as to always achieve maximum squeezing benefit. As observed in O3 in LIGO, Virgo and GEO, maximum squeezing level is observed only when the system is carefully tuned, with 0.5–1 dB less typically observed for the majority of the run. Quantitative analysis and improved tuning strategies should be studied.

5.3.3 Alternative Tunings

The high frequency sensitivity can also be improved by altering the frequency response of the interferometer. Fig. 7 shows the strain noise for a few options for this type of configuration change. Increasing the high frequency sensitivity in this way does in general give up sensitivity at mid-frequencies. Therefore, one of these options is probably most attractive as an upgrade to a single interferometer in a network where there are at least two (three?) other interferometers providing maximum detection range.

Wideband Tuning The simplest way to do this is to widen the bandwidth by increasing

the level of signal recycling (using a higher reflectivity signal recycling mirror). If injecting squeezing using a filter cavity, its finesse also needs to be increased to manage quantum radiation pressure noise. In Ref. [2] this simple wideband configuration is compared to a narrowband configuration where the signal recycling is detuned in addition to being increased. Although such detuning can lead to lower strain noise over a narrow band of frequencies, Ref. [2] concludes that the wideband configuration is preferred given its relative simplicity and broader noise reduction. The losses in the SEC must be reasonably low for this to be effective since this loss is not broadened along with the other noises; see Fig. 22.

TRL 5/6

Recommendations: As noted in the squeezed light section, it is important to make an accurate measure of the SEC loss and a detailed loss budget, in order to accurately predict the performance of a wideband configuration. With the 500 ppm loss shown in Fig. 7, the A$^\sharp$ wideband tuning is about a factor of two more sensitive than the standard tuning at 3 kHz. The A+ SEC loss level of 3000 ppm results in a factor of about 1.5 improvement over the standard tuning.

A variable transmission signal recycling mirror (SRM) could provide in situ bandwidth control, and such technology should be pursued. Ideally the filter cavity finesse would be tuned in concert with changing the SRM transmission, but a variable transmission filter cavity input mirror is much more demanding in terms of tolerable optical loss. This should also be pursued, but there may be scenarios where, by just bypassing the filter cavity, trading off poorer low-frequency sensitivity for better high-frequency sensitivity (as shown in Fig. 7) is advantageous.

12 km Folded Arms. A more radical approach is to bring the optical resonance that arises from the coupling between the signal recycling and arm cavities into the several kHz regime by folding the arm cavities to achieve an effective arm length of $3 \times 4\,\mathrm{km} = 12\,\mathrm{km}$. This scheme was considered in [13], and the strain noise for it, with the inclusion of all the other A$^\sharp$ upgrades, is also shown in Fig. 7. The coating thermal noise for this case (see Fig. 25) is calculated using the mechanical loss of the A+-design coatings (i.e., not the improved A$^\sharp$ coatings); this option could thus be an alternative if the reduced coating thermal noise assumed for A$^\sharp$ is not achievable, and it is worth looking more at what it involves. The beam radius on the input and end mirrors is 7.1 cm and 6.4 cm on the fold mirrors, which would fit on 100 kg optics (nominally 23 cm radius). The BSC ISI probably could not accommodate two (100 kg) suspensions, but LHO has the extra BSC chambers intended for the H2 interferometer that could house the fold mirrors. They would need to be outfitted with ISI systems.

Recommendations: A detailed assessment of the risks and benefits of the 12 km folded-arm configuration should be undertaken.

655 m SEC. Another way to bring the coupled resonance into the kHz regime is to lengthen the signal recycling (extraction) cavity, rather than the arm cavities. One idea for achieving this is to use the 300 m filter cavity tube to house the SEC; folding the SEC at the end of this tube would create a 655 m SEC length. This variant is included in Fig. 7. We have not, however, considered any practicalities of implementing this design (would it fit in the existing vacuum system? would it be compatible with the filter cavity?).

Recommendations: As Fig. 7 shows, the improvement with this design is modest and limited in frequency. Unless it becomes particularly important to have better sensitivity from 1–2 kHz, the motivation to pursue this option is weak.

We have not assigned TRLs to these last two variants (*12 km folded arms* and *655 m SEC*). Both of them mostly involve additional units of existing designs (or a design which will be part of A♯) – suspended optics and isolation systems. But both variants are more complex than the baseline A♯, and the question is more whether the performance benefit is worth the additional complexity and associated risk. Neither of them is considered to be a candidate for an immediate post-O5 upgrade.

6 Voyager

A more ambitious upgrade to the existing interferometers is LIGO Voyager (the Voyager concept is described in detail in [1]). Voyager largely re-uses the existing Advanced LIGO infrastructure: vacuum systems, controls, seismic isolation, suspensions, and all of the interferometer sensing and control infrastructure. Briefly, Voyager is a dual-recycled interferometer similar to Advanced LIGO but uses 200 kg crystalline silicon test masses, operated at 123 K. The laser wavelength is 2 µm, with 4 MW of power in each arm cavity. Frequency-dependent squeezing is employed at a level of 10 dB of effective squeezing.

The primary advantages of the Voyager concept are twofold: the very high thermal conductivity of silicon, and its effectively zero coefficient of thermal expansion at 123 K mean that thermal effects in the test masses are greatly reduced compared to fused silica; the test mass coatings based on amorphous silicon and silica layers, combined with low temperature operation, are a much lower noise coating than the amorphous metal-oxide coatings used on fused silica test masses. However, there are several technical challenges that require R&D. These are chiefly the fabrication of the silicon test mass optics and coatings. The cryogenic engineering, 2 µm lasers, and high quantum-efficiency photodiodes are more straightforward, low-risk development projects.[9]

Voyager is clearly a larger scale upgrade than those discussed in Section 5. It is not an all-new interferometer, however; nearly all of the essential features: vibration isolation, quad suspensions, DRSE, BHD, Squeezing, ALS, TCS, etc. have all been tested in Advanced LIGO or will be tested in A+. Voyager adopts all of these techniques, making the appropriate changes for silicon and 2 µm laser light. The main risks/unknowns are in the use of silicon as a mirror material, and the operation at low temperature (but not truly cryogenic like KAGRA). These risks can be significantly retired in the lab-scale prototypes.

Since any post-O5 upgrade would be replacing operational interferometers, the technology must be relatively mature before it can be proposed as a viable project. The Voyager team is in the process of both assessing the technical readiness levels of the underlying technologies, and establishing the criteria for achieving a TRL of 5 or 6 for each, as done for the A$^\sharp$ upgrades described in Section 5.

6.1 Recent Changes in the Design

There are a handful of design choices which have been made since writing of [1]. In this section we describe briefly those items.

6.1.1 Laser Wavelength

A significant change has been the decision to move away from the 2128 nm wavelength (chosen mainly to allow laser seed generation by downconversion from 1064 nm) to 2050.15 nm. This choice was made mainly to reduce the absorption of the light in the silica optics (IMC, BS, PRM) [14].

The slightly shorter wavelength also marginally reduces free carrier absorption in bulk sili-

[9] A FAQ for Voyager can be found here: https://git.ligo.org/-/snippets/89

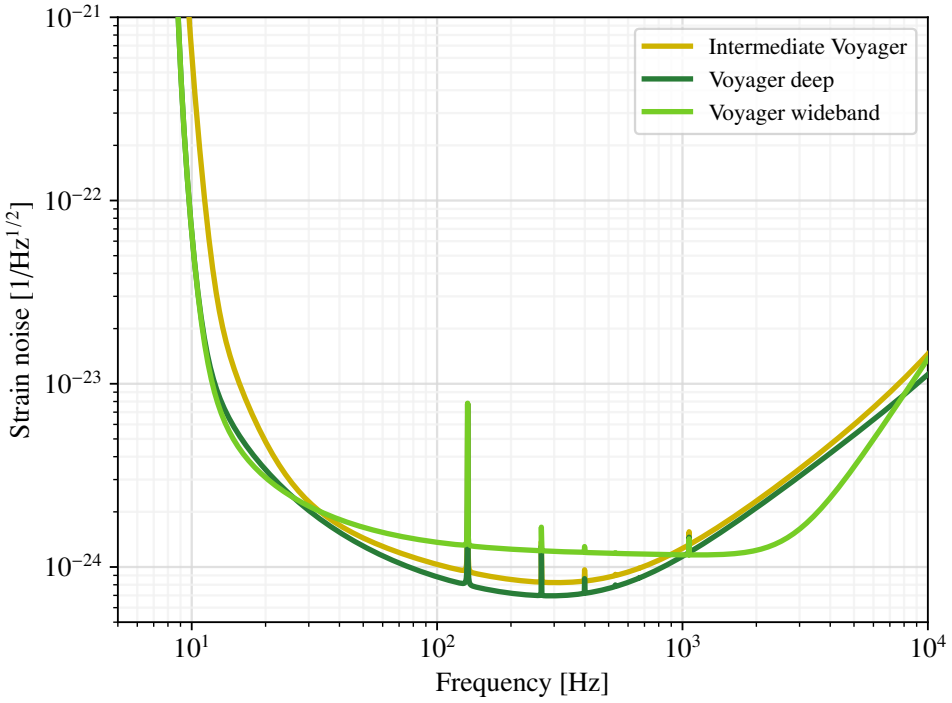

Figure 8: Comparison of Voyager configurations. The "deep" configuration maximizes the BNS range, the "wideband" configuration maximizes the sensitivity above 1 kHz, and the "intermediate" configuration compromises the sensitivity somewhat in order to minimize certain technical risks.

con [15], and marginally increases absorption in amorphous silicon coatings [16].

The new wavelength has the added benefits of missing the broad water absorption bands (for the out of vacuum optics) as well being popular in the laser/optics community for use in atmospheric CO_2 sensing. As such, there are, as of this writing, several commercial vendors (e.g. Thorlabs) producing lasers, optics, and electro-optics catering to this wavelength band. High power CW fiber amplifiers (Thulium and/or Holmium based) have been demonstrated with output powers > 200 W at 2 µm.

6.1.2 Configurations

A new family of Voyager configurations has been designed, focusing on "deep" and "wideband" observing scenarios, as well as an "intermediate" configuration that defers certain technical risks. Sensitivity curves for these configurations are shown in Fig. 8.

The "intermediate" configuration is targeted to minimize the R&D needed to prepare for the first Voyager observing run. The size of the ITMs and the beam spot size are decreased, to reduce the risk of procuring large silicon substrates. The HR coatings use proven low–absorption materials in the top few layers,[10] to mitigate any excess a-Si absorption. The bottom suspension stage uses metal blade springs in lieu of silicon blades. Seismic motion is assumed to be the same as aLIGO, and Newtonian gravity noise is canceled less aggressively.

[10]The thermal noise of this mixed coating is roughly estimated, not modeled in detail.

The "deep" and "wideband" configurations differ from each other only in the SRM transmittance, and the squeezing filter cavity mirror reflectivities.[11] In the "deep" configuration, the SRM transmittance was optimized for BNS inspiral range. In the "wideband" configuration, it was chosen to optimize sensitivity above 1 kHz.

Both configurations adopt the same arm cavity finesse, chosen as a compromise between mitigating the noise contribution of SEC loss at high frequencies, and the contribution of ITM thermo-refractive noise at low frequencies. By optimizing the arm finesse for each observing scenario individually, it would be possible to obtain a further improvement in the sensitivity. However, it would then be necessary to modify the PRM and ITMs, in addition to the SRM and filter cavity, when changing between the configurations.

6.1.3 Squeezing

An increased level of input squeezing is assumed for the A♯ and Voyager configurations, together with reduced input and output losses. Squeezer parameters are summarized in Table 2, and the resulting level of observed squeezing is shown in Fig. 9.

For Voyager, the squeezed light will be at 2 µm, the same as the main laser. Squeezing at ∼2 µm has been demonstrated (e.g. [17, 18]) at audio frequencies at the level of 11 dB.

In order to best exploit the squeezed light, the losses in the squeezing injection and GW readout path need to be very low. In most cases, we expect the scatter losses to be 4× lower than they are at 1 µm. This scaling law favors 2 µm, but only for mirrors. Most significantly, we expect the thermal distortions in the ITM/SEC, which most likely would limit squeezing for room temperature, fused silica mirrors, to be reduced by a large factor in Voyager, as compared to A+/A♯ as discussed in Section 6.3.

Two significant sources of loss, where neither the high thermal conductivity nor the longer wavelength help, are the Faraday Isolators (in the squeezing injection and GW readout paths) and the high QE PDs to read out the GW signal in the Balanced Homodyne Readout.

6.1.4 Higher Power

It is assumed that the ITM heat budget can be relaxed by about 50 %, via some combination of increased surface area for radiative cooling, reduced ITM thickness, and decreased ITM substrate absorption. (The latter two are also necessary to achieve the SEC loss target.) Accordingly, the input power is increased to 200 W.

In the deep configuration, the benefits of a power increase are marginal due to the presence of noise limits other than quantum noise; almost the same BNS range can be achieved without it. The wideband configuration takes full advantage of the reduced quantum noise at high frequencies.

6.1.5 Silicon Beamsplitter

The optical absorption in silica (and most glasses) rises steeply with increasing wavelength above 1.5 µm, mostly due to multi-phonon mediated excitation of the Si-O bond. This high absorption drives the laser wavelength choice to < 1.9 µm, which is unacceptable due to the

[11] Our experience in swapping SRM transmittance in aLIGO, was relatively benign, so we expect there to be minimal downtime in re-commissioning the interferometer after such a change.

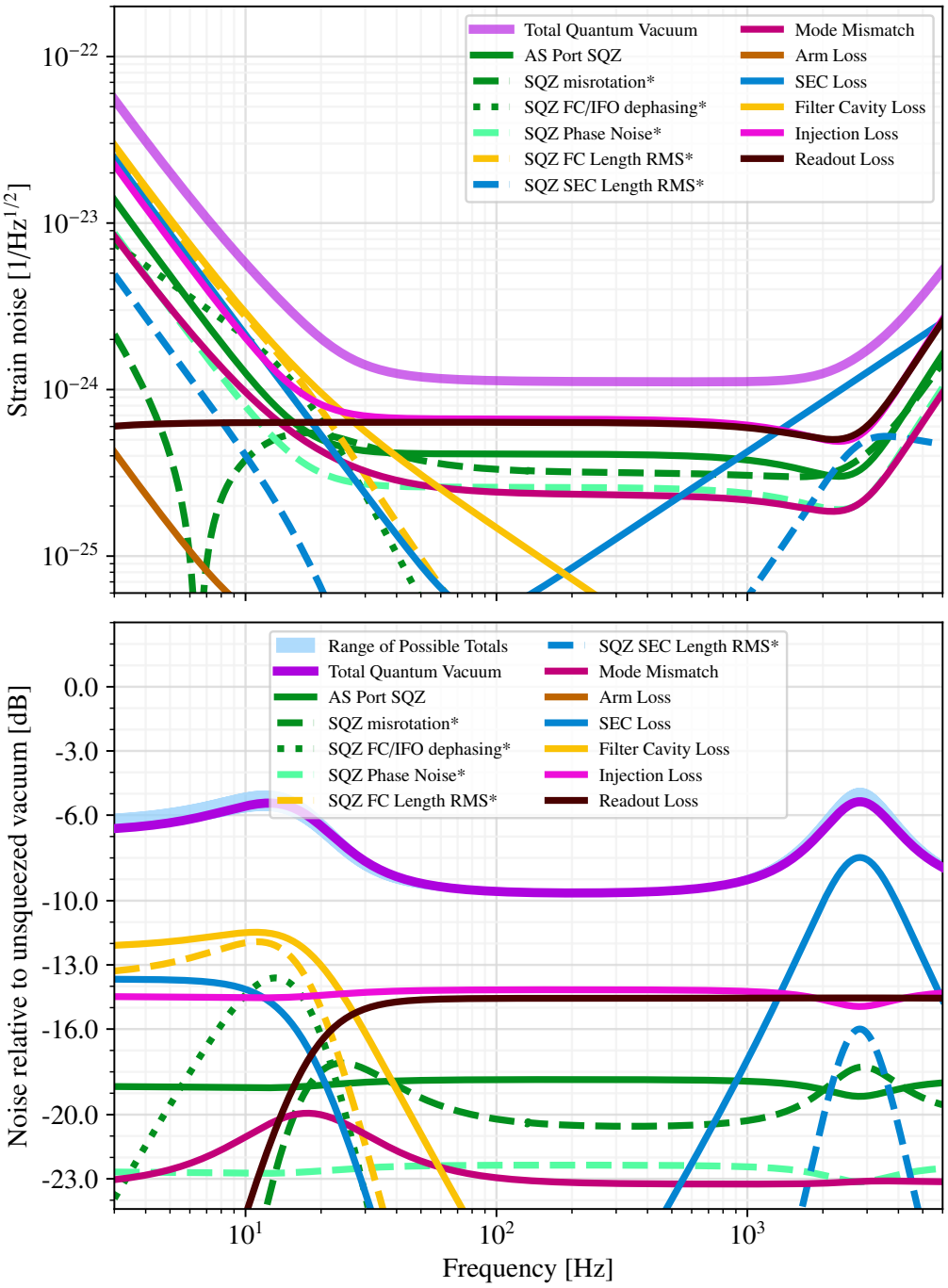

Figure 9: **Top**: Baseline quantum noise budget for Voyager Wideband achieving 9.0 dB squeezing at 1 kHz; **Bottom**: the same budget plotted as noise relative to unsqueezed vacuum. The noise due to mode mismatch varies for different relative phases between the higher order modes excited by the various mismatches. The budget shown is for one of the best cases and the light blue band shows the range of total quantum noise achieved for the possible relative phases.

high absorption in the a-Si HR coatings.

Instead of glass, the Voyager baseline now includes room temperature crystalline silicon as the beamsplitter material. The substrate would be cut at 45 deg from a ⟨100⟩ orientation silicon boule. This geometry would have no first order birefringence, and the absorption is low enough, even at room temperature. Issues to investigate include manufacturability, static birefringence due to gravity, photothermal birefringence, and index homogeneity.

6.2 Seismic Platform Weight Limits

The existing BSC-ISI platforms were engineered to be able to handle the additional mass that comes from having a FM (folding mirror) suspension or a TMS (Transmission Monitor Suspension). Since we no longer plan to have a second interferometer installed at the LIGO Hanford site, there is some additional capacity to have a heavier suspension there, especially if the ITM suspension is moved to the center of the ISI platform.

For the ETM ISI, there is a similar weight savings due to the TMS residing in a separate chamber. The Voyager TMs will be enclosed by cryogenic baffles, and the connection to the TMS and the ALS laser will be made through cold windows[12] (cf. Fig. 10).

The TM's mass is 200 kg and the total mass of the suspension main chain is 520 kg ($2.6\times m_{\mathrm{TM}}$), compared to 3× for aLIGO, and 4× for A♯. Considering the level of the various suspension/seismic noise sources, the mass distribution of the quad does not necessarily need to be optimized with respect to vibration isolation. There is also some margin to further reduce the mass of the upper stage with a slight, concomitant increase of the seismic noise. However, the direct contribution of seismic noise in the observation band is minimal.

The mass of the reaction chain can be significantly lighter than the main chain without significant disadvantages. The main drawback is actuation nonlinearity[13] (bilinear coupling) due to the increased variability of the actuator operating distance. This effect, however, is negligible for the TM/ESD, where the noise requirement is most severe.

Thus, the combined mass of both chains is less than 700 kg and can be further reduced if necessary. Considering these factors, it is clear that **the Voyager TM suspensions will fit within the weight limits of the existing ISI** (1000–1100 kg).[14]

The remaining weight margin is used for the suspension cages and other structural setups. Regarding the weight increase by cryogenics, only the inner shield around the suspension chains is attached to the suspension cage (cf. Fig. 10). The outer shield and the outer shield tubes are rigidly mounted on the vacuum chamber and the main beam tube. The inner shield tubes will be suspended from the main beam tube. Therefore, only the inner shield near the mirror is added to the ISI weight budget.

[12] Similar to the existing cold windows used in our prototypes: optical quality viewport with high absorption in the MWIR and LWIR, and a high transmission in the NIR. These windows are conductively cooled via attachment to the cryogenic shields.

[13] Brett Shapiro, private communication (2022)

[14] cf. LIGO-E1000032 and LIGO-G2102249.

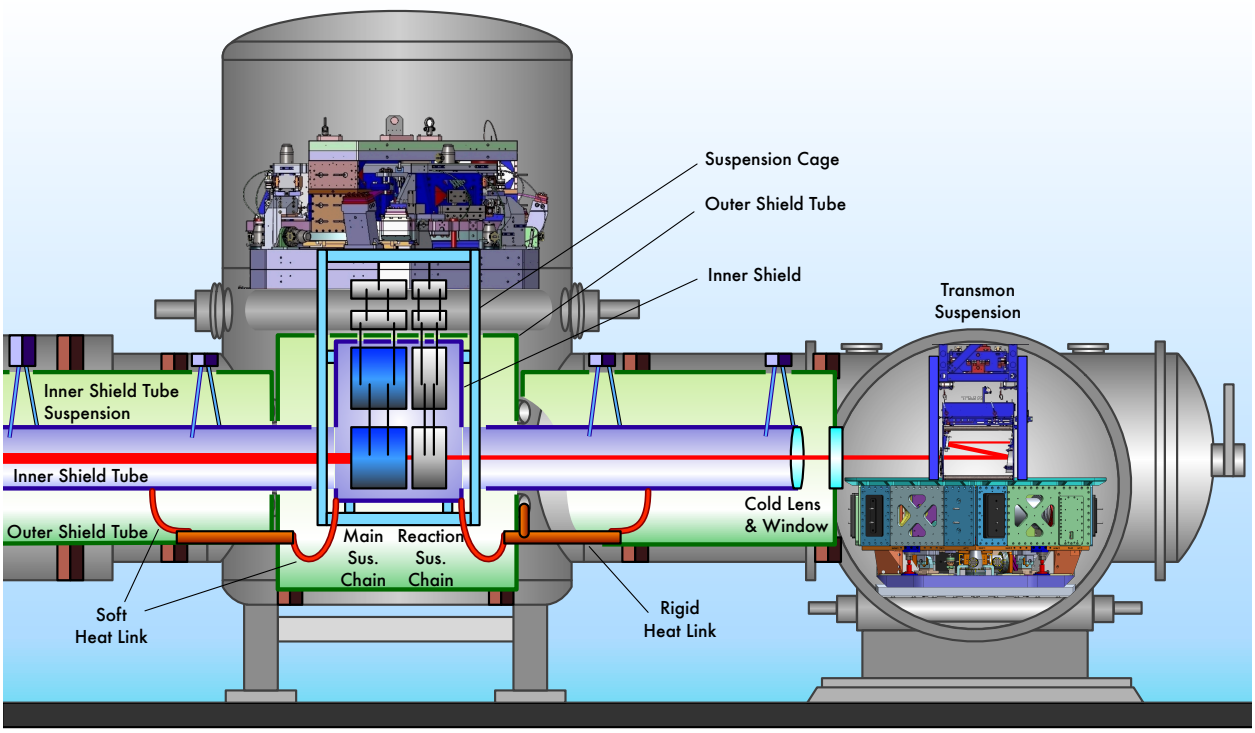

Figure 10: Sketch of the ETM chamber configuration for Voyager. The TMS will be accommodated in an independent chamber (TBD). The main TM chain and the reaction chain are suspended from the BSC-ISI. The suspension cage and inner shield are rigidly attached to the BSC-ISI. The outer shield and the outer shield tubes are rigidly mounted on the vacuum chamber and the main beam tube. This allows us to use thick, high thermal conductance connections for the main heat extraction path to the cryo-cooler. The inner shield tubes are suspended from the main beam tube. Soft copper links are used to extract the heat from the inner shield and the inner shield tubes. The hot radiation from the TMS is blocked with cold windows.

6.3 High Power Issues

The extremely high thermal conductivity and near-zero thermal expansion coefficient of silicon provide considerable advantages in terms of power handling compared to fused silica. In particular, the issue mentioned in Section 5.3.1 of thermally-induced optical distortions in the substrates and the resultant loss created in the SEC and misrotation of the squeezed state (both of which increase the quantum noise, c.f. Section 5.3.2) is significantly reduced in silicon. As noted in Section 5.3.1 the analysis of this effect is still in progress, and will be detailed in LIGO-T2200310. But it is clear that these thermally-induced SEC losses and squeezed state misrotation would be much lower in Voyager, and would likely not require large correction factors from the thermal compensation system (TCS).

The Voyager TCS calls for room temperature silicon compensation plates (CPs) in each arm, placed approximately 5 m from the ITM (close to the BS). This minimizes radiative coupling from the CP to the ITM. The compensation profiles will be provided by laser heating similar to A+. Absorption of visible light in silicon opens up options for shorter wavelength lasers as the heat sources (which may have better properties than CO_2 lasers).

Additionally, all of the Voyager configurations are essentially immune from point absorbers in the test mass coatings. Silicon's high thermal conductivity and near-zero coefficient of thermal expansion at 123 K mean that any point absorber will produce only a negligible distortion of the test mass surface, and thus negligible additional arm cavity loss.

6.4 Scattered light

With the longer laser wavelength, a significant reduction of the scattered light noise is expected in Voyager.

The Voyager test mass is surrounded by a vibration-isolated inner shield and suspended inner shield tubes. These inner shields serve double duty: they absorb the far-infrared radiation from the mirror for radiative cooling, as well as trapping light scattered from the mirror surface into wide angles. By ensuring that there are no heat leaks in the radiation shield, we should also be cutting off paths for scattered light to hit the vibrating chamber walls.

The use of longer wavelengths also provides Voyager an advantage in the process of generating, backscattering, and recombining of the scattered light. The power loss in the scattering process is proportional to $1/\lambda^2$ per scattering surface (cf. Flanagan and Thorne, LIGO-T940063). This reduction of the scattered field takes places at three points: the generation of scattered light at the mirror, backscattering from the nearby surfaces (e.g. vacuum chambers), and recombination of scattered light at the mirror. **We can expect a $\sim$4$\times$ reduction in the scattered light induced strain noise as compared to the 1 µm case.**[15]

The fringe wrapping, due to large amplitude motion at low frequency, has a corner frequency, $f_{\rm corner} \propto v_{\rm scat}/\lambda$. So the upconversion due to this effect will be reduced dramatically, since the noise falls very steeply above the corner frequency [19].

[15] The phase modulation produced by the motion of the backscattering body is also improved by a factor of $1/\lambda$, but this effect is cancelled because the same factor is applied to the phase modulation produced by the gravitational wave signal.

System	TRL	Comments	Effort Req'd	Fund Req'd
TM Substrate	3	absorption, annealing	5	5
TM HR coating	3	absorption, Q	5	3
TM Emissivity	5	barrel treatment (PI)	3	2.5
Quad Suspension	3	cold blades, ribbons, controls	4	4
Ice formation	-	prototype tests	3	3
Squeezing	5	increase existing SQZ level	2	2
High QE PD	3	HgCdTe (UWA), InAsSb (JPL)	4	2
ISC components	4		1	1.5
ALS	4	1550 nm laser, comb	2	2
Parametric Instability	6	more unstable modes + better damping	2	1
PSL	5	new laser	3	3
IOO	6	EOM / FI	2	3
SEI	8	use A+ ISI	1	1
Cryogenics	5	modeling, prototyping	3	3
Misc sensors	6		2	3

Table 3: TRLs for the major Voyager Technologies

6.5 Technical Readiness Levels

Here we describe the Technical Readiness Levels (TRL)[16] for LIGO Voyager. There are several areas where the work done for A+/A♯/Voyager are similar in approach and objective. Those for which the risk will be retired in A+, we will assume can be elevated to TRL 6 or 7 after the success of A+, depending on the overlap between A+ and Voyager.

Almost none of the Voyager sub-systems are at TRL 7, which we would define as demonstrated low noise operation in a suspended cryogenic interferometer. A system which is well tested in aLIGO, and only needs moderate modifications for Voyager, we would describe as TRL 5 or 6.

Test mass substrate

At present, the most challenging requirements for the test mass substrate are its large diameter (45 cm), and its low bulk absorption at 2 µm (below 20 ppm/cm). Both of these requirements have been met in isolation: in silicon crystals grown by the magnetic Czochralski (MCZ) and float zone (FZ) processes, respectively [20, 21]. The challenge for the test mass substrate is to satisfy both requirements simultaneously – we expect to work closely with our Einstein Telescope colleagues on mirror substrate and coating technology.

The most direct route to achieve this would be to mitigate the excess absorption that sometimes occurs in MCZ silicon crystals. The most probable mechanism for the excess absorption arises from the presence of free charge carriers, contributed by clusters of oxygen atoms that are found as impurities in the MCZ material [22].

In wafers of MCZ silicon, a rapid annealing treatment is known to disrupt the oxygen clusters and largely eliminates the resulting free carrier population [23]. For Voyager, we need to find out whether a similar procedure can consistently achieve low absorption in a test mass sized crystal. Preliminary studies done by Stanford, U. Florida, and Caltech have found

[16] See Appendix B for TRL definitions

absorption levels as low as 2.5 ppm/cm in macroscopic pieces of MCZ silicon, and rapid annealing has been shown to suppress excess absorption by factors approaching 100 (LIGO-G1700480, LIGO-G2200909). The sensitivity of MCZ silicon's absorption to thermal history in the 450 °C range would also impose constraints on subsequent coating anneals.

Test mass HR coating

The HR coating needs to satisfy simultaneously a low mechanical friction and a low optical absorption requirement. The baseline design is to use amorphous silica and amorphous silicon. Although, the mechanical loss requirement has been satisfied at 123 K, the absorption needs to be reduced even further. Work in the LSC OWG has shown that one can get low absorption a-Si thin films with high energy IBS, high temperature growth, and hydrogenation.

Test mass emissivity

Ray tracing calculations, based on estimates of the transparency of high resistivity silicon at the peak thermal wavelengths for 123 K, suggest that the Voyager test mass is big enough that the emissivity of any uncoated surfaces will be high ($\sim$0.7), as limited by the prompt reflectivity of the surface. This will be confirmed in the ongoing silicon emissivity measurements, as well as in the Mariner prototype. The emissivity of the test mass's HR/AR surfaces will be modified by the optical coatings applied to those surfaces. This effect also needs further study.

Cryogenic Suspension

The Voyager suspensions will be direct copies of the aLIGO suspensions, with the exception of the TM Quad suspensions. The challenges in the cryogenic quad suspension mechanics are the pendulum material – primarily silicon ribbon, the silicon blade springs for the cryogenic penultimate stage, and silicon bonding. For both the pendulum material and the blade springs, increasing the strength of Si to the level of GPa will become a design advantage from the currently-used value of 100 MPa. The production of silicon ribbons/fibres is not yet a common technology, but we expect to work closely with the Einstein Telescope team and adopt a common technology. The mechanical strength, as well as the mirror and suspension thermal noise due to the material and bonding, will need to be fulfilled together.

Cryogenic displacement sensors for OSEMs have been in progress and have seen no major problems.

Ice formation

Warm steam from the main vacuum system can adsorb onto the HR surface of the mirror. This has been observed in KAGRA, but it seems that this should be manageable by engineering a small enough solid angle of warm vacuum visible by the HR surface of the mirror. The extensive cryogenic shielding around the mirror would be < 80 K, whereas the mirror surface would be $\sim$123 K. The expectation is that only the water molecules which ballistically reach the mirror surface, in a single shot from the warm volume, are able to participate in the ice formation process. Estimation of formation rate and problem level is ongoing, and will be confirmed in a relevant setting as part of the Mariner prototype.

Squeezing

Squeezed light at 1984 nm has already been demonstrated by the ANU [17]. There were no major problems with the demonstration except the reliability of the 2 µm laser. It is expected that the generation of squeezed light at 2050 nm at the required level will be straightforward based on decades of experience in the community.

High Quantum Efficiency Photodiodes

At the moment, there are no photodetector materials which simultaneously meet all of the requirements of a high QE photodetector for the BHD/GW readout: high QE, high power, low $1/f$ noise, and high spatial uniformity. Research for two materials, however, is very promising.

HgCdTe [24] is well established and developers are confident that it can easily achieve the required QE, however, the power handling is an issue that needs to be resolved. QE measurements on HgCdTe imaging arrays (similar to what is used on the James Webb telescope) yield results that are equivalent to 100 % QE, within the error bars of the measurement [25].

InAsSb in an nBn structure [26] is a promising alternative – the power handling does not appear to be an issue but the maximum QE is still hypothetical: a 90 % QE has been demonstrated on first generation devices. These are being developed and tested in collaboration with JPL, with the expectation that 95 % is easily achievable. It remains to be seen if InAsSb can be made with sufficient QE.

ISC components

Interferometer Sensing and Control for Voyager will share many components with aLIGO. The opto-electronic interface needs the consideration of the wavelength change. For RF photodiodes, where $1/f$ noise is less problematic, we may be able to assume that large-diameter exInGaAs PDs are applicable. Their performance needs to be confirmed. WFS require reasonably fast large-diameter QPDs, but they are not commonly available in the market. This can be resolved by working with vendors to make a custom run, as was done for the Bull's Eye QPDs for iLIGO [27]. PD/QPD for DC applications should be investigated in detail too. There, $1/f$ noise must be sufficiently suppressed. There is still room to consider whether to cool the elements to accomplish the suppression, or not.

ALS

An arm length stabilization scheme utilizing the phase locking of 2050 nm and 1550 nm lasers nonlinear optics and low-cost frequency combs, has been designed. This will be tested in the Mariner prototype in 2023. We are forced to use wavelengths longer than 1300 nm to avoid the absorption in silicon. This scheme will be similar to the concept proposed in Section 5.2.2 for A$^\sharp$ with crystalline coatings. Almost all of the ALS system will be a direct copy of the aLIGO scheme, with only the wavelength intercomparison as a new feature.

Parametric Instability

A preliminary analysis of the acousto-optic parametric instabilities (cf. the Voyager Whitepaper LIGO-T1400226) indicates that there would be a few dozen unstable modes at an operating power of 3 MW, in the case where no damping (passive or active) is applied to the

mirror.

As described in Section 5.3.1, a combination of active damping with enhanced passive damping will be studied over the next few years. This approach blends nicely with engineering the Voyager mirror barrels with high emissivity surface treatments.

PSL

Many aspects of the aLIGO PSL sub-system will be re-used: FSS, ISS, PMC, Reference Cavity, EOMs, etc. All of the optics will be replaced with 2 µm optics, but the mechanics, electronics, and software will not need to change. The high power laser will require significant effort to develop and characterize.

Several high power lasers around 2050 nm have been demonstrated, although not yet with the desired linewidth. The Voyager team is evaluating a few seed laser possibilities at 2050 nm offered by low-noise laser vendors (includes DPSS lasers, similar to the NPRO and diode lasers, similar to the RIO Planex). These are comparable in frequency and amplitude noise to the existing Innolight NPRO lasers in the aLIGO PSL.

Fiber laser amplifiers that can deliver > 200 W CW at 2050 nm, are commercially available, but none have been tested yet at the reliability levels required for the LIGO PSL. The Mariner prototype will be testing a $\sim$40 W amplifier towards the end of 2023.

As all previous interferometers have done, we expect to slowly increase the laser power over the first few years of commissioning, adopting the best technology at the time it is required. Recall that aLIGO has never been operated with the full design laser power (as of this writing – 7 years after first lock).

IOO

Faraday isolators, EOMs and AOMs already exist for this wavelength. Some small amount of work is expected to be required here to make custom units to our exact specifications. There are some differences in the photo-elastic constant, Verdet constant, and electro-optic coefficient for these devices, but nothing very different from the 1 or 1.5 µm items.

SEI

Section 6.2 describes the issues with the cryogenic suspension and the ISI. We expect there to be no weight related issues, and centering the cage on the table should not impact the moment of inertia too much, since the ballast masses will be removed/reduced.

It remains to be seen how cold the ISI will get. In preliminary SUS tests on a $\sim$1 m^3 cryostat, there was no significant cooling. The Mariner prototype will characterize the cooling of the stack table top so that this can be considered when predicting the impact on the ISI.

Cryogenics

The low temperature used in Voyager is not an extreme cryogenic temperature; it is $\sim$2.5$\times$ lower than room temperature, whereas a true cryogenic instrument like KAGRA or ET operates at 10–20 K. The mild cryogenics required for Voyager can be handled with a closed cycle cryo-cooler and 2 layers of radiative shielding. This radiative cooling approach has been in use in the Caltech cryogenic interferometry labs since 2011, albeit on flexible cantilever

and fixed spacer cavities, rather than suspended Fabry-Perot cavities.

The main challenges in the cryogenics are the surface treatment of the mass (described above) and the procurement of a baffling coating that absorbs well in the far infrared. These will require some development effort but are mostly straightforward.

Misc sensors

Imagers capable of sensing 2 µm are indispensable for regular optics work as well as beam shape monitoring. The imagers are usually based on extended-InGaAs or HgCdTe and are quite expensive ($5k per unit). Their performance has not been evaluated yet. The equivalent item of an IR sensor card exists, but it is substantially less sensitive than the 1 µm equivalents.

6.6 Voyager Prototype: Mariner

In order to perform integration testing of the Voyager concept, a prototype interferometer designated 'Mariner' is under construction and expected to start installation in early 2023.

6.6.1 Prototype Description

The Mariner prototype, LIGO-T2100014, is planned as a scaled down version of Voyager (cryogenic silicon test masses, amorphous silicon coating, and a 2050 nm laser wavelength) using the existing Caltech 40 m facility. Before Advanced LIGO, the Caltech 40 m prototyped controls schemes and operations for that interferometer. Mariner is intended to do the same for Voyager. The prototyping is divided into two phases:

- Phase 1: "quick and dirty". This is a simpler configuration consisting of a Fabry-Perot Michelson without recycling cavities. The focus will be initial control of the IFO at 2 µm and operation of the cryogenic cooling system. The test-masses are approximately 5.8 kg silicon test masses with a-Si HR coatings. The barrel coatings will be the highest emissivity coatings that we can quickly achieve. The input laser power will be approximately 5 W. There will be no squeezing. We will also investigate any issues associated with ice forming on the test masses due to cryogenic operation.

- Phase 2: "lower noise". An upgraded version of the Mariner prototype will be tested in late 2024/early 2025. The configuration will be a full dual-recycled Fabry-Perot Michelson with higher emissivity coatings on the barrels of the test masses. If possible, we will go to higher input laser power (approximately 10–20 W). This configuration will potentially include squeezing. In addition to implementing lessons from Phase 1, the R&D focus will shift to low noise investigations, full controls of a dual-recycled Fabry-Perot Michelson, and optimization of the cryogenic cooling system.

Due to the scaled down physical size of the Caltech 40 m, there are some fundamental limitations to Mariner. Briefly, these are:

- No full-size suspensions or test masses.

- Smaller test masses lower the maximum radiative cooling due to a smaller surface area. This will prevent simultaneous high power testing and low temperature operation. The Mariner heat budget will not be a 1:1 facsimile of full Voyager.

6.6.2 Risks Retired by the Prototype

Mariner Phase 1 and Phase 2 will retire multiple risks associated with Voyager, mainly through sub-system and integration testing. Some of these will be *retired* and others may require *additional R&D work*. A representative list of risks explored is:

- Silicon issues
  - Absorption in silicon and SiO2
  - Birefringence (in substrates)
  - Demonstration of polishing of test mass demonstration to required tolerances. Exploration of what those tolerances are.
- Cryo Engineering issues
  - Cryo coolers
  - Seismic isolation of shields
  - Emissivity of coatings and silicon and confirmation of thermal modeling of test mass and environs.
  - Risk of ice formation on mirror surfaces investigated
- Demonstration of medium power 2 µm laser
  - Frequency stabilization
  - PMC locking
  - Intensity stabilization
- Control of 2 µm cavities
  - Locking 2 µm mode-cleaner and FP cavities
  - Practical length and alignment control of cryogenic test silicon masses at 2 µm including some semiconductor issues.
  - Demonstration of 1550 nm Arm Length Stabilization (ALS) system locked to 2050 nm laser via frequency comb

7 Post O5 science

We base the science case on our understanding of the astrophysical population after the third observing run [28]. We focus on studying how key high-confidence scientific outcomes (given the types of sources we have observed thus far and our understanding of their astrophysical rates) vary between the detector configurations being considered. In Section 7.1 we compare the redshifts of the mass-dependent horizon, as well as the potential of each configuration to provide early-warning alerts to the astronomical community; Section 7.2 presents the plausible range of catalog sizes for each configuration; in Section 7.3 we explore the sensitivity of each configuration to higher-order mode content in BBH signals; Section 7.4 compares the sensitivity of each configuration to BNS post-merger signals.

7.1 Horizons, Ranges, and Early Warnings

To assess the relative sensitivity to compact binary mergers we first compare the redshifts at which optimally oriented (i.e., face-on) and located (i.e., over-head), non-spinning, equal-mass binaries over a range of total masses would be detected at a threshold SNR of 8. Fig. 11 shows the redshift of the horizon as a function of source-frame total mass for the detector configurations under consideration.

While horizon distances provide a sense of the farthest possible detections, the effects of cosmology and the non-spherical nature of detector response patterns make it difficult to intuit the corresponding changes to the detection rate. For this reason we provide estimates of the range, R, obtained as $(4\pi/3)R^3 = V$, where V is the orientation-averaged spacetime (comoving) volume surveyed per unit detector time. For a population of sources with a constant comoving source-frame rate density, multiplying V by that rate density provides the expected detection rate. Table 4 shows the range for fiducial BNS ($1.4{+}1.4\,M_\odot$) and BBH ($30{+}30\,M_\odot$) systems, as well as the maximum redshift at which an equal-mass non-spinning binary of *any* total mass could be observed.

As the sensitivity and bandwidth of the detectors improve, BNS signals will be observable early enough in their inspiral to enable approximate localization *before* merger. This could allow electromagnetic observatories to already be observing the localization region when the source becomes EM bright. Table 4 shows how many minutes prior to merger a $1.4{+}1.4\,M_\odot$ at $z = 0.03$ would accumulate enough SNR to pass a detection threshold of 8 for each configuration.

7.2 Catalog Size

O3 population analyses constrained the astrophysical rates of BNS, NSBH, and BBH mergers to $170.0^{+270.0}_{-120.0}$, $130.0^{+112.0}_{-69.0}$, and $25.0^{+10.0}_{-7.0}$ $\mathrm{Gpc}^{-3}\mathrm{yr}^{-1}$, respectively, with NSBH rates from [29] and BNS and BBH rates from [28] (median and central 90 % bounds). By assuming an astrophysical distribution and detector duty cycle we can predict the number of binaries of each class that will be detected with a given detector configuration. Similar to what is done in [30], we simulate a simple astrophysical distribution: BBHs are assumed to be equal mass with component masses following a power law with index -3, neutron stars have mass

	Range [Mpc]				Post-Merger	
Configuration	BNS	BBH	$t_{\rm early}$[min]	$z_{\rm max}$	$\rho_{\rm pm}^{(10)}$	$\rho_{\rm pm}^{(\rm max)}$
O3 LLO	130	1200	0.3	1.3	0.4	0.6
July 2022 LLO	120	1200	0.5	1.5	0.3	0.5
A+	350	2600	2.7	3.2	1.4	2.0
A+ Wideband	290	2300	3.7	3.5	2.2	2.6
A$^\sharp$	600	3700	6.2	5.4	2.7	3.7
A$^\sharp$ (A+ coatings)	440	3000	6.1	4.6	2.7	3.4
A$^\sharp$ Wideband	490	3300	6.8	5.5	4.8	5.6
A$^\sharp$ Wideband (A+ coatings)	400	2900	6.7	4.7	4.8	5.5
Intermediate Voyager	670	3900	4.8	6.5	2.5	3.7
Voyager Deep	780	4100	9.0	7.9	2.8	4.1
Voyager Wideband	630	3800	9.3	8.4	5.2	5.9
STO	690	4000	10.1	7.6	2.7	3.7
A$^\sharp$ 655 m SEC	450	3100	6.7	5.3	3.4	5.1
A$^\sharp$ 12 km folded arms	530	3400	9.9	6.4	8.5	9.7

Table 4: Astrophysical performance of the scenarios shown in Fig. 1 for optimally oriented non-spinning binary systems. The BNS and BBH range estimates are for 1.4+1.4 $M_\odot$ and 30+30 $M_\odot$ systems, respectively. The early warning time $t_{\rm early}$ is the time before merger of a 1.4+1.4 $M_\odot$ system at $z = 0.03$ at which the cumulative SNR in a given detector reaches 8; $t_{\rm early}$ is heavily dependent on the low frequency noise (as illustrated by $t_{\rm early}$ for the July 2022 LLO case, at 28 s, compared to O3, at 16 s, even though the latter has a bit higher BNS range), and the GWINC design curves do not include excess technical noise which has historically been present. $z_{\rm max}$ is the maximum redshift at which an equal mass binary can be detected (see Fig. 11); and the post-merger SNR $\rho_{\rm pm}$ is the SNR of the post-merger signal of an optimally oriented BNS at a distance of 100 Mpc. Three viable neutron star equations of state (SLy, ALF2, and LS220) are used to generate 302 sources; the SNR of the best 10 % of sources is $\rho_{\rm pm}^{(10)}$ and the SNR of the best source is $\rho_{\rm pm}^{(\rm max)}$.

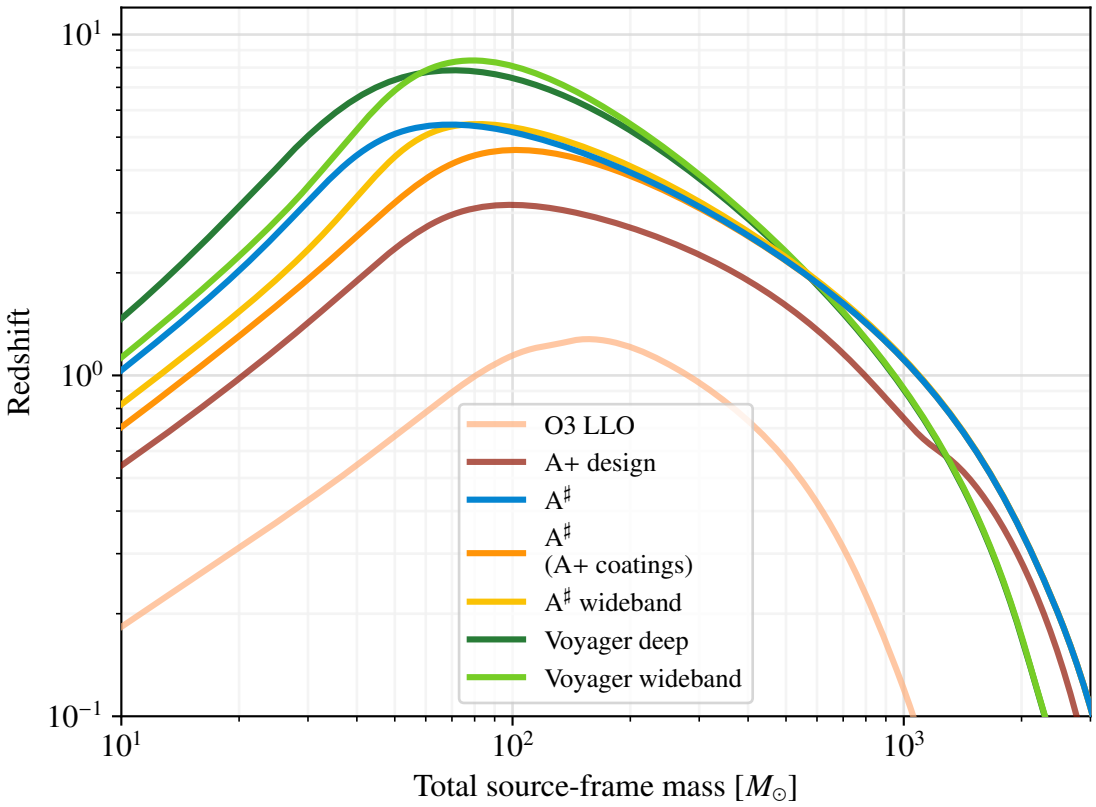

Figure 11: Horizon redshifts at which the SNR in a detector is 8 for optimally oriented, non-spinning, equal mass binaries for the scenarios shown in Fig. 1.

1.4 $M_\odot$, merger rates evolve proportionally to the star formation rate following [31]. For all scenarios we consider a LIGO-Hanford, LIGO-Livingston network with single-observatory duty cycles of 80 % and a network SNR threshold of 9 for BBH signals, and 8 for BNS and NSBH signals.

Table 5 shows the expected number of events each year of each class based on the current median and central 90 % credible intervals on their astrophysical rates. With catalogs of this size we should expect to perform *detailed* analyses of the astrophysical population, tracing out mass distributions, spin distributions, etc. with exceptional fidelity.

With catalogs of several 10^3 BBHs, we should expect to constrain $H(z)$ at the few percent level by measuring the redshift-luminosity-distance relation of BBHs if a mass scale is imprinted on the mass distribution (e.g., via the pair instability supernova process). While multi-messenger and/or dark siren constraints may allow us to surpass this precision, their expected constraints depend sensitively on the precision of localization of sources and completeness of galaxy catalogs, both of which are difficult to predict at this time.

Configuration	Annual Detections		
	BNS	NSBH	BBH
A+	69^{+138}_{-48}	291^{+291}_{-148}	1440^{+572}_{-412}
A$^\sharp$	364^{+717}_{-244}	1526^{+1517}_{-762}	6131^{+2132}_{-1739}
A$^\sharp$ (A+ coatings)	138^{+274}_{-94}	630^{+627}_{-317}	2902^{+1149}_{-826}
A$^\sharp$ Wideband	177^{+350}_{-120}	909^{+905}_{-455}	3937^{+1557}_{-1118}
Voyager Deep	794^{+1563}_{-529}	3798^{+3771}_{-1894}	11975^{+2932}_{-3392}
Voyager Wideband	404^{+798}_{-270}	2035^{+2021}_{-1016}	7343^{+2901}_{-2082}

Table 5: Plausible range of number of detections in a calendar year observing run for each class of binary. Ranges are based on the central 90 % credible intervals on astrophysical rates from O3 [28, 29].

7.3 Higher-Order Modes

The (complex) GW strain can be decomposed into a basis of spin-weighted spherical harmonics with spin weight -2

$$h = h_+ - ih_\times = \sum_{\ell \geq 2} \sum_{m=-\ell}^{\ell} h_{\ell m}\, {}^{-2}Y_{\ell m}, \tag{1}$$

where the $h_{\ell m}$ denote the higher-order multiples (modes) of the gravitational radiation field. While the quadrupolar ($\ell = 2$) modes are the most dominant, depending on the mass and spin parameters of the black holes as well as the orientation of the binary relative to the detector, higher-order modes can have a significant impact on the GW signal. Identifying individual higher order modes either during the inspiral or the ringdown of the remnant black hole enables precision tests of the black hole dynamics and the no-hair theorem [32].

We consider the HLV three-detector network with five different sensitivities of the two LIGO detectors and a fixed O5 target sensitivity for Virgo [33]. Following the O3 population analysis [28] and using GWPopulation [34], we draw 200 000 black hole binaries from the power law + peak mass model; for the black hole spins we consider the Default model, where the spin magnitudes follow a Beta distribution, while the spin orientations are drawn from a mixture model consisting of an aligned and isotropic component [35]. The binaries are distributed in redshift z according to a power law with a power law index of 2.7 following the star formation rate [31]. All extrinsic binary parameters are drawn from their standard prior distributions [36].

Using the inspiral-merger-rindown model `IMRPhenomXPHM` [37–39] we compute the optimal network SNR ρ_N for each binary. Imposing $\rho_N > 12$ for the complete signal, we determine the fraction of binaries detectable in the least sensitive network (A+). The SNR contained in the higher-order modes $(\ell, |m|) = (2,1), (3,3), (4,4)$ for the common set of detected binaries is shown in Fig. 12. We find comparable performance between the A+, A$^\sharp$ (A+ coatings) and A$^\sharp$ Wideband sensitivities, while A$^\sharp$ as well as the two Voyager sensitivities will provide a significant enhancement to detecting higher-order modes with an SNR above 6. For a given SNR there is at least a factor of a few improvement in the fraction of events with detectable higher-order modes between the A+ or A$^\sharp$ configurations with A+ coatings, and the A$^\sharp$ respectively Voyager designs. Sizeable higher-order modes improve the measurement

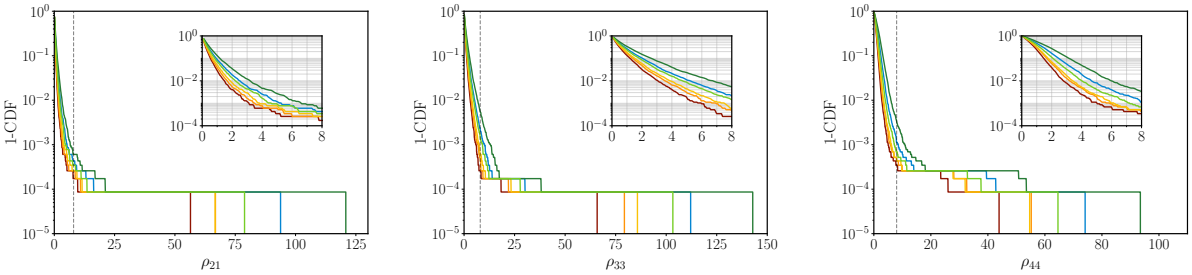

Figure 12: Expected distribution of SNR in the higher-order modes $(\ell, |m|) = (2,1), (3,3), (4,4)$ for BBH events drawn from the underlying astrophysical population with a network SNR $\rho_N > 12$ for six different LIGO sensitivities: A+ (red), A$^\sharp$ (A+ coatings) (orange), A$^\sharp$ (blue), A$^\sharp$ Wideband (golden), Voyager Wideband (light green) and Voyager Deep (dark green). The inset shows a zoom-in of the region where $\rho_{\ell m} \leq 8$. The vertical dashed line indicates an SNR of 6.

accuracy of the binary's source parameters by breaking certain degeneracies, e.g. the well-known distance-inclination as well as the mass ratio-spin degeneracy, and aid the detection of the gravitational-wave memory effect [40–42].

7.4 BNS Post-Merger Signals

We use the time-domain BNS post-merger waveforms for the SLy, ALF2, and LS220 equations of state from the CoRe database [43] to quantify the prospects of studying post-merger physics. The post-merger signal is defined as the part of the waveform after the ringdown has damped to a minimum, and the post-merger SNR $\rho_{\rm pm}$ given in Table 4 is the SNR of the post-merger signal.

7.5 Equation of State

Gravitational waves from BNSs provide a unique opportunity to probe the nuclear equation of state of cold ultradense matter through the tidal interaction between the two stars and the characteristic imprint it leaves in the GW signal. The GW signal emitted by a BNS differs from that of a BBH predominantly due to the star's deformation in its companion's gravitational field. At leading post-Newtonian order this induced tidal deformation is encapsulated by the (dimensionless) binary tidal deformability parameter $\tilde{\Lambda}$ [44].

We simulate a nonspinning GW170817-like BNS at a luminosity distance of 100 Mpc with the soft equation-of-state (EOS) APR4 [45] in the HLV three-detector network with four different sensitivities of the two LIGO detectors and a fixed O5 target sensitivity for Virgo [33]. Performing full Bayesian inference with Bilby [46, 47], assuming a maximal dimensionless neutron star spin of 0.05 and using the tidal waveform model `IMRPhenomD_NRTidalv2` [48, 49], we determine the posterior probability densities of the binary parameters. The result for $\tilde{\Lambda}$ is shown in Fig. 13. In particular, we find that the measurement accuracy, e.g. characterised by the 90 % credible interval, improved by almost a factor of two between the A+ and all of the post-O5 sensitivities.

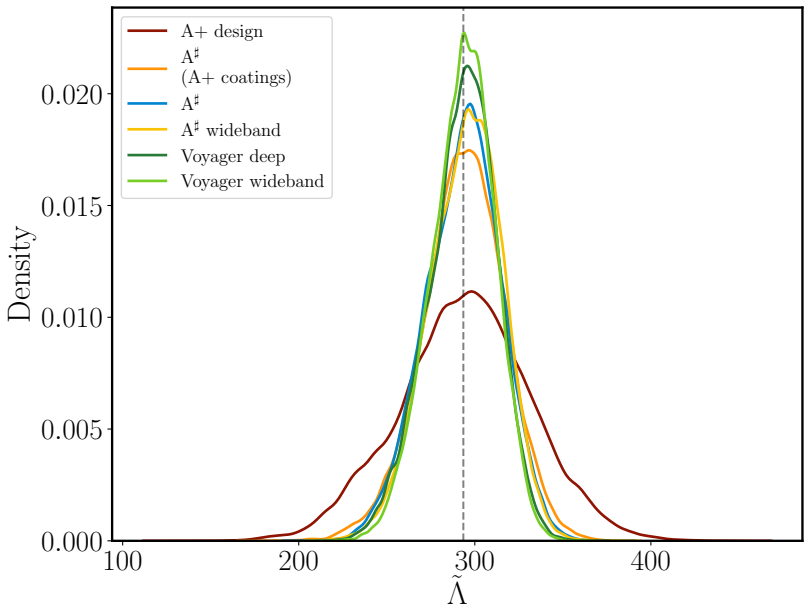

Figure 13: One-dimensional posterior probability density of the binary tidal deformability $\tilde{\Lambda}$ for a simulated GW170817-like BNS event at a distance of 100 Mpc for different LIGO sensitivities. The dashed vertical line indicates the parameter of the simulated signal.

Using quasi-universal relations [50], we map the tidal deformability parameter $\tilde{\Lambda}$ into a constraint on the neutron radius R via the compactness C and compare it against the predictions from other EOS. Fig. 14 shows our results for the five different sensitivities. As opposed to $\tilde{\Lambda}$ we find only very little improvement between A+ and the post-O5 sensitivities. It is interesting to note that we find almost identical results between Voyager Deep, Voyager Wideband and A♯ Wideband (A+ coatings). Since tidal effects come into view at GW frequencies $\gtrsim 400$ Hz, the improved sensitivity at $f \gtrsim 1000$ Hz for A♯ Wideband and Voyager Wideband may trade-off the better performance of Voyager Deep at frequencies below 800 Hz.

7.6 Gravitational Wave Background from Binary Mergers

In addition to detecting the coherent signal from relatively nearby binaries, we also expect to be sensitive to the astrophysical gravitational wave background of unresolved binaries. We use the inferred astrophysical merger rates of BNS, NSBH, and BBH systems from GWTC-3 to estimate the dimensionless energy-density spectra $\Omega_{\rm GW}(f)$ of gravitational waves radiated by each class of compact binary (see [28] for more details). Figure 15 shows current estimates for the total energy-density spectra from all compact binaries, compared with projected sensitivities of the various detector configurations. Any of the proposed upgrades to the A+ design will guarantee detection of the stochastic background from binary mergers, if it has not already been detected by the end of O5.

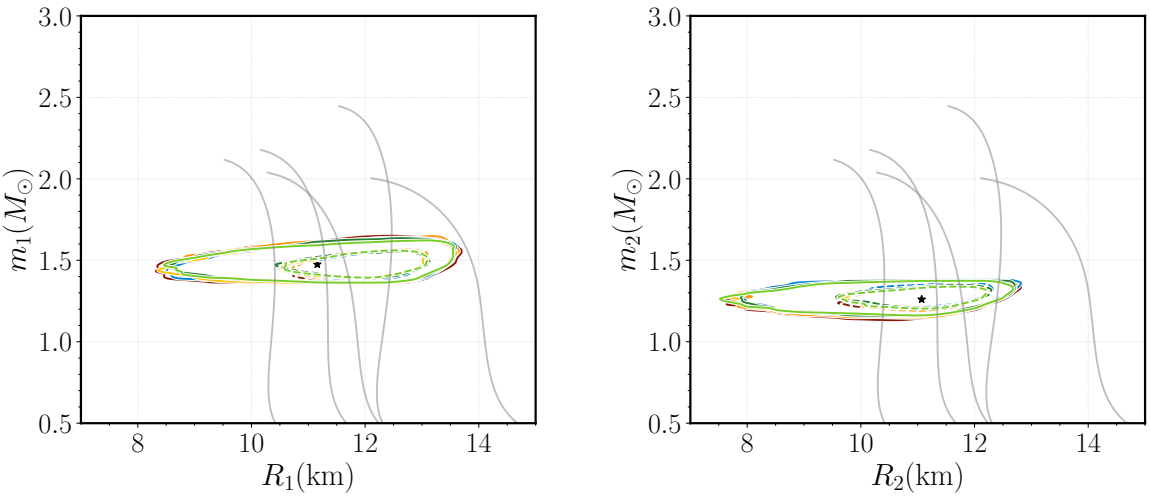

Figure 14: Mass-radius curves for a simulated GW170817-like BNS at a distance of 100 Mpc. We use universal relations to map from the tidal parameters to the neutron star radius R. Note that we do not enforce that both stars obey the same EOS. The LIGO sensitivities are A+ (red), A$^\sharp$ (A+ coatings) (orange), A$^\sharp$ (blue), A$^\sharp$ Wideband (golden), Voyager Wideband (light green) and Voyager Deep (dark green). The grey curves indicate predictions for a set of EOS, the star marks the parameters of the simulated signal.

7.7 Continuous Waves

Spinning deformed neutron stars (NSs) emit continuous gravitational waves (CWs) with typical time scales that are longer or comparable to the run duration, in contrast to transient GWs [51]. No CWs have been detected so far, although interesting upper limits have been obtained in various searches [52], including those for CW emission from known pulsars [53, 54], directed searches toward the Galactic center [55], specific supernova remnants [56] and LMXB systems, like Sco-X1 [57], and all-sky searches [58].

The typical amplitude of CW signals is difficult to estimate, as it depends on poorly known quantities, especially the star's ellipticity, which is a measure of its degree of asymmetry. For a non-accreting non-axisymmetric spinning NS the signal amplitude is given by

$$h_0 = \frac{4\pi^2 G}{c^4}\frac{\epsilon I_{zz} f^2}{d} \approx 10^{-26}\left(\frac{\epsilon}{10^{-6}}\right) \times \left(\frac{I_{zz}}{10^{38}\,\mathrm{kg\,m^2}}\right)\left(\frac{f}{100\,\mathrm{Hz}}\right)^2\left(\frac{1\,\mathrm{kpc}}{d}\right), \qquad (2)$$

where d is the source distance, f is the GW frequency (twice the spin frequency for a NS rotating around one of its principal axes of inertia), $\epsilon = (I_{xx} - I_{yy})/I_{zz}$ is the ellipticity of the star, and I_{zz} is its moment of inertia with respect to the principal axis (z-axis) aligned with the rotation axis.

Although the range of CW searches is very wide, and covers also exotic sources, such as ultra-light dark matter particles, see e.g. [59], in the following we provide some figures of merit about detection perspectives in the post-O5 era focusing on two specific – but important – cases: targeted searches for known pulsars and all-sky searches for isolated NSs. The former are based on fully coherent matched filtering, which provides optimal sensitivity (under the

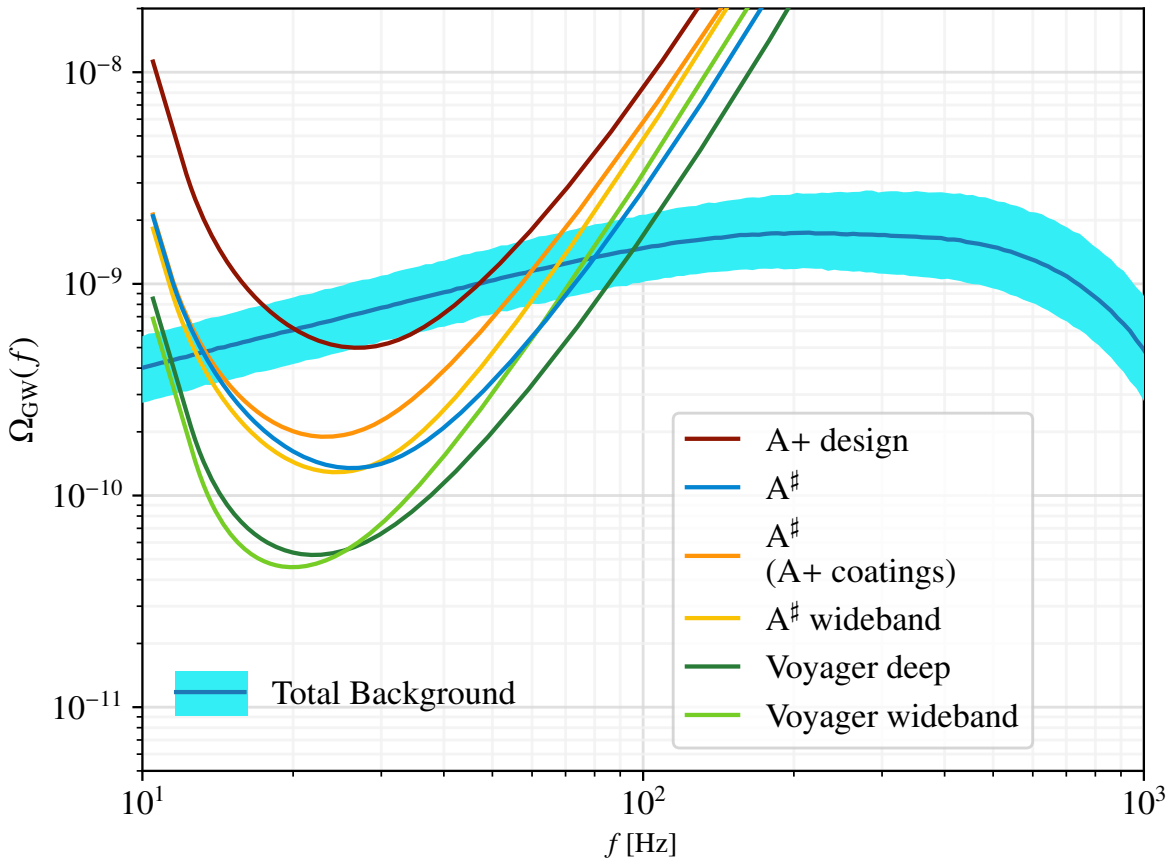

Figure 15: Forecast for the astrophysical gravitational wave background from binary mergers based on observations through O3. The (blue) band shows current estimates for the total dimensionless energy-density spectra across BNS, NSBH, and BBH sources, compared with the projected sensitivities of the various detector configurations. While the A+ design should enable detection of this background, *any* of the post-O5 designs should guarantee detection of the astrophysical background.

assumption of Gaussian noise) but requires a very accurate knowledge of the source's main parameters, typically provided by electromagnetic observations. The latter – at the other extreme – search a wide parameter space for sources with no electromagnetic counterpart, having to use computationally cheaper and less sensitive methods.

For targeted searches we provide summary results in Table 6. This lists, for different detector configurations, the number of potentially detectable known pulsars (at 95 % C.L.) under three different assumptions on their ellipticity, considering a fully-coherent search based on matched filtering in the frequency domain [60], a total observation time $T_{\rm obs} = 3\,$years[17], and a duty cycle of 80 %.

Column 2 corresponds to assuming that pulsars emit at their spin-down limit, i.e. that all their loss of rotational energy is due to GW emission, yielding an ellipticity $\epsilon_{\rm sd}$, depending on moment of inertia, spin frequency and frequency derivative. Column 3 assumes every pulsar's

[17]For fully coherent analyses, this is equivalent to a network of three detectors with equal sensitivity over one year.

Configuration	n_1 $\left(\frac{\epsilon_{\rm min}}{10^{-10}},\ \frac{\epsilon_{\rm median}}{10^{-5}}\right)$	n_2 $\left(\frac{\epsilon_{\rm min}}{10^{-10}},\ \frac{\epsilon_{\rm median}}{10^{-9}}\right)$	n_3 $\left(\frac{\epsilon_{\rm min}}{10^{-10}},\ \frac{\epsilon_{\rm median}}{10^{-10}}\right)$
A+	148 (8.8, 6.0)	37 (8.8, 8.0)	4 (8.8, 10)
A$^\sharp$	219 (4.9, 2.4)	80 (4.9, 5.6)	7 (4.9, 7.3)
A$^\sharp$ (A+ coatings)	194 (5.4, 4.4)	54 (5.4, 6.1)	4 (5.4, 6.5)
A$^\sharp$ Wideband	191 (5.8, 4.0)	51 (5.8, 8.2)	4 (5.8, 7.4)
Voyager Deep	248 (4.3, 1.1)	107 (4.3, 7.3)	8 (4.3, 6.8)
Voyager Wideband	207 (4.9, 1.8)	66 (4.9, 6.8)	4 (4.9, 6.2)

Table 6: Expected number of detectable known pulsars, assuming three different conditions for the ellipticity: $\epsilon = \epsilon_{\rm sd}$ (case n_1), $\epsilon = \min(\epsilon_{\rm sd},\ 10^{-6})$ (case n_2), $\epsilon = \min(\epsilon_{\rm sd},\ 10^{-9})$ (case n_3), a total observation time $T_{\rm obs} = 3$ years and a duty cycle of 80%. For each case, we give in parentheses the minimum and median ellipticity for detectable signals.

ellipticity is the minimum of $\epsilon_{\rm sd}$ and 10^{-6}, which is of the order of the maximum theoretical ellipticity a NS with standard EOS is expected to have, see e.g. [61]. Column 4 (n_3) considers the minimum of $\epsilon_{\rm sd}$ and 10^{-9}, considered as a plausible value for millisecond pulsars [62]. These results show a significant improvement in detection perspectives with respect to the current situation [53]. This is true, in particular, for the A$^\sharp$ (AlGaAs coatings) and Voyager deep configurations. Similar results would be obtained using other algorithms based on matched filtering.

Concerning all-sky searches, Fig. 16 shows, for different detector configurations, the minimum detectable ellipticity as a function of signal frequency, assuming the source's rotational evolution is dominated by GW emission and a fixed source distance of 5 kpc. These results have been obtained considering an analysis done by means of the FrequencyHough pipeline [63], a semi-coherent procedure routinely used in current CW searches. Its sensitivity can be estimated (assuming Gaussian noise) as

$$h_{\rm min,95\%} \approx \frac{4.97}{N^{1/4}}\sqrt{\frac{S_n(f)}{T_{\rm FFT}}}\sqrt{CR_{\rm thr} + 1.6449}, \tag{3}$$

where $N = T_{\rm obs}/T_{\rm FFT}$ is the ratio of total observation time and the duration of the data segments to be incoherently combined, $S_n(f)$ is the average detector noise power spectrum and $CR_{\rm thr}$ is the threshold critical ratio to select signal candidates. In the plot we have used $T_{\rm obs} = 1$ year, $T_{\rm FFT} = 1$ day[18] and $CR_{\rm thr} = 4.5$.

For instance, a source located at 5 kpc emitting a signal at 500 Hz would be detected if its ellipticity is at least $\sim 10^{-7}$. At a given frequency, the ellipticity scales linearly with the distance. Nearby sources, e.g. located within ~ 500 pc, would produce detectable signals with an ellipticity as small as few times per 10^{-9}, if spinning at around 500 Hz. As before, although the results presented here are based on a specific analysis pipeline, we expect similar results using other semi-coherent methods.

[18] Although current searches typically use a shorter data segment duration, values as large as 1 day are very reasonable, and likely conservative, for the Post-O5 era, given the algorithmic developments and the increase in available computing power.

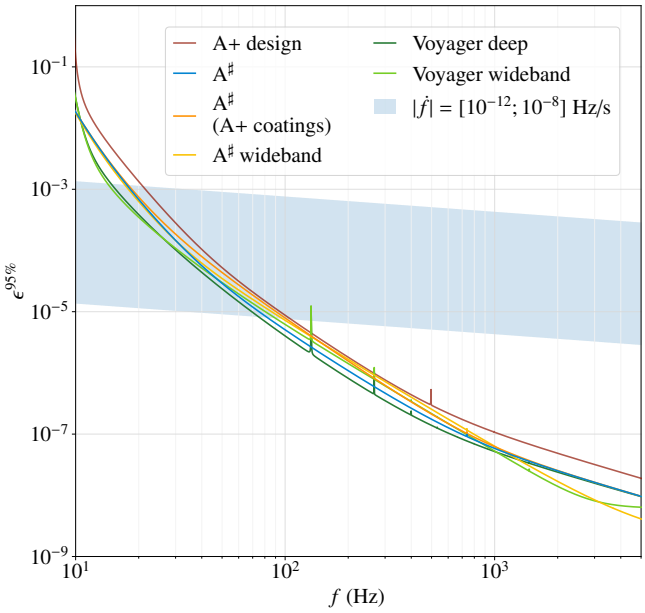

Figure 16: Sensitivity reach to all-sky searches of CWs (95 % C.L.). The various continuous curves are the minimum detectable ellipticity as a function of frequency for different detector configurations, assuming a source distance of 5 kpc, an observation time $T_{\mathrm{obs}} = 1$ year, a duty cycle $D = 80\,\%$ and data segments duration $T_{\mathrm{FFT}} = 1$ day. The shaded area is delimited by lines of constant spin-down of, respectively, 10^{-12} Hz/s and 10^{-8} Hz/s.

8 Relationship with other instruments

The A♯ configurations naturally have a large overlap with the A+ configuration; in addition most of the A♯ technology improvements and new technologies will serve as pathfinders for Cosmic Explorer. In addition, A♯ has a lot of technical overlap with AdVirgo+ and Virgo_nEXT, which offers the possibility of collaborating on developing these technologies.

Voyager has some technology overlap with some possible Einstein Telescope configurations.[19]

[19] cf. ETpathfinder Design Report: https://www.etpathfinder.eu/research/

A Detector parameters

Parameter	Units	A+	A$^\sharp$	iVoy	STO	VoyD	VoyW
Arm power	kW	750	1500	3000	1500	4000	4000
Laser wavelength	µm	1	1	2	1	2	2
Test mass material		Silica	Silica	Silicon	Silica	Silicon	Silicon
Temperature	K	295	295	123	295	123	123
Test Mass	kg	40	100	200	200	200	200
Total susp. mass	kg	120	400	520	520	520	520
Final stage susp. length	cm	60	60	80	80	80	80
Total susp. length	m	1.6	1.6	1.6	1.6	1.6	1.6
Observed squeezing	dB	7	10	9	10	9	9
Rayleigh wave suppression	dB	0	6	6	20	20	20
Test Mass Coatings		A+	AlGaAs	Ta/aSi/SiO_2	AlGaAs	aSi	aSi
Horiz. susp. pt. at 1 Hz	pm $/\sqrt{\text{Hz}}$	10	10	10	0.1	0.1	0.1
Final susp. stage blade		None	None	Aluminum	Silica	Silicon	Silicon
ETM beam radius	cm	6.2	5.5	8.0	5.5	8.4	8.4
ITM beam radius	cm	5.3	4.5	5.2	4.5	5.9	5.9
Cavity stability $g_i g_e$		0.83	0.71	0.62	0.71	0.73	0.73
Transverse mode spacing	kHz	32.5	30.7	29.6	30.7	31.0	31.0
Filter cavity linewidth	Hz	48	42	28	30	36	13
Arm finesse		450	450	3100	450	2000	2000
SRM transmission	%	32.5	32.5	4.6	32.5	9.2	1.1
Arm length	m	3995	3995	3995	3995	3995	3995
Filter cavity length	m	300	300	300	300	300	300
SEC length	m	55	55	55	55	55	55
RT arm cavity loss	ppm	75	75	20	75	20	20
RT filter cavity loss	ppm	40	30	10	20	10	10
RT SEC loss	ppm	3000	500	500	500	500	500
Exc. gas damp.		2.0	2.6	2.5	3.1	2.5	2.5
Diffusion time	µs	800	1500	1400	2300	1400	1400

Table 7: Defining parameters of detectors (aSi: amorphous silicon; AlGaAs: aluminum gallium arsenide; RT: round trip). The parameters needed to reach these squeezing levels are given in Table 2. Detailed coating parameters are given in Table 9. The excess gas damping is the squeezed film enhancement to residual gas damping as described in [64] and calculated in LIGO-T0900582. As described in Appendix A of [64], the details of the sticking time for molecules in the TM/ERM gap depend on the mirror temperature and the AR coating's sticking energy. These are not well characterized for our amorphous oxides at 123 K, and so while we expect the squeezed film damping to be less for Voyager, we use the standard room temperature formula as a conservative upper limit for now.

Parameter	Units	A+	A+ WB	A♯	A♯ WB	A♯ LS	A♯ 12 km	VoyD	VoyW
SRM trans	%	32.5	5.0	32.5	5.0	3.0	1.3	9.2	1.1
SEC detune	deg	0	0	0	0	0	0	0	0
FC detune	Hz	46	17	41	15	11	13	36	12
Arm length	km	4	4	4	4	4	12	4	4
SEC length	m	55	55	55	55	655	55	55	55
RT SEC loss	ppm	3000	3000	500	500	500	500	500	500
RT FC loss	ppm	40	40	30	30	30	30	10	10

Table 8: Parameters for the configurations shown in Figs. 7 and 8. WB: wideband; LS: Long SEC (655 m in the FC tube); SEC: signal extraction cavity; SRM: signal recycling mirror; FC: filter cavity.

Parameter	Units	A+	AlGaAs	aSi	Ta/aSi/SiO_2
High Index Layers					
Loss angle		9.0×10^{-5}	6.2×10^{-6}	1.0×10^{-5}	1.4×10^{-5}
Refractive index		2.09	2.09	3.50	3.50
Young's modulus	GPa	120	120	60	60
Poisson ratio		0.29	0.29	0.22	0.22
Thermal conductivity	W/m/K	33	33	1.03	1.03
Thermal expansion coeff.	ppm/K	3.6	3.6	1×10^{-3}	1×10^{-3}
Thermorefractive coeff.	ppm/K	14	14	140	140
Heat capacity per volume	J/K/m^3	2.1×10^{6}	2.1×10^{6}	1.1×10^{6}	1.1×10^{6}
Low Index Layers					
Loss angle		1.3×10^{-5}	6.2×10^{-6}	1.0×10^{-4}	1.4×10^{-4}
Refractive index		1.45	1.45	1.44	1.44
Young's modulus	GPa	70	70	72	72
Poisson ratio		0.19	0.19	0.17	0.17
Thermal conductivity	W/m/K	1.38	1.38	1.05	1.05
Thermal expansion coeff.	ppm/K	0.51	0.51	0.51	0.51
Thermorefractive coeff.	ppm/K	8	8	8	8
Heat capacity per volume	J/K/m^3	1.6×10^{6}	1.6×10^{6}	1.6×10^{6}	1.6×10^{6}

Table 9: Coating parameters used to calculate coating thermal noise. The coating names correspond to those listed in Table 7. The AlGaAs loss angles are reverse-engineered to produce the upper limit for AlGaAs coating thermal noise measured in LIGO-G2001592. As such, and since a coating design canceling thermo-optic noise does not yet exist for these coatings, the coating Brownian noise calculated with these loss angles is taken as the total coating thermal noise for the AlGaAs coatings in this report. Ta/aSi/SiO_2 refers to the non-binary coatings used by initial Voyager where tantala replaces amorphous silicon as the high index material in the top few coating layers to reduce absorption. This is modeled as a 20 % increase in coating thermal noise relative to the Voyager aSi/SiO_2 coatings in this report.

Species	Tube pressure [torr]	Chamber pressure [torr]
H_2	2.0×10^{-9}	2.0×10^{-9}
H_2O	1.0×10^{-10}	1.0×10^{-10}
N_2	1.0×10^{-10}	1.0×10^{-10}
O_2	7.5×10^{-12}	7.5×10^{-12}

Table 10: Partial pressures used to calculate residual gas noise.

B Technical Readiness Level (TRL) Definitions

For completeness we have included a description of the Technical Readiness Levels that have been copied from the following website: https://acqnotes.com/acqnote/tasks/technology-readiness-level

Level	Definition	TRL Description
1	Basic principles observed and reported.	Lowest level of technology readiness. Scientific research begins to be translated into applied research and development. Examples might include paper studies of a technology's basic properties.
2	Technology concept and/or application formulated.	Invention begins. Once basic principles are observed, practical applications can be invented. Applications are speculative and there may be no proof or detailed analysis to support the assumptions. Examples are limited to analytic studies.
3	Analytical and experimental critical function and/or characteristic proof of concept.	Active research and development is initiated. This includes analytical studies and laboratory studies to physically validate analytical predictions of separate elements of the technology. Examples include components that are not yet integrated or representative.
4	Component and/or breadboard validation in laboratory environment.	Basic technological components are integrated to establish that they will work together. This is relatively "low fidelity" compared to the eventual system. Examples include the integration of "ad hoc" hardware in the laboratory.
5	Component and/or breadboard validation in relevant environment.	The Fidelity of breadboard technology increases significantly. The basic technological components are integrated with reasonably realistic supporting elements so it can be tested in a simulated environment. Generally all scientific risk is considered retired beyond TRL 5.
6	System/subsystem model or prototype demonstration in a relevant environment.	A representative model or prototype system, which is well beyond that of TRL 5, is tested in a relevant environment. Represents a major step up in a technology's demonstrated readiness.
7	System prototype demonstration in an operational environment.	Prototype near, or at, planned operational system. Represents a major step up from TRL 6, requiring the demonstration of an actual system prototype in an operational environment such as an aircraft, vehicle, or space.
8	Actual system completed and qualified through test and demonstration.	Technology has been proven to work in its final form and under expected conditions. In almost all cases, this TRL represents the end of true system development. Examples include developmental test and evaluations of the system in its intended weapon system to determine if it meets design specifications.
9	Actual system has proven through successful mission operations.	The actual application of the technology in its final form and under mission conditions, such as those encountered in operational test and evaluation. Examples include using the system under operational mission conditions.

Table 11: Technical Readiness Levels (TRL) descriptions

C Extra Interferometers

Here we compare a few variants of the interferometers used for Fig. 1. Noise budget plots for each can be found in Appendix D.

- **Intermediate Voyager.** This is a version of Voyager that is meant to have a higher degree of technical readiness than the nominal design. The main differences are:
  1. smaller beam size on the ITM (enabling the use of smaller mirrors which are easier to acquire);
  2. test mass coatings that use silica/tantala for the top 1-2 bilayers (in case amorphous silicon absorption reduction does not succeed);
  3. aluminum blade springs at the bottom suspensions stage (in case silicon spring development takes longer).
- **STO, or Spacetime Observatory.** This is a more ambitious version of A$^\sharp$, with the test masses increased to 200 kg, AlGaAs/GaAs crystalline coatings on the test masses, fused silica blade springs included in the test mass suspension stage, a higher level of Newtonian noise suppression, and significantly reduced ISI platform motion. The idea is that STO is more comparable to Voyager in terms of technical readiness/feasibility.

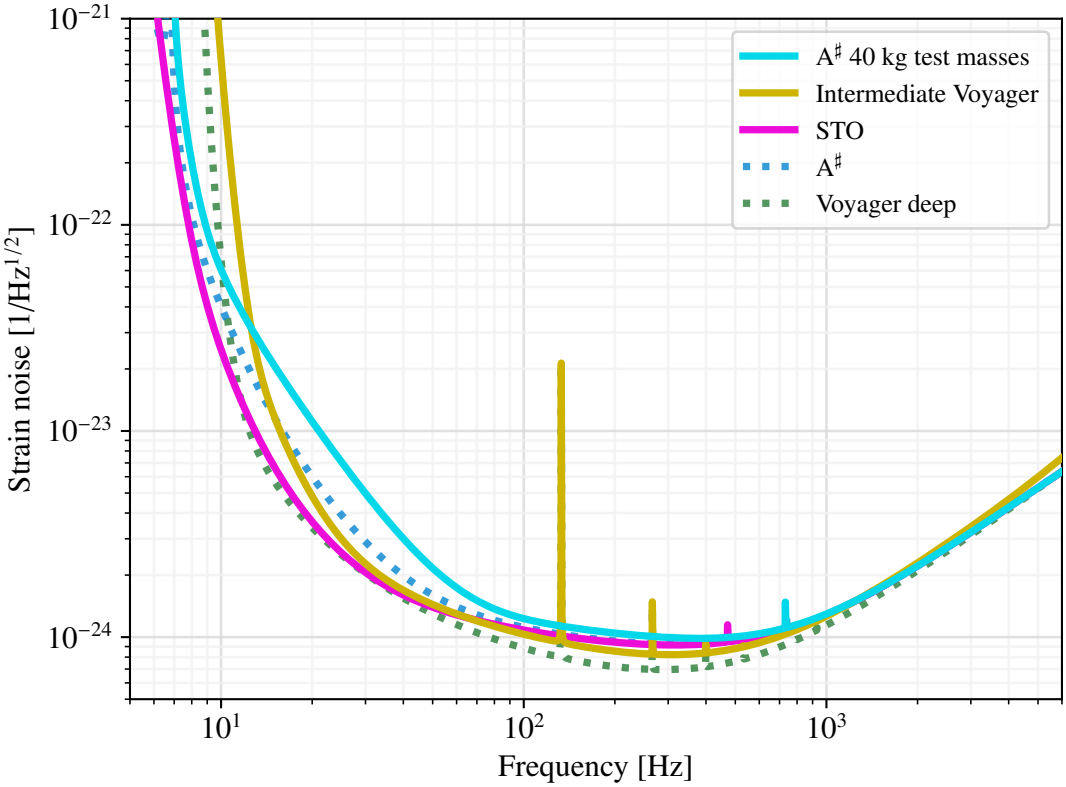

Figure 17: Design strain noise for variants of the designs shown in Fig. 1. 'A♯ 40 kg test masses' is the A♯ design, but without the heavier test masses (but with the higher stress suspension fibers). See text for the other curves.

D Noise Budgets

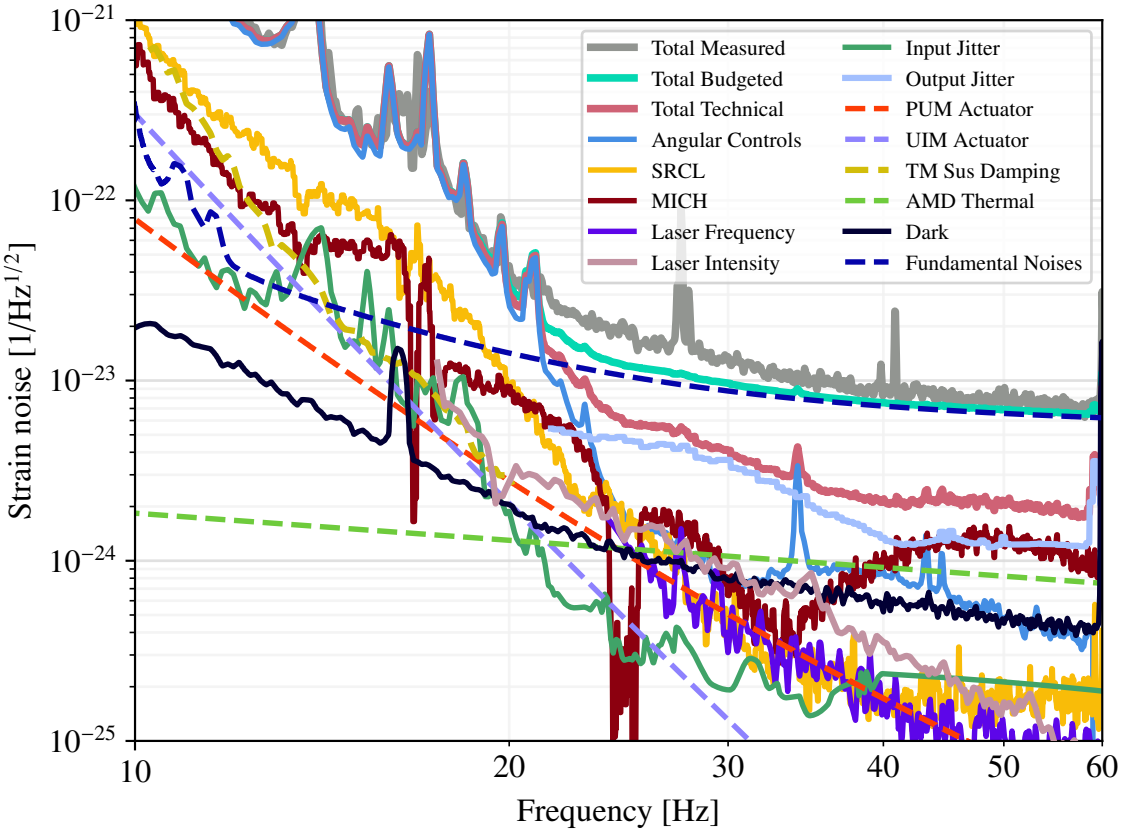

Figure 18: LIGO Livingston technical noise budget from July 2022. The aquamarine "Total Budgeted" curve is the sum of all the known noises (technical and fundamental). This is less than the gray "Total Measured" curve, which is the same as the pink curve of Fig. 4, showing that there are unknown noise sources in the 20–40 Hz band. MICH and SRCL are auxiliary length Michelson and signal recycling cavity length degrees of freedom, respectively. The control noises from the auxiliary degrees of freedom, especially the angular controls, are significant and should be reduced by the improved suspensions and seismic isolation and the larger test masses proposed for A♯ and discussed in Section 5.1. The dark blue dashed "Fundamental Noises" curve includes the quantum, suspension thermal, coating thermal, seismic, and residual gas noises. PUM: penultimate mass; UIM: upper intermediate mass; AMD: acoustic mode dampers; TM Sus: test mass suspensions.

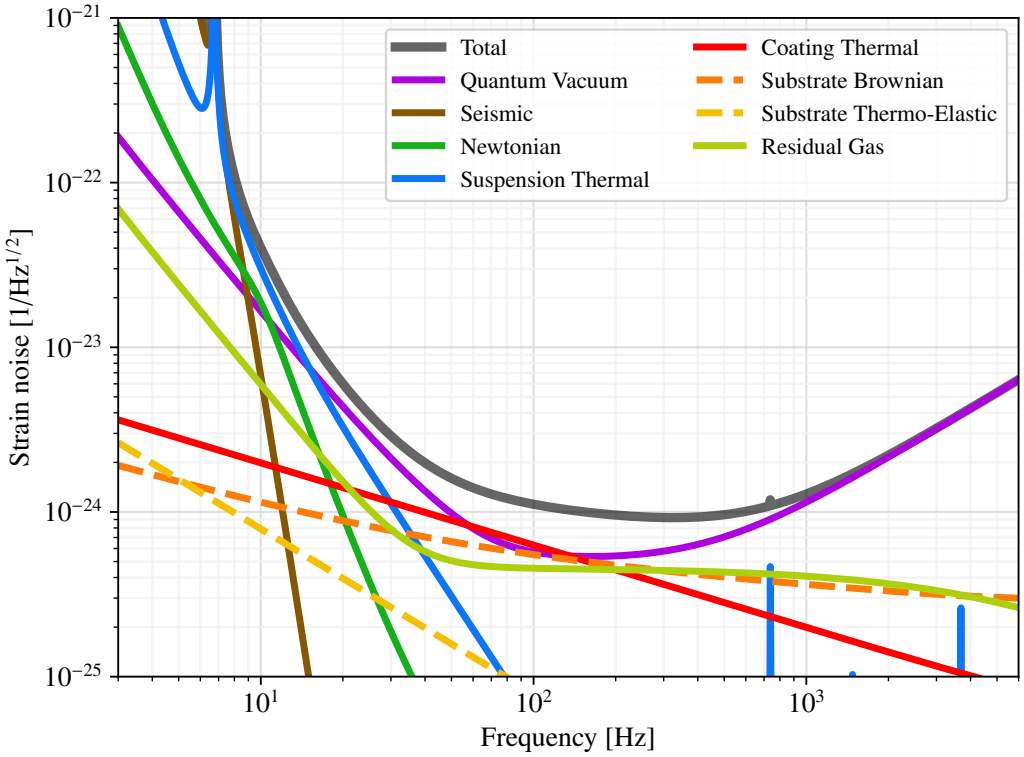

Figure 19: A♯ noise budget

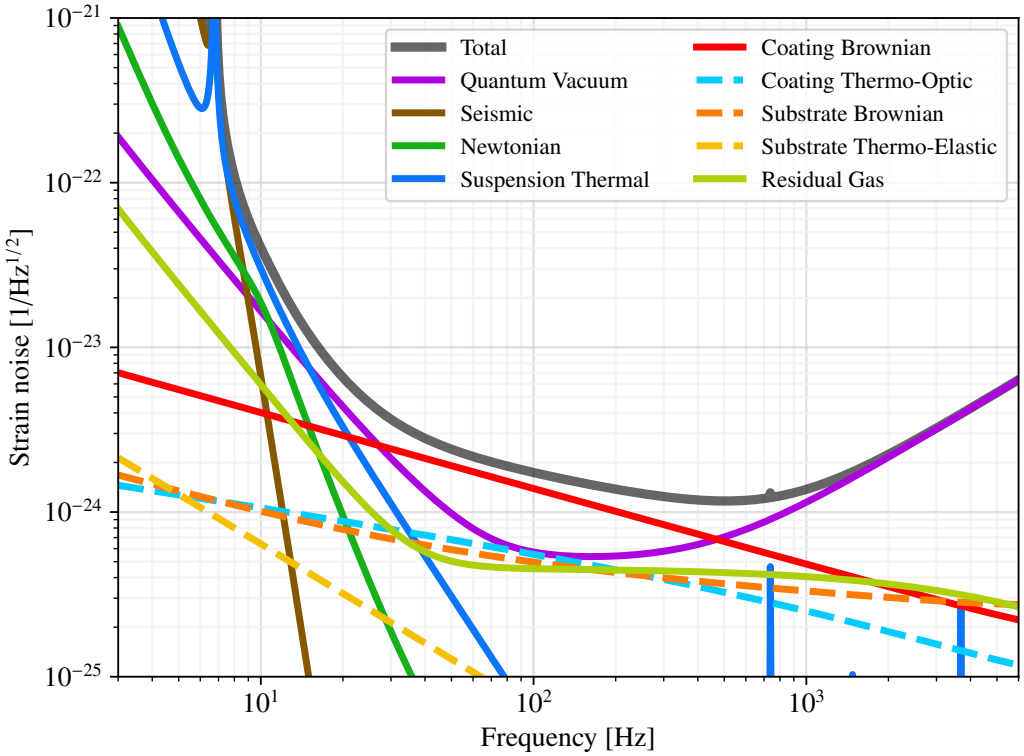

Figure 20: A♯ noise budget with A+ coatings

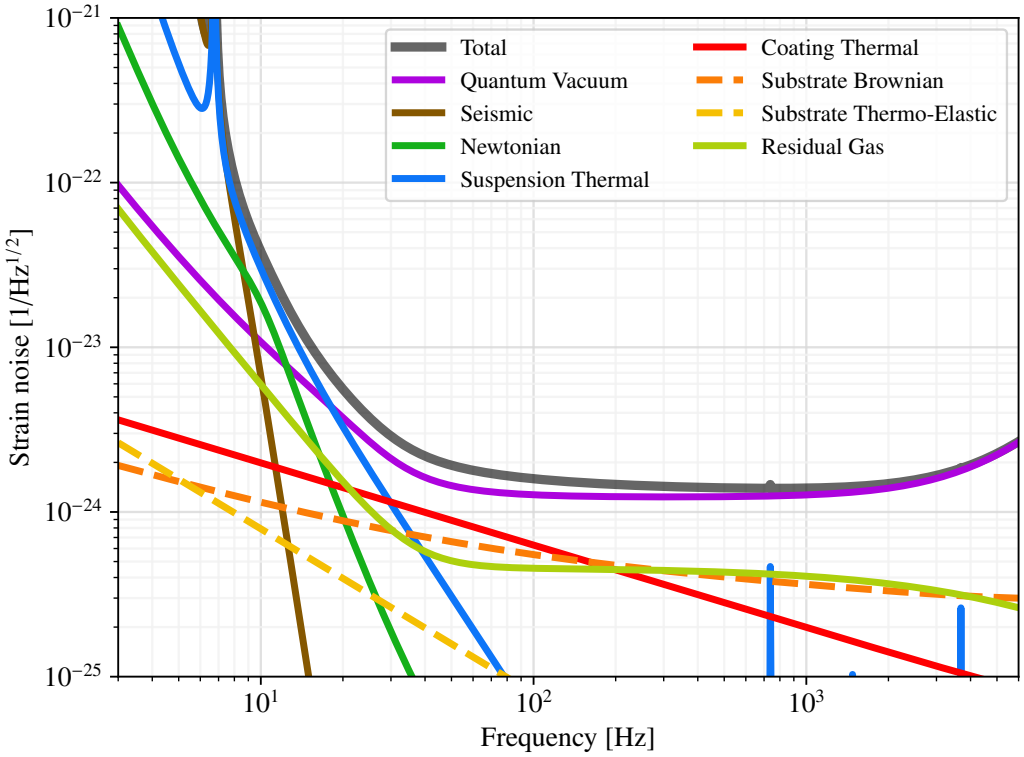

Figure 21: A$^\sharp$ wideband noise budget

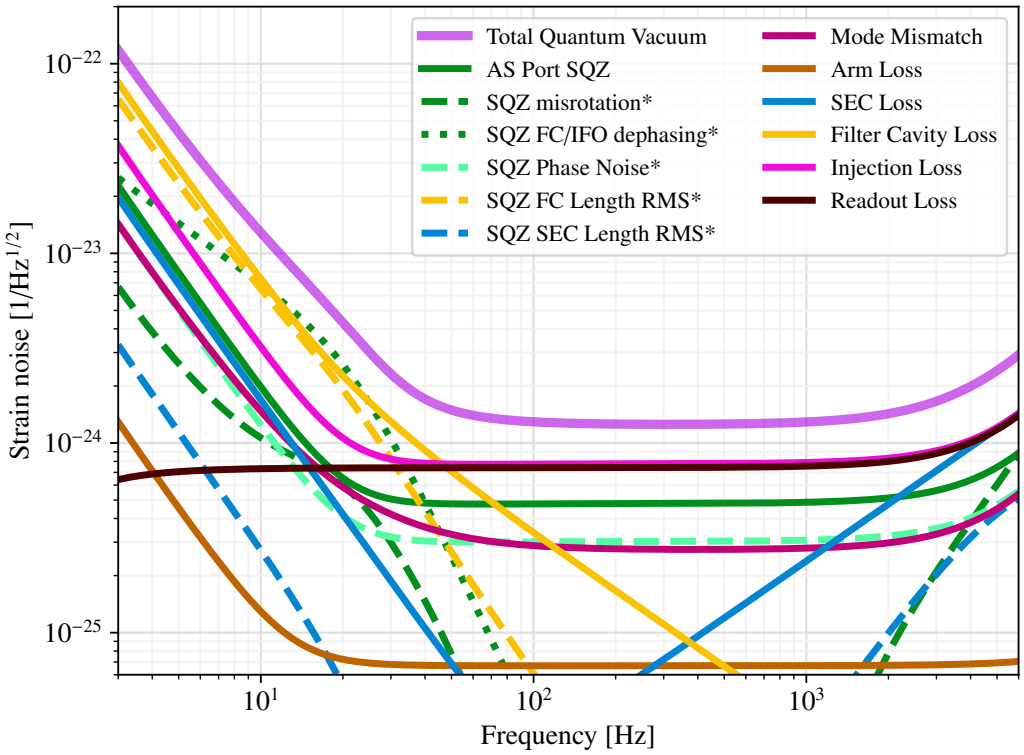

Figure 22: A$^\sharp$ wideband quantum noise budget

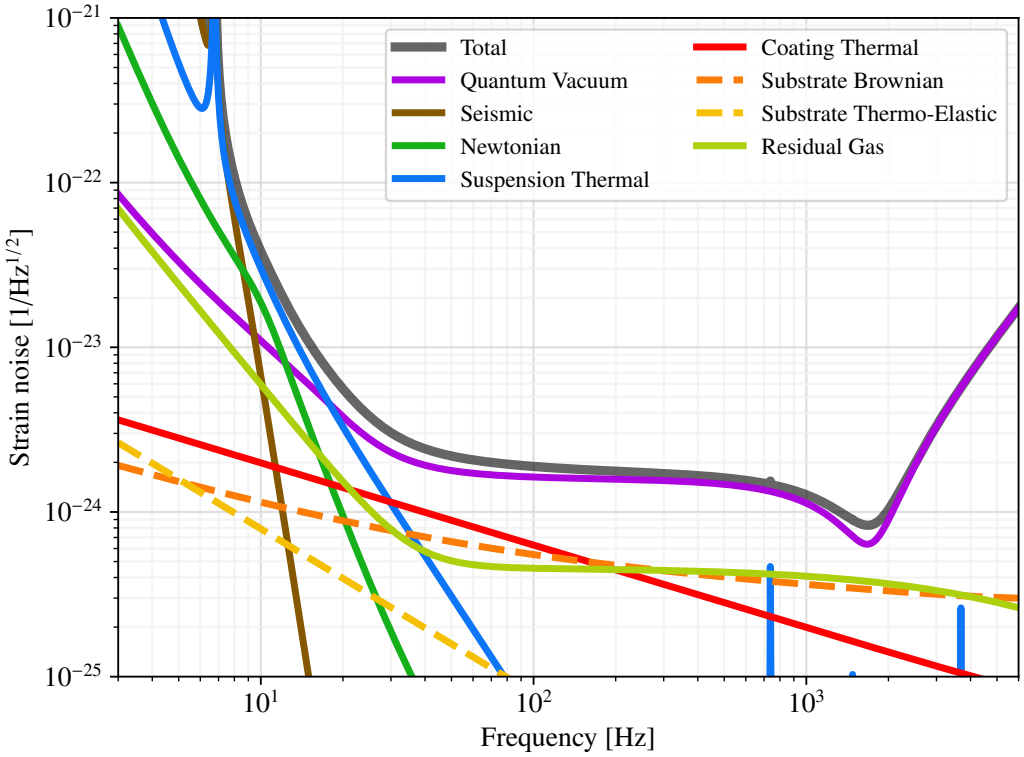

Figure 23: A♯ 655 m long SEC noise budget

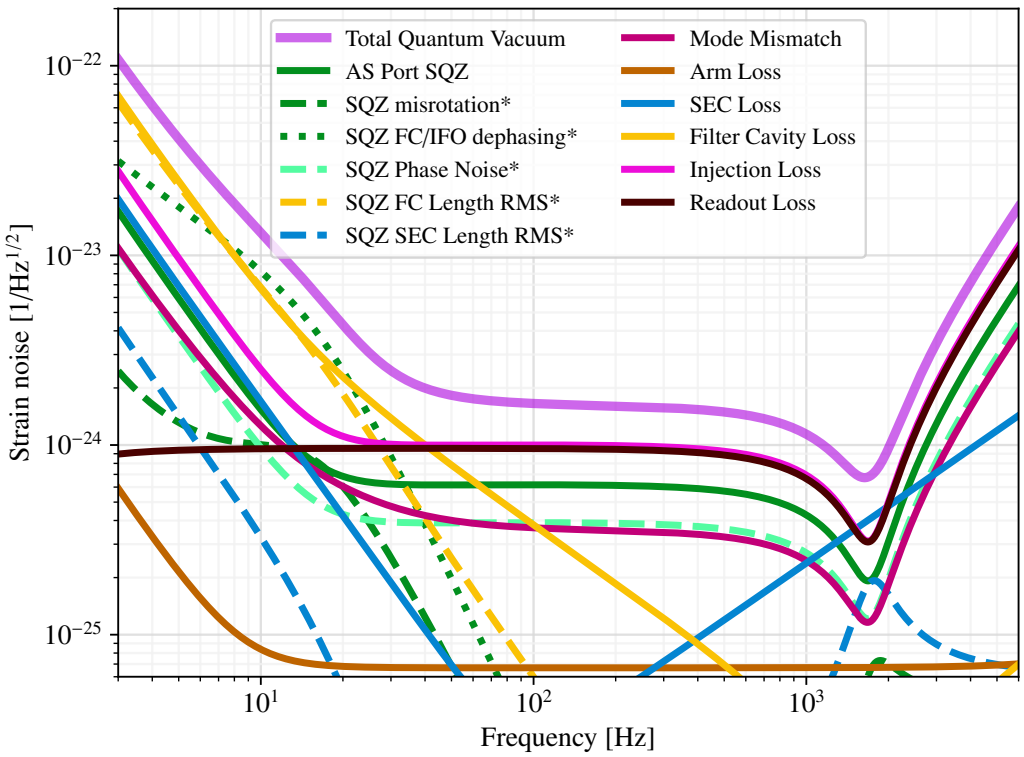

Figure 24: A♯ 655 m long SEC quantum noise budget

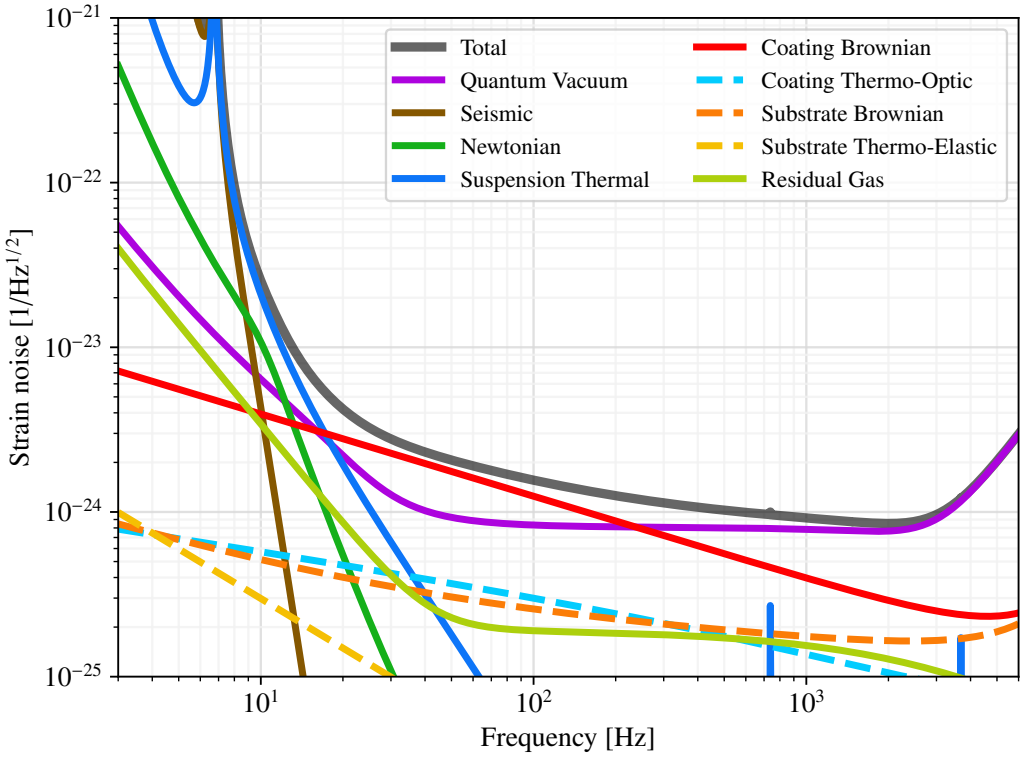

Figure 25: A$^\sharp$ noise budget with 12 km folded arms

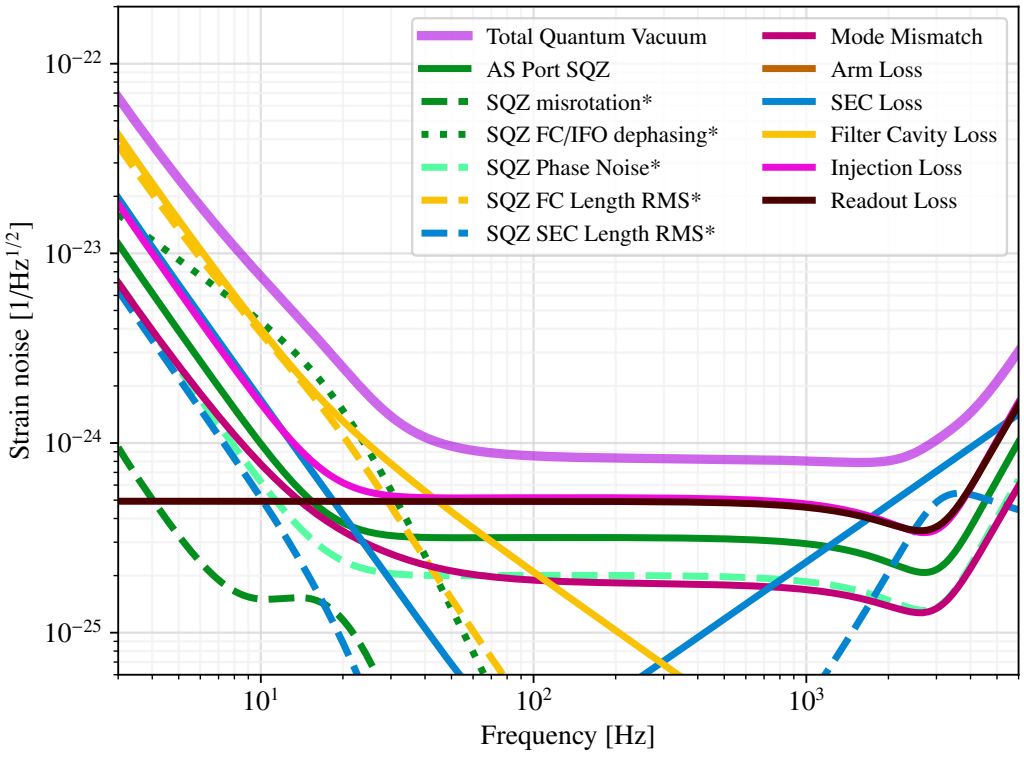

Figure 26: A$^\sharp$ quantum noise budget with 12 km folded arms

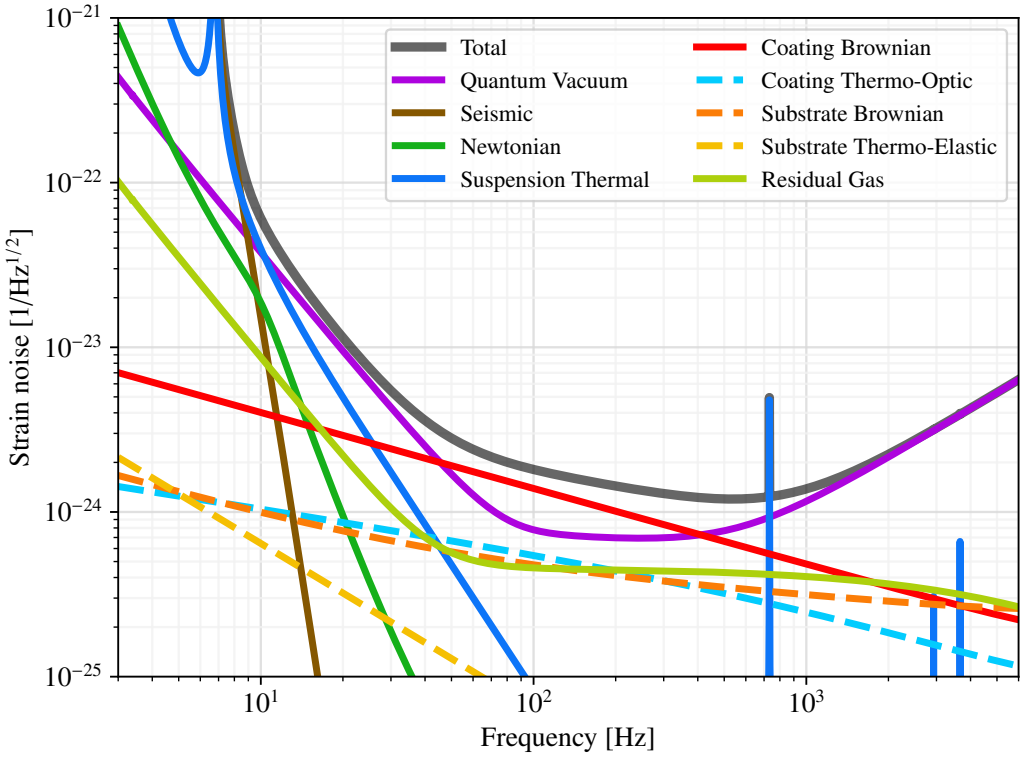

Figure 27: A$^\sharp$ noise budget with 40 kg test masses

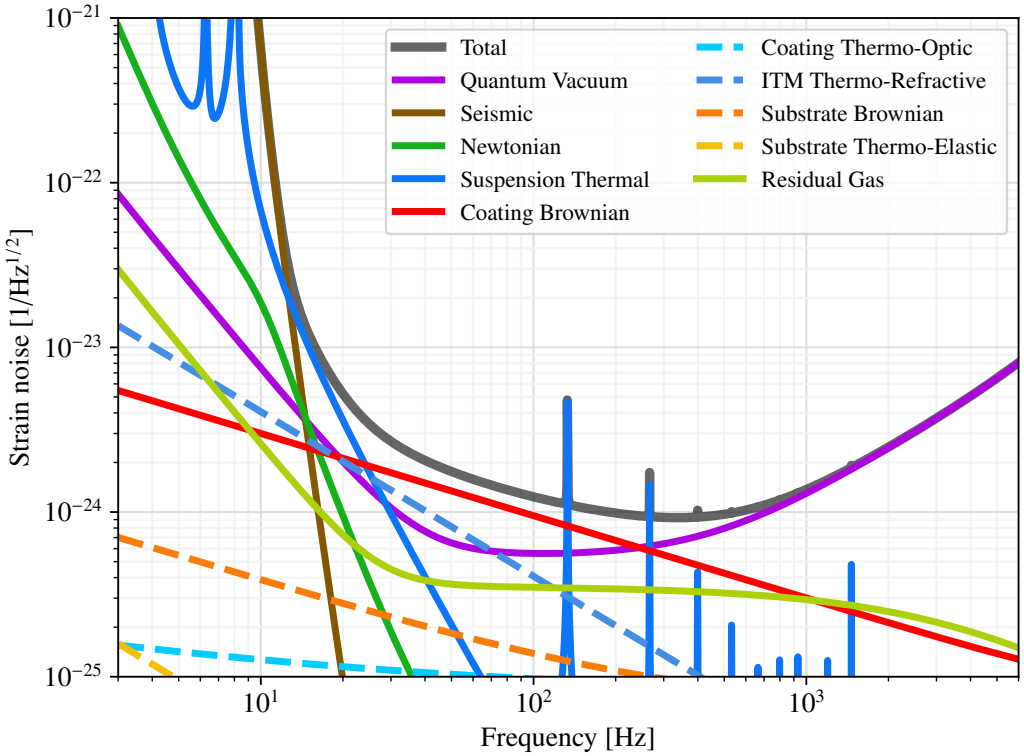

Figure 28: Intermediate Voyager noise budget

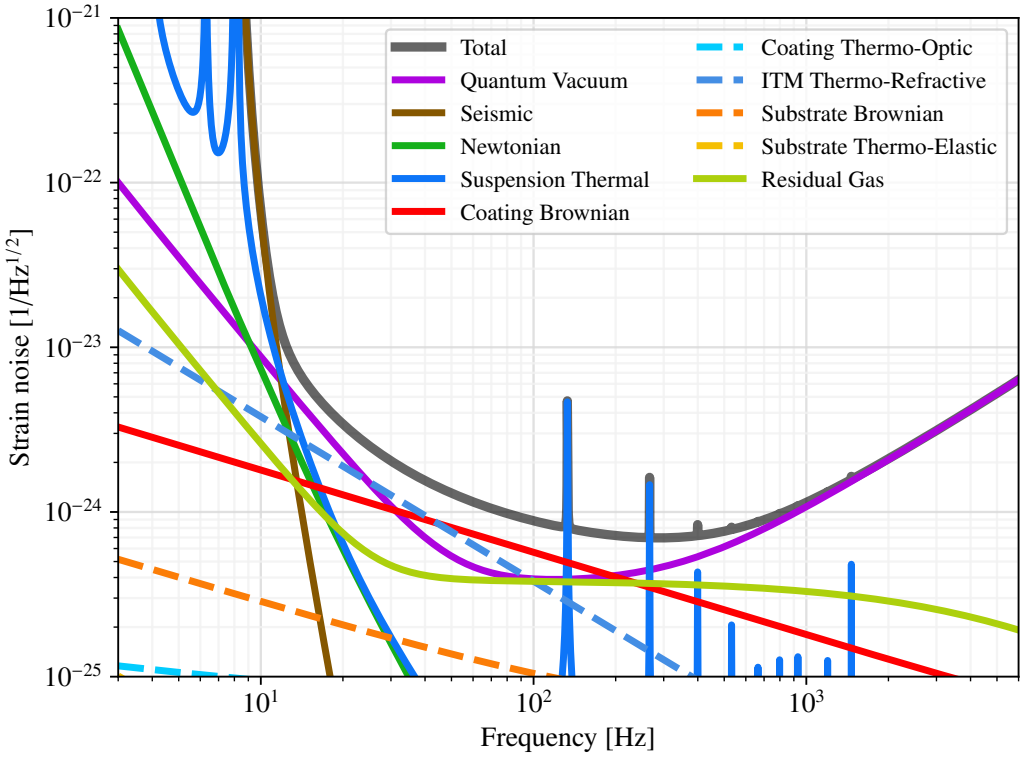

Figure 29: Voyager Deep noise budget

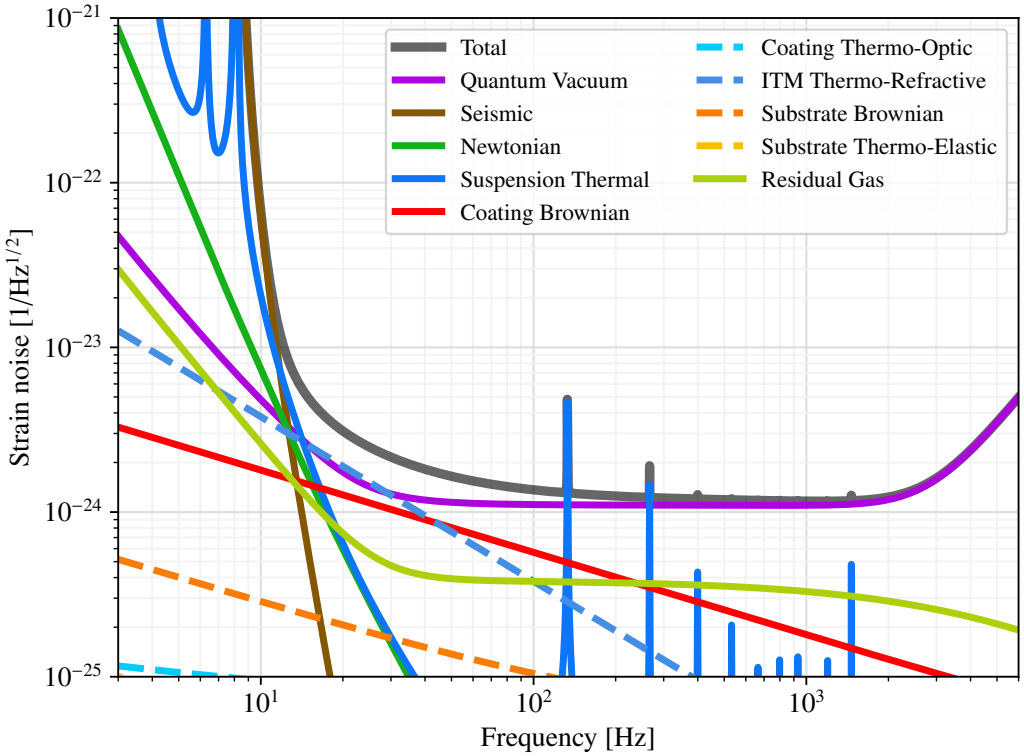

Figure 30: Voyager Wideband noise budget

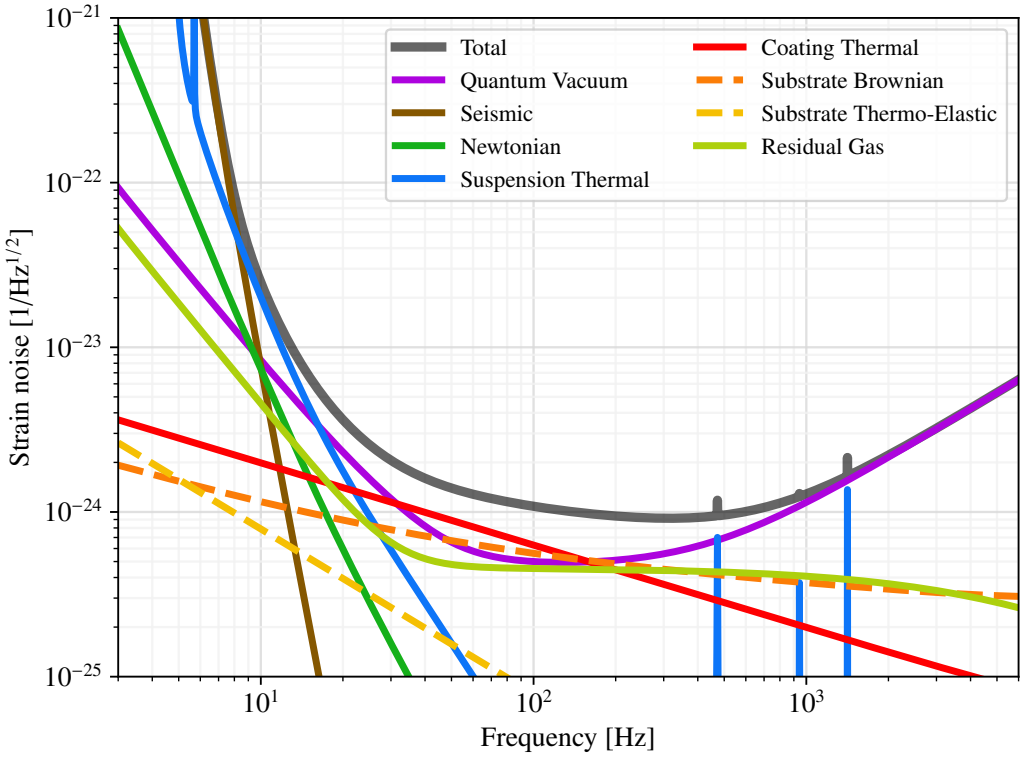

Figure 31: Spacetime Observatory (STO) noise budget

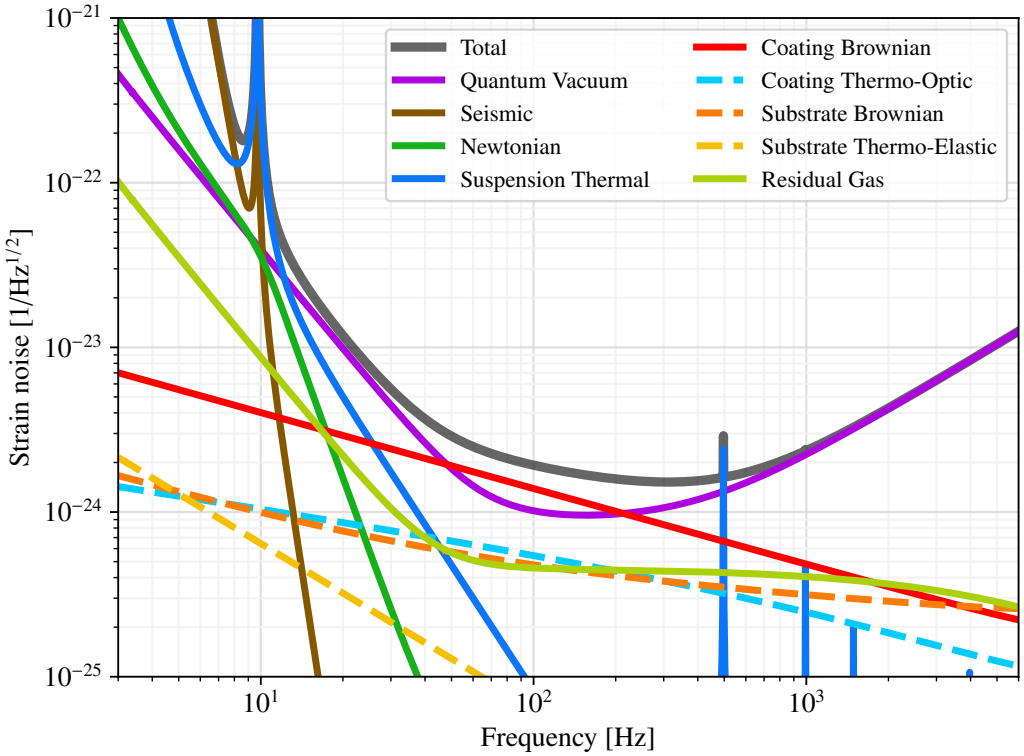

Figure 32: A+ noise budget

References

[1] R. X. Adhikari et al. (LIGO), "A cryogenic silicon interferometer for gravitational-wave detection", Class. Quant. Grav. **37**, 165003 (2020) (cit. on pp. 9, 33).

[2] D. Ganapathy et al., "Tuning Advanced LIGO to kilohertz signals from neutron-star collisions", Phys. Rev. D **103**, 022002 (2021) (cit. on pp. 10, 30, 31).

[3] A. V. Cumming et al., "Large-scale monolithic fused-silica mirror suspension for third-generation gravitational-wave detectors", Phys. Rev. Applied **17**, 024044 (2022) (cit. on pp. 16, 18).

[4] S. J. Cooper et al., "Interferometric sensing of a commercial geophone", Classical and Quantum Gravity **39**, 075023 (2022) (cit. on p. 20).

[5] J. C. Driggers, J. Harms, and R. X. Adhikari, "Subtraction of Newtonian noise using optimized sensor arrays", Phys. Rev. D **86**, 102001 (2012) (cit. on p. 21).

[6] J. Harms and S. Hild, "Passive Newtonian noise suppression for gravitational-wave observatories based on shaping of the local topography", Class. Quant. Grav. **31**, 185011 (2014) (cit. on p. 21).

[7] J. Yu et al., "Excess noise in highly reflective crystalline mirror coatings", arXiv:2210.15671 (2022) (cit. on p. 22).

[8] D. Kedar et al., "Frequency stability of cryogenic silicon cavities with semiconductor crystalline coatings", arXiv:2210.14881 (2022) (cit. on p. 22).

[9] M. Evans et al., "A horizon study for Cosmic Explorer: science, observatories, and community", arXiv:2109.09882 (2021) (cit. on pp. 23, 25).

[10] E. Genin et al., "Vacuum-compatible low-loss faraday isolator for efficient squeezed-light injection in laser-interferometer-based gravitational-wave detectors", Appl. Opt. **57**, 9705–9713 (2018) (cit. on p. 25).

[11] L. McCuller et al., "LIGO's quantum response to squeezed states", Phys. Rev. D **104**, 062006 (2021) (cit. on pp. 25, 27).

[12] H. Miao, N. D. Smith, and M. Evans, "Quantum limit for laser interferometric gravitational-wave detectors from optical dissipation", Phys. Rev. X **9**, 011053 (2019) (cit. on p. 25).

[13] D. Martynov et al., "Exploring the sensitivity of gravitational wave detectors to neutron star physics", Physical Review D **99**, 102004, 102004 (2019) (cit. on pp. 30, 31).

[14] M. E. Thomas, *Optical propagation in linear media: atmospheric gases and particles, solid-state components, and water*, Johns Hopkins University/Applied Physics Laboratory Series in Science and Engineering (Oxford University Press, Oxford ; New York, 2006) (cit. on p. 33).

[15] M. A. Green, *Silicon solar cells: advanced principles & practice* (Centre for Photovoltaic Devices and Systems, Univ. of New South Wales, Sydney, 1995) (cit. on p. 34).

[16] J. Steinlechner et al., "Silicon-Based Optical Mirror Coatings for Ultrahigh Precision Metrology and Sensing", Physical Review Letters **120**, 263602 (2018) (cit. on p. 34).

[17] G. L. Mansell et al., "Observation of squeezed light in the 2 μm region", Phys. Rev. Lett. **120**, 203603 (2018) (cit. on pp. 35, 42).

[18] M. J. Yap et al., "Squeezed vacuum phase control at 2 μm", Optics Letters **44**, 5386 (2019) (cit. on p. 35).

[19] S. Soni et al., "Reducing scattered light in LIGO's third observing run", Classical and Quantum Gravity **38**, 025016 (2021) (cit. on p. 39).

[20] R. Doering and Y. Nishi, eds., *Handbook of semiconductor manufacturing technology*, 2nd ed (CRC Press, Boca Raton, 2008) (cit. on p. 40).

[21] J. Degallaix et al., "Bulk optical absorption of high resistivity silicon at 1550 nm", Optics Letters **38**, 2047 (2013) (cit. on p. 40).

[22] F. Shimura, ed., *Oxygen in silicon*, Semiconductors and Semimetals 42 (Acad. Press, Boston, 1994) (cit. on p. 40).

[23] W. Götz et al., "Thermal donor formation and annihilation at temperatures above 500 °C in Czochralski-grown Si", Journal of Applied Physics **84**, 3561–3568 (1998) (cit. on p. 40).

[24] N. D. Akhavan et al., "Design Principles for High QE HgCdTe Infrared Photodetectors for eSWIR Applications", Journal of Electronic Materials **51**, 4742–4751 (2022) (cit. on p. 42).

[25] P. R. McCullough et al., "Quantum Efficiency and Quantum Yield of an HgCdTe Infrared Sensor Array", PASP **120**, 759 (2008) (cit. on p. 42).

[26] A. Soibel et al., "High operating temperature nBn detector with monolithically integrated microlens", Applied Physics Letters **112**, 041105 (2018) (cit. on p. 42).

[27] G. Mueller et al., "Determination and optimization of mode matching into optical cavities by heterodyne detection", Optics Letters **25**, 266–268 (2000) (cit. on p. 42).

[28] The LIGO Scientific Collaboration, the Virgo Collaboration, and the KAGRA Collaboration, "Population of Merging Compact Binaries Inferred Using Gravitational Waves through GWTC-3", Physical Review X **13**, 011048, 011048 (2023) (cit. on pp. 46, 49, 51).

[29] The LIGO Scientific Collaboration, the Virgo Collaboration, and the KAGRA Collaboration, "Observation of Gravitational Waves from Two Neutron Star-Black Hole Coalescences", Astrophysical Journal Letters **915**, L5, L5 (2021) (cit. on pp. 46, 49).

[30] B. P. Abbott et al. (KAGRA, LIGO Scientific, Virgo), "Prospects for observing and localizing gravitational-wave transients with Advanced LIGO, Advanced Virgo and KAGRA", Living Rev. Rel. **21**, 3 (2018) (cit. on p. 46).

[31] P. Madau and M. Dickinson, "Cosmic Star Formation History", Ann. Rev. Astron. Astrophys. **52**, 415–486 (2014) (cit. on pp. 48, 49).

[32] C. Van Den Broeck and A. S. Sengupta, "Binary black hole spectroscopy", Class. Quant. Grav. **24**, 1089–1114 (2007) (cit. on p. 49).

[33] *Noise curves used for Simulations in the update of the Observing Scenarios Paper*, https://dcc.ligo.org/LIGO-T2000012/public, 2020 (cit. on pp. 49, 50).

[34] C. Talbot et al., "Parallelized Inference for Gravitational-Wave Astronomy", Phys. Rev. D **100**, 043030 (2019) (cit. on p. 49).

[35] C. Talbot and E. Thrane, "Measuring the binary black hole mass spectrum with an astrophysically motivated parameterization", Astrophys. J. **856**, 173 (2018) (cit. on p. 49).

[36] B. P. Abbott et al. (LIGO Scientific, Virgo), "GWTC-1: A Gravitational-Wave Transient Catalog of Compact Binary Mergers Observed by LIGO and Virgo during the First and Second Observing Runs", Phys. Rev. X **9**, 031040 (2019) (cit. on p. 49).

[37] G. Pratten et al., "Computationally efficient models for the dominant and subdominant harmonic modes of precessing binary black holes", Phys. Rev. D **103**, 104056 (2021) (cit. on p. 49).

[38] C. García-Quirós et al., "Multimode frequency-domain model for the gravitational wave signal from nonprecessing black-hole binaries", Physical Review D **102**, 064002, 064002 (2020) (cit. on p. 49).

[39] G. Pratten et al., "Setting the cornerstone for a family of models for gravitational waves from compact binaries: The dominant harmonic for nonprecessing quasicircular black holes", Phys. Rev. D **102**, 064001 (2020) (cit. on p. 49).

[40] D. Christodoulou, "Nonlinear nature of gravitation and gravitational wave experiments", Phys. Rev. Lett. **67**, 1486–1489 (1991) (cit. on p. 50).

[41] P. D. Lasky et al., "Detecting gravitational-wave memory with LIGO: implications of GW150914", Phys. Rev. Lett. **117**, 061102 (2016) (cit. on p. 50).

[42] O. M. Boersma, D. A. Nichols, and P. Schmidt, "Forecasts for detecting the gravitational-wave memory effect with Advanced LIGO and Virgo", Phys. Rev. D **101**, 083026 (2020) (cit. on p. 50).

[43] T. Dietrich et al., "CoRe database of binary neutron star merger waveforms", Classical and Quantum Gravity **35**, 24LT01 (2018) (cit. on p. 50).

[44] E. E. Flanagan and T. Hinderer, "Constraining neutron star tidal Love numbers with gravitational wave detectors", Phys. Rev. D **77**, 021502 (2008) (cit. on p. 50).

[45] A. Akmal, V. R. Pandharipande, and D. G. Ravenhall, "The Equation of state of nucleon matter and neutron star structure", Phys. Rev. **C58**, 1804–1828 (1998) (cit. on p. 50).

[46] G. Ashton et al., "BILBY: A user-friendly Bayesian inference library for gravitational-wave astronomy", Astrophys. J. Suppl. **241**, 27 (2019) (cit. on p. 50).

[47] I. M. Romero-Shaw et al., "Bayesian inference for compact binary coalescences with bilby: validation and application to the first LIGO–Virgo gravitational-wave transient catalogue", Mon. Not. Roy. Astron. Soc. **499**, 3295–3319 (2020) (cit. on p. 50).

[48] T. Dietrich et al., "Improving the NRTidal model for binary neutron star systems", Phys. Rev. D **100**, 044003 (2019) (cit. on p. 50).

[49] S. Khan et al., "Frequency-domain gravitational waves from nonprecessing black-hole binaries. II. A phenomenological model for the advanced detector era", Phys. Rev. D **93**, 044007 (2016) (cit. on p. 50).

[50] K. Yagi and N. Yunes, "Approximate Universal Relations for Neutron Stars and Quark Stars", Phys. Rept. **681**, 1–72 (2017) (cit. on p. 51).

[51] K. Riles, "Searches for continuous-wave gravitational radiation", arXiv:2206.06447, 10.48550/ARXIV.2206.06447 (2022) (cit. on p. 52).

[52] O. J. Piccinni, "Status and perspectives of continuous gravitational wave searches", Galaxies **10**, 72 (2022) (cit. on p. 52).

[53] The LIGO Scientific Collaboration, the Virgo Collaboration, and the KAGRA Collaboration, "Searches for Gravitational Waves from Known Pulsars at Two Harmonics in the Second and Third LIGO-Virgo Observing Runs", Astrophysical Journal **935**, 1, 1 (2022) (cit. on pp. 52, 54).

[54] The LIGO Scientific Collaboration, the Virgo Collaboration, and the KAGRA Collaboration, "Narrowband Searches for Continuous and Long-duration Transient Gravitational Waves from Known Pulsars in the LIGO-Virgo Third Observing Run", Astrophysical Journal **932**, 133, 133 (2022) (cit. on p. 52).

[55] The LIGO Scientific Collaboration, the Virgo Collaboration, and the KAGRA Collaboration, "Search for continuous gravitational wave emission from the Milky Way center in O3 LIGO-Virgo data", Physical Review D **106**, 042003, 042003 (2022) (cit. on p. 52).

[56] R. Abbott et al., "Searches for Continuous Gravitational Waves from Young Supernova Remnants in the Early Third Observing Run of Advanced LIGO and Virgo", Astrophysical Journal **921**, 80, 80 (2021) (cit. on p. 52).

[57] The LIGO Scientific Collaboration, the Virgo Collaboration, and the KAGRA Collaboration, "Model-based cross-correlation search for gravitational waves from the low-mass X-ray binary Scorpius X-1 in LIGO O3 data", arXiv e-prints, arXiv:2209.02863, arXiv:2209.02863 (2022) (cit. on p. 52).

[58] The LIGO Scientific Collaboration, the Virgo Collaboration, and the KAGRA Collaboration, "All-sky search for continuous gravitational waves from isolated neutron stars using Advanced LIGO and Advanced Virgo O3 data", arXiv e-prints, arXiv:2201.00697, arXiv:2201.00697 (2022) (cit. on p. 52).

[59] The LIGO Scientific Collaboration, the Virgo Collaboration, and the KAGRA Collaboration, "All-sky search for gravitational wave emission from scalar boson clouds around spinning black holes in LIGO O3 data", Physical Review D **105**, 102001, 102001 (2022) (cit. on p. 52).

[60] P. Astone et al., "A method for detection of known sources of continuous gravitational wave signals in non-stationary data", Classical and Quantum Gravity **27**, 194016, 194016 (2010) (cit. on p. 53).

[61] J. A. Morales and C. J. Horowitz, "Neutron Star Crust Can Support A Large Ellipticity", arXiv e-prints, arXiv:2209.03222, arXiv:2209.03222 (2022) (cit. on p. 54).

[62] G. Woan et al., "Evidence for a Minimum Ellipticity in Millisecond Pulsars", Astrophys. Journal Lett. **863**, L40, L40 (2018) (cit. on p. 54).

[63] P. Astone et al., "Method for all-sky searches of continuous gravitational wave signals using the frequency-Hough transform", Physical Review D **90**, 042002, 042002 (2014) (cit. on p. 54).

[64] R. Dolesi et al., "Brownian force noise from molecular collisions and the sensitivity of advanced gravitational wave observatories", Phys. Rev. D **84**, 063007 (2011) (cit. on p. 56).